

# **Imaging Electrical Properties Using MRI and In Vivo Applications**

A DISSERTATION

SUBMITTED TO THE FACULTY OF THE GRADUATE SCHOOL  
OF THE UNIVERSITY OF MINNESOTA

BY

JIAEN LIU

IN PARTIAL FULFILLMENT OF THE REQUIREMENTS  
FOR THE DEGREE OF  
DOCTOR OF PHILOSOPHY

Dr. BIN HE, advisor

November, 2015



## Acknowledgement

I am really thankful to my advisor Dr. Bin He for his guidance over the years. I am grateful to his confidence on me and support even during difficult times when I almost lost confidence on myself. I appreciate his challenges to push me beyond my own comfort zone and grow mature both as a human and a researcher. I learned so much from his insightful and critical comments. Without his resource and support, my thesis work would have become difficult to move on.

I would like to thank my friend, colleague and mentor Dr. Xiaotong Zhang. Our discussion has been a source of inspiration. He always came with suggestions and encouragement. I also feel fortunate to work with Mr. Yicun Wang for his help in my research. His eagerness to learn in many times triggered me to think again about the problem to make sure I was clear.

I own great thanks to Dr. Pierre-Francois Van de Moortele and Dr. Sebastian Schmitter at CMRR for their deep MRI knowledge, scientific support and hours spent on the scanner. I want to thank Dr. Gregor Adriany for his generosity to share his knowledge and help on the animal coil. I also want to thank Ms. Lynn Utecht and Dr. Dinesh Deelchand for their technical help in the animal experiment. I would like to thank the Center for Magnetic Resonance Research for providing MRI and computation resource.

Many thanks go to Dr. John Bischof for providing the animal resource and Mr. Qi Shao for his scientific discussion and effort to make the animal model available.

I want to thank Dr. Leo Mariappan, Dr. Yunfeng Lu, Mr. Kai Yu, Mr. Long Yu, Mr. Abbas Sohrabpour and Mr. Keith Jamison for inspiring discussion and all the members in Dr. He's lab for their encouragement and friendship.

I want to give my deep thanks to my wife Ying Li for her continuous love and patience. I couldn't have gone through the doctoral study without her encouragement and support. It has been extremely challenging for her to be a graduate student, mother of two kids and wife of a PhD student. I am really grateful to my two lovely kids and beautiful angles Nathan and Elsa for the joy they have brought into our lives. I own too much to our parents and families in China for their love and support to us.

I am thankful to God for His everlasting grace, love, wisdom and blessings to me and my family.

## **Dedication**

This dissertation is dedicated to my grandfather Donghai Liu and grandmother Jianrong Liu.

## Abstract

Electrical properties, namely conductivity and permittivity, describe the interaction of materials with the surrounding electromagnetic field. The electrical properties of biological tissue are associated with many fundamental aspects of tissue, such as cellular and molecular structure, ion concentration, cell membrane permeability, etc. Electrical properties of tissue in vivo can be used as biomarkers to characterize cancerous tissue or provide useful information in applications involving tissue and electromagnetic field. Among many related electrical-property imaging technologies, electrical properties tomography (EPT) is a promising one that noninvasively extracts the in vivo electrical properties with high spatial resolution based on measured  $B_1$  field using magnetic resonance imaging (MRI). In this thesis, advanced EPT methods have been developed to improve the imaging quality of conventional EPT. First of all, a multi-channel EPT framework was introduced to release its dependency on a  $B_1$  phase assumption and expand its application under high field strength. Secondly, a gradient-based EPT (gEPT) approach was proposed and implemented, showing enhanced robustness against effect of measurement noise and improved performance near tissue boundaries. Using gEPT, high resolution in vivo electrical-property images of healthy human brain were obtained, and an imaging system for rat tumor models was also developed. As a result of malignancy, increased conductivity was captured in tumors using the in vivo animal imaging system. Thirdly, based on EPT theory, quantitative water proton density imaging was proposed using measured  $B_1$  field information, provide a new way for estimating water content in tissue for diagnostic and research purpose.

# Table of Contents

<b>ACKNOWLEDGEMENT</b>	<b>I</b>
<b>DEDICATION</b>	<b>III</b>
<b>ABSTRACT</b>	<b>IV</b>
<b>TABLE OF CONTENTS</b>	<b>V</b>
<b>LIST OF TABLES</b>	<b>VII</b>
<b>LIST OF FIGURES</b>	<b>VIII</b>
<b>CHAPTER 1 INTRODUCTION</b>	<b>1</b>
1.1 Motivation and Significance	1
1.2 Organization of the Dissertation	5
<b>CHAPTER 2 BACKGROUND</b>	<b>6</b>
2.1 Biophysics of Electrical Properties in Tissue	6
2.2 Measuring Electrical Properties	10
2.2.1 Invasive Methods	10
2.2.2 Imaging Methods	12
2.3 Theory of Electrical Properties Tomography	17
2.3.1 Introduction of magnetic resonance imaging	18
2.3.2 B <sub>1</sub> Field	21
2.3.3 Maxwell's Equations	22
2.3.4 Central Equations	23
2.3.5 Helmholtz Equation and Electrical Properties Tomography	25
<b>CHAPTER 3 HELMHOLTZ-BASED MULTICHANNEL ELECTRICAL PROPERTIES TOMOGRAPHY</b>	<b>27</b>
3.1 Introduction	27
3.2 Theory	28
3.3 Materials and Methods	30
3.3.1 Computer Simulation	30
3.3.2 Experiment Protocol	32
3.4 Results	34
3.5 Discussion and Conclusion	41
3.6 Appendix	44
<b>CHAPTER 4 GRADIENT-BASED ELECTRICAL PROPERTIES TOMOGRAPHY</b>	<b>46</b>
4.1 Introduction	46
4.2 Theory	47
4.3 Materials and Methods	48
4.3.1 Computer Simulation	48
4.3.2 Experiments	51
4.4 RESULTS	55
4.4.1 Simulations	55
4.4.2 Phantom Studies	61
4.4.3 In Vivo Human Experiments	63
4.5 Discussion	65
<b>CHAPTER 5 IN VIVO IMAGING OF ANIMAL TUMOR MODEL</b>	<b>71</b>
5.1 Introduction	71
5.2 Materials and Methods	73
5.2.1 Image Reconstruction Algorithm	73
5.2.2 RF Coil Construction	74

5.2.3	MRI Techniques	75
5.2.4	Phantom Construction	76
5.2.5	Animal Preparation and Tumor Model	77
5.2.6	In Vivo Experiment	78
5.2.7	Histology	78
<b>5.3</b>	<b>Results</b>	<b>79</b>
5.3.1	RF Coil Performance	79
5.3.2	Phantom Validation	81
5.3.3	In Vivo Imaging Result	86
<b>5.4</b>	<b>Discussion</b>	<b>90</b>
<b>CHAPTER 6</b>	<b>SIMULTANEOUS PROTON DENSITY AND ELECTRICAL PROPERTIES IMAGING</b>	<b>94</b>
<b>6.1</b>	<b>Introduction</b>	<b>94</b>
<b>6.2</b>	<b>Theory</b>	<b>97</b>
<b>6.3</b>	<b>Materials and Methods</b>	<b>99</b>
6.3.1	Simulation	99
6.3.2	Experiment	101
<b>6.4</b>	<b>Results</b>	<b>103</b>
6.4.1	Simulation	103
6.4.2	Experiment	107
<b>6.5</b>	<b>Discussion</b>	<b>112</b>
<b>CHAPTER 7</b>	<b>SUMMARY AND FUTURE WORK</b>	<b>118</b>
<b>7.1</b>	<b>Summary</b>	<b>118</b>
<b>7.2</b>	<b>Future Work</b>	<b>121</b>
7.2.1	Technical Development	121
7.2.2	Prospective Applications	123
<b>REFERENCE</b>		<b>126</b>



## List of Tables

Table 4.1 Relative errors and correlation coefficients of EP reconstruction using gEPT in the Duke head model based on various assumptions when SNR=50. ....	59
Table 6.1 Evaluation of reconstructed EP and proton density using duke head model..	107
Table 6.2 Reconstructed EP in the phantom. Units of $\sigma$ and $\varepsilon$ are S/m <sup>-1</sup> and $\varepsilon_0$ , respectively. ....	110
Table 6.3 Evaluation of reconstructed EP using gradient-based EPT and differently derived proton density.....	112

## List of Figures

Figure 2.1 Frequency dependence of electrical properties .....	8
Figure 2.2 Schematic of open coaxial line-based measurement of electrical properties ....	12
Figure 2.3 Conceptual diagram of electrical properties tomography .....	17
Figure 2.4 Nuclear precession around the static magnetic field. ....	19
Figure 2.5 Schematic of $B_1$ field and Rotating Frames .....	21
Figure 3.1 Schematic of simulation with multiple channels.....	31
Figure 3.2 Reconstructed absolute transmit $B_1$ phase.....	36
Figure 3.3 Reconstruction of electrical properties under noise free condition .....	37
Figure 3.4 Reconstruction of $\sigma$ and $\epsilon_r$ under noise condition .....	39
Figure 3.5 Effect of utilized channels. ....	40
Figure 3.6 Reconstructed electrical properties in phantom .....	41
Figure 4.1 Schematic diagram of the gradient-based EPT .....	47
Figure 4.2 Simulation and RF coil.....	49
Figure 4.3 Reconstruction of electrical properties using gEPT under noise free condition in simulation.....	56
Figure 4.4 Reconstruction of electrical properties using gEPT under noise condition in simulation.....	57
Figure 4.5 Summary of RE and CC of gEPT under different conditions. ....	60
Figure 4.6 Reconstruction using gEPT in phantom .....	62
Figure 4.7 In vivo experimental results in humans.....	63
Figure 4.8 Three slices of reconstructed in vivo electrical properties in a human brain ..	65

Figure 5.1 RF coil schematic and picture. ....	75
Figure 5.2 Noise correlation matrix of the RF coil.....	80
Figure 5.3 Measured transmit $B_1$ field magnitude maps using the RF coil .....	81
Figure 5.4 L-curve and convergence speed of the algorithm .....	82
Figure 5.5 Reconstructed electrical properties of a phantom .....	83
Figure 5.6 Effect of initial EP value on reconstruction result.....	85
Figure 5.7 Tumor location and histology of the first rat.....	86
Figure 5.8 Reconstructed conductivity in three slices in the first rat.....	87
Figure 5.9 Reconstructed conductivity in the second rat.....	89
Figure 6.1 Simulation setup .....	100
Figure 6.2 Results of reconstructed electrical properties in the digital phantom.....	105
Figure 6.3 Results of reconstructed electrical properties using Duke head model .....	106
Figure 6.4 Experimental condition.. .....	108
Figure 6.5 Results of reconstructed electrical properties in the phantom.....	109
Figure 6.6 Reconstructed proton density and its accuracy. ....	112

# Chapter 1 Introduction

## 1.1 Motivation and Significance

Electrical properties, including conductivity  $\sigma$  and permittivity  $\varepsilon$  are intrinsic properties of tissue as of other materials. They are also known as impedance or complex permittivity, based on specific combination of conductivity and permittivity. Electrical properties characterize the distribution of electromagnetic (EM) field inside a medium once it is exposed to EM stimulation. Electrical properties of tissue are closely associated with a series of fundamental tissue aspects, such as ion concentration, extracellular and intracellular water volume, cell membrane permeability, molecular dielectric relaxation, structural interfaces, etc. in response to the applied EM field (Pethig, 1984; Foster and Schwan, 1989; C. Gabriel et al., 1996; Sha et al., 2002). They are frequency dependent because at different frequencies, the molecular or cellular structure inside tissue exhibit various responses to the applied EM field.

Tissue electrical properties play an important role in biomedical research. They are useful to understand EM field distribution inside tissue. For example, accurate models of tissue's electrical properties are needed to localize the internal electrical activities based on noninvasive electrophysiological recording over the body surface such as electroencephalogram (EEG) (Assaf and Ebersole, 1997; He, 1999; Michel et al., 2004; Yang et al., 2012) and electrocardiogram (ECG) (Burnes et al., 2000; He and Cohen, 1992; Liu et al., 2006). On the other hand, electrical properties are critical to estimate the distribution and power of EM energy inside the body in some applications utilizing EM stimulation for treatment, such as deep brain stimulation (DBS) to mitigate Parkinson's

disease symptom (Benabid et al., 1991; Limousin et al., 1998), transcranial magnetic stimulation (TMS) in neuropsychiatry (George et al., 1999), radiofrequency (RF) ablation to remove arrhythmic genesis foci (Pappone et al., 2000) and RF hyperthermia in cancer treatment (Hiraoka et al., 1984). Model of electrical properties of the body is also critical to quantify tissue heating induced by EM wave emitted from antennas as used in cell phones or magnetic resonance imaging (MRI) scanners.

As fundamental tissue parameters, electrical properties can potentially be used as a biomarker indicating the health condition of tissue for diagnosis in clinical applications. Previous studies have shown that various diseases cause local changes of electrical properties relative to the healthy nearby tissue. Study carried out on animal models showed that cerebral ischemia could increase impedance up to 60% (Holder, 1992), suggesting an effective method for differentiating ischemic and hemorrhagic stroke. Differentiating between both types of stroke is a critical step when planning stroke attention within the first minutes following symptoms onset (European Stroke Initiative Executive Committee et al., 2003). Local ischemia and cell swelling that happen due to a focal seizure during epilepsy can also change the electrical properties (Lux et al., 1986). Among various cancers, breast cancerous tissue has been shown with the most different electrical properties compared to normal breast tissue (Surowiec et al., 1988; Joines, 1994). Benign breast tissue shows significantly different conductivity compared to malignant breast carcinoma (Jossinet, 1998). Other tumors such as melanoma and prostate cancer also exhibit more significant contrast compared to benign tissue in their electrical properties than using other conventional imaging modalities (Aberg et al., 2004; Halter et al., 2009).

In the past decades, a number of efforts have been made in an attempt to map distribution of electrical properties in vivo. Among related techniques, electrical impedance tomography (EIT) (Barber and Brown, 1983; Paulson et al., 1993; Metherall et al., 1996; Mueller et al., 1999; Brown, 2003) was the first developed and can provide high temporal resolution. However, EIT requires mounting electrodes and injecting current into the sample but provides limited spatial resolution due to small number of detecting electrodes and the ill-posed nature of the inverse problem. Magnetic resonance electrical impedance tomography (MREIT) (Oh et al., 2003a; Seo et al., 2003; Park et al., 2004; Kim et al., 2007; Seo et al., 2008; Woo and Seo, 2008; Kim et al., 2009) utilizes an MRI scanner to detect the magnetic field induced by the probing current, providing high spatial resolution, but requires safety-concerning current density to reach a sufficient signal to noise ratio. Both EIT and MREIT could be challenged by the shielding effect to make electrical current penetrate through non-conductive medium (such as the skull) (Xu and He, 2005). Magneto-acoustic tomography with magnetic induction (MAT-MI) holds promises of high spatial resolution, but a lot of instrumentation challenges need to be addressed before it can be used for clinical applications (Xu and He, 2005; Li et al., 2007; Hu et al., 2011; Mariappan and He, 2013).

Recently, electrical properties tomography (EPT) has gained considerable interest as a non-invasive in vivo imaging approach to simultaneously map conductivity and permittivity at Larmor frequency of proton using an MRI scanner (Haacke et al., 1991; U Katscher et al., 2009; Wen, 2003; Zhang et al., 2010). EPT reconstructs distribution of electrical properties from the measured RF field (or  $B_1$  field) in MRI, exploiting the relationship between the electrical properties and  $B_1$  field as described in Maxwell's

equations.  $B_1$  field is a magnetic field oscillating at Larmor frequency and commonly utilized in MRI to excite the sample for generating MRI images. Compared to other methods, EPT can achieve high spatial resolution and high penetration depth without the need of current injection. Scanning is conducted similarly to existing MRI imaging techniques, making it potentially applicable for clinical application.

In the meantime, electrical properties at Larmor frequency are key information in quantifying local specific absorption rate (SAR) (Gandhi and Chen, 1999; Collins et al., 2004; Wang et al., 2007; Collins, 2009), which is a measurement of the power of heating induced by the RF field. The intrinsic signal to noise ratio and contrast to noise ratio of MRI benefit from increased static magnetic field strength (Uğurbil et al., 2003; Duyn, 2012). However, SAR increases in proportion to the square of the operational frequency of  $B_1$  field. At high (3T) and ultra-high ( $\geq 7$  T) field magnetic field strength, SAR is a major safety concern in MR examinations and becomes a significant limiting factor in MRI. Knowing distribution of subject's electrical properties can help calculate the applied RF electrical field and allow for fast and subject-specific SAR estimation (Zhang et al., 2013a, 2014). Using this SAR information as a constraint to design RF pulses can potentially enhance flexible management of tissue heating, which in turn would optimize performance of high-field and ultra-high-field MR scanners under safety regulations.

In this thesis, new EPT imaging algorithms utilizing  $B_1$  field data from multiple channels of an RF coil were proposed. Computer simulation was utilized to evaluate the theory of the proposed algorithms. Experimental methods were developed to validate the proposed methods in realistic experimental scenarios. The developed methods have been applied to study the in vivo electrical properties of healthy human brain and tumors in an

animal model. The results show that the proposed work significantly enhanced the spatial resolution, sensitivity and accuracy of EPT. Without the need of external equipment to be mounted on body surface to inject current or to collect data, EPT is a convenient imaging methodology and suitable for basic research to uncover the fundamental tissue biophysics or clinical applications to provide valuable diagnostic information through imaging the electrical properties with high resolution and accuracy.

## **1.2 Organization of the Dissertation**

In Chapter 2, the biophysics of tissue electrical properties will be introduced. The significance of electrical properties in biomedical applications will be elaborated further. Various measurement and imaging techniques of tissue electrical properties will be reviewed. The origin, fundamental theory and the state of the art of electrical properties tomography (EPT) will be introduced.

In Chapter 3, a new method to quantitatively estimate the absolute  $B_1$  phase using multiple transmit or receive channels will be introduced.

In Chapter 4, a gradient-based EPT (gEPT) method will be introduced. The gEPT method shows significantly improved performance. The method has been applied to acquire in vivo electrical properties images of healthy human brain.

In Chapter 5, gEPT method has been applied to study tumor's conductivity compared to normal tissue in a rat tumor model.

In Chapter 6, a quantitative method for simultaneously extracting proton density (or water content) and electrical properties based on measured  $B_1$  data will be introduced.

The last chapter will be summary of the dissertation and discussion of future work.



## Chapter 2 Background

### 2.1 Biophysics of Electrical Properties in Tissue

Electrical properties, also known as dielectric properties, including conductivity ( $\sigma$ ) and permittivity ( $\epsilon$ ), are fundamental properties of materials. In some cases, conductivity and permittivity are jointly expressed in the term of complex permittivity, which is defined as

$$\hat{\epsilon} = \epsilon' + i\epsilon'' \quad (2.1)$$

where  $\epsilon' \equiv \epsilon_r \epsilon_0$  is permittivity  $\epsilon$  and  $\epsilon'' \equiv -\frac{\sigma}{\omega}$ . Here,  $\epsilon_0$  is the absolute permittivity of free space,  $\epsilon_r$  the relative permittivity and  $\omega$  the angular frequency.

The capability to transfer electrical current inside material is proportional to its conductivity. During the current conducting process, electrical energy is converted into heat due to the frictional motion of the current carrying charges against their surrounding environment. The local heating rate is proportional to the local  $\sigma$  and the squared magnitude of electric field. Permittivity measures the resistance to form an electric field inside a medium. It is directly related to electric susceptibility which is a measure of the polarization that is formed due to the separation of the centers corresponding to positive and negative charges inside molecules under an electric field. As a result of polarization, an internal electric field is created to counterbalance the applied external electric field so that the total field inside the medium is reduced. Part of the electric energy is stored in the polarized molecules of the medium, and this is the basic principle of electric capacitors to hold electric energy.

Biological tissue can be generally divided into intracellular and extracellular spaces separated by cell membranes, which are composed of a lipid bilayer with a thickness around 6 nm (Pethig, 1984). Electrical properties of tissue show significant frequency dependence. As shown in Figure 2.1, changes mainly occur in three steps which are also known as  $\alpha$ ,  $\beta$  and  $\gamma$  dispersions from low to high frequencies (Foster and Schwan, 1989). Dispersions reflect mechanisms by which various molecules or cell membranes interact with the EM field. In the low frequency range ( $<10$  kHz), the  $\alpha$  dispersion happens mainly because of the ionic diffusion through a polarized double layer near a large charged surface. The DC relative permittivity can be very high up to  $10^7$  because of this polarization near the interface. However, the conductivity increase in  $\alpha$  dispersion range is hardly noticeable, being small compared to the background conductivity. In the low frequency range, because of nonconductive nature of cell membranes, current is restricted in the extracellular space; thus little information about cellular structure and membrane can be deduced from the conductivity in this range. As the frequency increases, in the range of 0.1-10 MHz, another major dispersion, the  $\beta$  dispersion, occurs when electric current flows across cell membranes between the extracellular and intracellular fluid and charges the cell membrane to induce membrane polarization. This phenomenon is known as the Maxwell-Wagner polarization, explaining the frequency-dependent electrical properties of inhomogeneous materials even with compartments of frequency-independent electrical properties (Fricke, 1953). As frequency goes even higher above 0.1 GHz, both conductivity and permittivity change significantly in the so-called  $\gamma$  dispersion. The  $\gamma$  dispersion is associated with dipole relaxation of small polar molecules including proteins, polar side chains on proteins or

water. The dramatic conductivity increase is due to the dielectric loss of the polar molecules. The relative permittivity is firstly dominated by that of small protein and then by that of water as frequency increases. Above 100 MHz, relative permittivity is positively correlated with the water fraction inside tissue (Schroeder et al., 2008). The frequency spectrum of electrical properties can be described by relaxation models with multiple relaxation time constants to incorporate various dispersions. These models include variants of Debye (Hurt, 1985) or Cole-Cole (Cole and Cole, 1941) equations (S. Gabriel et al., 1996a).

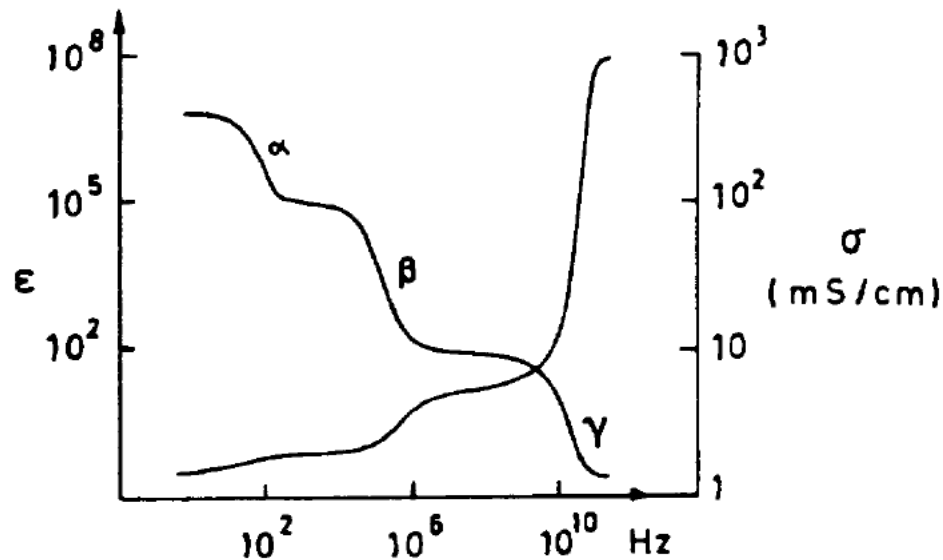


Figure 2.1 Frequency dependence of electrical properties (Schwan, 1994).

Certain tissues with specific structural heterogeneity exhibit orientation-dependent anisotropic electrical properties. For example, skeleton muscle and white matter have fibers with isolating membranes restricting ions from moving across. At low frequency, skeleton muscle exhibits a large anisotropy in their electrical properties, with three- to tenfold difference in frequency range  $<100$  kHz (Epstein and Foster, 1983). Similarly, in the frequency range of EEG signal, conductivity of white matter along a

fiber pathway is more than ten times higher than that perpendicular to the fiber direction (Güllmar et al., 2010). Anisotropy of conductivity of muscle and white matter reduces to less than 10% at frequencies above 10 MHz (S. Gabriel et al., 1996b). This can be understood given shorter ion displacement distance and smaller responsive molecules under high frequency oscillating EM field.

Besides the frequency- and orientation-dependency of electrical properties in tissue, they are also associated with temperature and physiological conditions (Foster and Schwan, 1989). The conductivity varies as a function of temperature with a coefficient within the range of -2%/K to 2%/K, which is determined by the relative contribution of ion and dipole loss at different frequencies (Foster and Schepps, 1981). For practical purposes, the temperature-dependence of electrical properties needs to be incorporated for predicting absorption of EM energy at 37 °C using data obtained at room temperature; it potentially affects the accuracy of RF dose in thermal ablation (Brace, 2008). In most of the literature, the reported electrical properties were measured in excised tissues that were removed from physiologically normal status. Factors such as blood supply, metabolism and cellularity, which either are immediately interrupted or slowly happen after tissue is excised, can affect tissue's electrical properties. It has been reported that there were no significant changes of electrical properties of feline brain tissues within the first minute after animals were sacrificed from 10 MHz to 1 GHz (Stuchly et al., 1981). However, the changes can progress over time as suggested by (Schmid et al., 2003). In their study, a decline of porcine gray matter conductivity of about 15% at 900 MHz and 11% at 1800 MHz was observed within the first hour after death, together with a less pronounced decrease of permittivity (3-4%), as a result of loss of blood supply and

terminated metabolism. Again, it necessitates the caution of relying on postmortem data to investigate EM distribution inside tissue in vivo.

## **2.2 Measuring Electrical Properties**

Measuring electrical properties of materials generally involves introducing certain type of EM energy into the medium and observing the response in either EM signal or other physical quantities to deduce the distribution or value of the electrical properties inside the medium. For tissue measurement, the methods can be divided into two categories: invasive methods, which usually require surgeries to gain access to the targeted region, and noninvasive imaging methods, which monitor the responding signal outside the body.

### **2.2.1 Invasive Methods**

Various methods have been utilized to acquire tissue's electrical properties in different frequency ranges. Most of these methods require invasive operations to gain access to the tissue unless it is located on the surface of the body such as skin, tongue, etc. The measured value has been used extensively to provide reference for other applications, such as predicting distribution of specific absorption rate (Christ et al., 2010), evaluation of EEG/ECG source imaging methods (Zhang et al., 2006), validation of medical devices (Grant and Lowery, 2010), etc.

In the lower frequency range, the measurement is performed by stimulating the tissue with controlled current source and measuring the actual voltage difference across the sample (Gabriel et al., 2009; Rush et al., 1963). These methods can be categorized into two kinds based on the number of employed electrodes. The first two-electrode method injects current and measures the voltage difference using the same pair of

electrodes. This method is sensitive to contact impedance and polarization effect between electrodes and the tissue (S. Gabriel et al., 1996b). The four-electrode method has been used to provide a means of eliminating the contact impedance (Rush et al., 1963; Lukaski et al., 1985). It separates current injection and voltage measurement using two pairs of electrodes. The contact impedance is negligible at the voltage electrodes compared to the very high input impedance of the amplifier.

In the high frequency range (100 MHz to a few GHz), one of the most common methods for measuring tissue's electrical properties is to use an open-ended coaxial probe, which is immersed into a liquid or in contact with a flat surface of a solid material as shown in Figure 2.2 (S. Gabriel et al., 1996b; Joines, 1994; Stuchly et al., 1981; Yoo, 2004). Part of the EM wave transmitted through the coaxial cable is reflected at the interface between the sample and the probe as a function of the difference of electrical properties between the sample and the probe. The reflected signal can be measured and used to calculate the electrical properties (Stuchly and Stuchly, 1980). The method offers easiness of sample preparation and accuracy for tissue measurement.

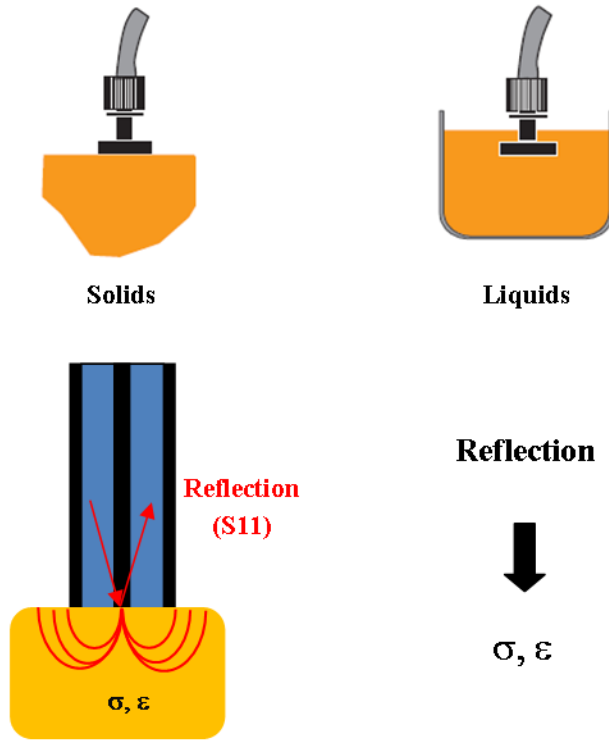


Figure 2.2 Schematic of open coaxial line-based measurement of electrical properties

### 2.2.2 Imaging Methods

Because most of the aforementioned measuring methods require contact of the probe with tissue, they are considered less capable to measure the true electrical properties of tissue under normal living conditions. Therefore, different noninvasive imaging methods have been developed to provide insight into the electrical properties of tissue in vivo. Some of these methods inject electrical current into tissue with electrodes on various locations on the surface of the body and acquire the potential distribution on the surface with electrodes whereas others induce EM response inside tissue using EM wave stimulation without the need of mounting electrodes on the body.

#### *Electrical Impedance Tomography*

Electrical impedance tomography (EIT) was first developed as an impedance-based tomographic imaging modality (Barber and Brown, 1983). This method measures

the distribution of body conductivity by injecting a low frequency (100 ~ 100 k Hz) current using electrodes mounted on the surface and recording surface voltages on multiple sites. For nearly static field the relationship between body conductivity ( $\sigma$ ) and electrical potential ( $\phi$ ) can be simplified as a non-linear equation:

$$\nabla \cdot (\sigma \nabla \phi) = 0 \quad (2.2)$$

In principle, this equation gives unique solution of conductivity given adequate boundary condition of  $\phi$  (Cheney et al., 1999). In practice, the normal current density (perpendicular to the surface) as a gradient of  $\phi$  is known on the surface of the object, but availability of the surface  $\phi$  is limited by the number of electrodes. In principle, if there are  $N$  voltage electrodes, the number of independent voltage measurements will be  $N(N-1)/2$ . This number limits the amount of information for image reconstruction. Therefore, the EIT problem is ill-posed, and its spatial resolution is limited. For image reconstruction, either single-step algorithms based on Jacobian of the forward solver (Metherall et al., 1996) and or iterative algorithms (Woo et al., 1992) have been proposed. The iterative algorithm is supposed to be more accurate to solve the nonlinear EIT equations, but it can more time consuming and put more challenges on instrumentation design.

The main advantages of EIT techniques are the low cost and high temporal resolution. The sampling frequency of commercial EIT system can reach a frame rate of more than 20 frames/s (Pulmovista 500, Drager Medical, Lubeck, Germany). Taking advantage of its high temporal resolution, certain EIT-based techniques has been applied in several clinical applications with different degree of success. For example, bedside monitoring EIT equipment has been installed in intensive care units and used as aides in



decision making processes related to the treatment of patients with acute respiratory distress syndrome (ARDS) (Blankman et al., 2013). However, due to the error of modeling and intrinsic ill-posedness of EIT, it can hardly achieve high spatial resolution. Spatial resolution around 5% to 10% of the object dimension is commonly achieved for EIT techniques (Malmivuo and Plonsey, 1995). This may limit the potential application of EIT as an imaging method for detecting lesion with small size, such as tumor in the early stage.

### ***Magnetic Induced Tomography***

Magnetic induced tomography (MIT) uses one or multiple pairs of coaxial exciting/receiving coils to stimulate the sample. The receiving coil detects the secondary signal  $\Delta B$  caused by the eddy current in the sample generated by the excitation EM wave, and images are reconstructed by backprojection (Griffiths et al., 1999). The spatial resolution depends on number of independent measurements done by the coil pairs. Compared with EIT, MIT does not need to mount the probe against surface of the subject. Thus it gives much flexibility of the measurement and eases the experience of the subject during the operation. A large integration of probe array makes no difference in the subject's view. More independent measurements can be done by rotating the probes by a small angle and this can help to improve the spatial resolution.

However, the MIT technique has been hammered by its technical difficulties (Griffiths, 2001). The first is the low sensitivity as the biological tissue usually has small variation of conductivity and the secondary signal  $\Delta B$  is very small compared to the primary signal  $B$ . Few articles reported satisfying *in vivo* measurement in the past ten

years. Another disadvantage similar to that of EIT is that MIT still need to solve the intrinsic ill-posed inverse problem which limits its spatial resolution and accuracy.

### ***Magnetic Resonance Electrical Impedance Tomography***

The current density imaging (CDI) technique utilizes the principle of MRI to measure the magnetic flux density caused by injected current (Joy et al., 1989; Scott et al., 1991). Although it does not measure electric properties directly, it provides the basis for later development of the magnetic resonance electrical impedance tomography MREIT technique. According to the static version of the Ampere's circuital law, the relationship between  $J(J_x, J_y, J_z)$  and the magnetic field  $B(B_x, B_y, B_z)$  could be described as:

$$J = \frac{\nabla \times B}{\mu_0} \quad (2.3)$$

Here,  $\mu_0$  is the permeability of free space. In order to get one component of  $J$ , the gradients of  $B$  in the other two dimensions are needed. With one MRI scan it is only able to measure one component of  $B$  in the direction of the main magnetic field. To get the measurement of one  $J$  component the sample or the main magnetic field  $B_0$  need to be orientated twice so that two components of  $B$  can be measured through MRI. Since it is unrealistic to change the orientation of  $B_0$  it might induce errors due to imperfect alignment of the sample. For human applications the limited space of the magnetic bore does not allow the subjects change their orientation to get a full measurement of one  $J$  component. Later it has been shown that under Larmor frequency one component of  $J$  can be measured by just one scan (Scott et al., 1995, 1992). But the subject still has to be reoriented to get a full measurement of  $J$ .

The MREIT technique takes advantage of the current density measured by CDI to help solve the ill-posed problem in EIT (Zhang, 1992; Oh et al., 2003a). A series of  $B_z$ -

based algorithms which use obtained  $B_z$  data with different current injection directions have been reported to eliminate the need of rotating subjects as required by the principle of CDI (Gao and He, 2008; Oh et al., 2003a; Park et al., 2004; Seo et al., 2008, 2003). *In vivo* experiments have been reported to obtain high resolution conductivity imaging (Kim et al., 2007). However, for both CDI and MREIT techniques the signal-noise ratio is positively related to the amplitude of injected current. High current density may cause excitation of neurons or heart failure. Further exploration of low current density technique is expected for the technique to be available in human application (Kim et al., 2009).

### ***Magnetoacoustic Tomography with Magnetic Induction***

The magnetoacoustic tomography with magnetic induction (MAT-MI) technique excites the sample with an alternative magnetic  $B_1$  field in a static magnetic field  $B_0$ . The induced eddy current generates Lorentz force in the  $B_0$  field and cause mechanical vibration of the sample, which is in turn detected by ultrasonic transducers (Xu and He, 2005; Li and He, 2010; Hu et al., 2011; Mariappan and He, 2013).

The electric properties can be reconstructed pixel-wise because spatial point can be determined by the echo-time of ultrasound. Thus, this method eliminates the ill-posedness compared with EIT or MIT. However, it might be limited in brain-related applications due to the blockade of skull to the sound echo. Besides pure electrical properties, the acquired signal might be confounded by other physical properties such as mechanical stiffness or elasticity of tissue. Further development is expected to demonstrate its value for clinical applications.

## 2.3 Theory of Electrical Properties Tomography

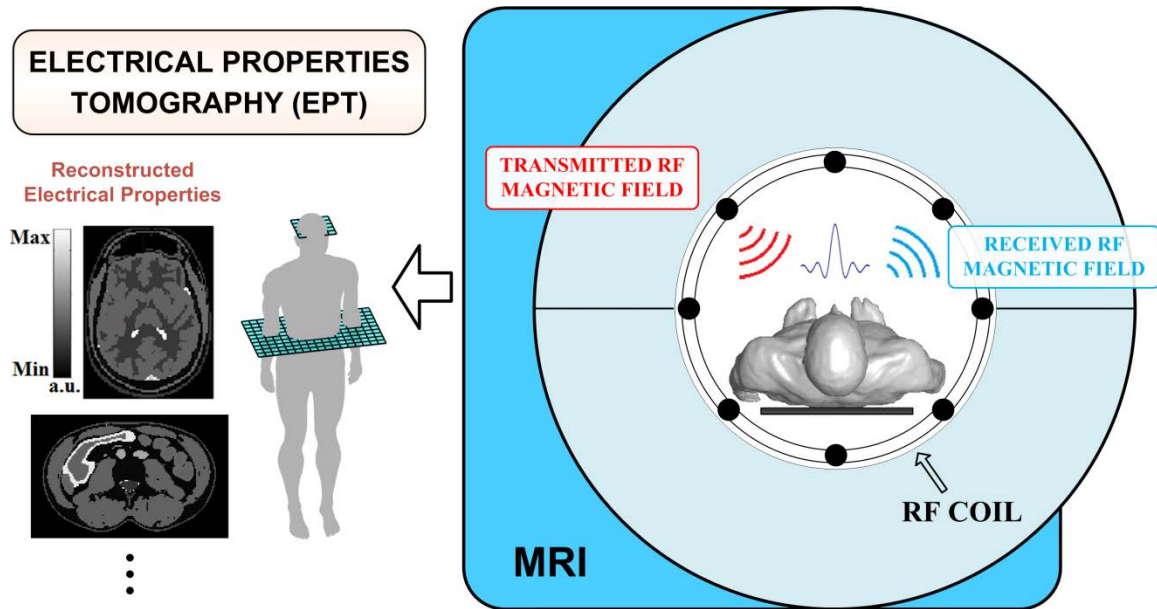


Figure 2.3 Conceptual diagram of electrical properties tomography

Electrical properties tomography (EPT) is a noninvasive method for imaging electrical properties in vivo using an MRI scanner. Figure 2.3 shows the conceptual diagram of EPT approach. The electrical properties distribution within the body is quantitatively reconstructed from the measured  $B_1$  field distribution of MRI. EPT requires no electrode mounting, and no additional external energy is introduced into the body during an MRI scanning other than the inherent  $B_1$  fields.

In next few sections, a brief background about magnetic resonance imaging (MRI) will be introduced to provide basic understanding about the phenomenon of nuclear magnetic resonance (NMR), how it has been utilized for imaging purpose and the foundation of using MRI to extract the electrical properties.

### 2.3.1 Introduction of magnetic resonance imaging

In current hospitals and research institutes, magnetic resonance imaging (MRI) is a powerful tool to provide high resolution and high contrast images of soft tissue for clinical diagnosis and research purposes. MRI is based on the phenomenon of nuclear magnetic resonance (NMR). NMR was first described and measured in molecular beams by (Rabi et al., 1938), who was awarded the Nobel Prize in Physics in 1944. The study was further extended in solids and liquid (Bloch, 1946; Purcell et al., 1946), for which Bloch and Purcell were awarded the Nobel Prize in Physics in 1952.

Base on NMR theory, protons and neutrons, which construct nuclei, have the intrinsic properties of spin. In quantum mechanics, the overall nuclear spin is characterized by the spin quantum number  $I$ . The quantum number  $I$  determines that there are  $2I+1$  orientations of the nuclear spins, each corresponding to a different energy level when an external magnetic field  $B_0$  is applied. For example, the nucleus of  $^1\text{H}$  with a spin number of  $1/2$  has two states:  $-1/2$  and  $+1/2$ . In an external  $B_0$  field, slightly more spins stay in the low energy status of  $+1/2$  with the initial distribution described in the Boltzmann distribution. The low energy spins can be excited into the high energy status with electromagnetic radiation, whose frequency is determined by the energy difference between energy levels.

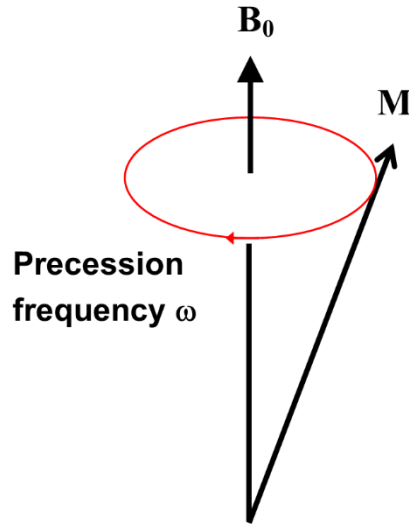


Figure 2.4 Nuclear precession around the static magnetic field.

The nucleus is positively charged and spinning. The generated magnetic moment  $\mu$  is determined by its spin quantum number  $I$ . In the perspective of classical mechanics, the total magnetization, consisting of a group of nuclear magnetic moments, behaves like a small magnetic dipole with its axis precessing around the  $B_0$  direction as shown in Figure 2.4. The vectorized precession angular frequency  $\omega$  is determined as

$$\omega = -\gamma B_0 \quad (2.4)$$

where  $\gamma$  is the gyromagnetic ratio and nucleus-dependent. For proton  $^1\text{H}$ ,  $\gamma$  is  $267.513 \times 10^6 \text{ rad s}^{-1} \text{ T}^{-1}$ . The precession frequency is also known as Larmor frequency. It is the same frequency of the applied RF electromagnetic field to induce nuclear precession. The dynamics of the macroscopic magnetization can be described by Bloch equation without considering relaxation effect (Bloch, 1946):

$$\frac{d\mathbf{M}(t)}{dt} = \gamma \mathbf{M}(t) \times \mathbf{B}(t) \quad (2.5)$$

where  $\mathbf{M}$  and  $\mathbf{B}$  are the time-varying vectors of magnetization and net magnetic field in the Cartesian coordinate, respectively. Equation (2.5) describes the precession of the magnetization around the axis in the direction of the magnetic field.

Once the incident RF field is turned off, the stimulated spins in the high energy status will return to its low energy status and generate RF signal at the same Larmor frequency, whose strength is proportional to the total magnetization of the nuclear spins in the sample.

It was not until 30 years after the discovery of NMR that MRI was developed to utilize NMR as an imaging method. In 1973, Lauterbur introduced the ground-breaking concept of superimposing linear gradient magnetic fields onto the main field to encode the nuclear spins at each location with different precession frequencies and reconstruct the image by Fourier transform of the encoded signal (Lauterbur, 1973). Lauterbur shared the Nobel Prize in Physiology or Medicine in 2003 with Peter Mansfield, who advanced MRI by developing echo planar imaging (EPI) for very fast imaging speed (Mansfield, 1977).

The spatial encoding idea overcomes the limitation on imaging resolution imposed by the fairly long wavelength of the RF field. In contrast to computerized tomography (CT), which is based on different attenuation of X-ray passing through tissue to generate high resolution images, MRI is more suitable to image soft tissue, does not use ionizing radiation and can be manipulated to reflect various aspects of tissue to generate useful contrast. Therefore, it has gained extensive applications in different areas from medical diagnosis to research investigation.

### 2.3.2 $B_1$ Field

As has been mentioned in section 2.3.1, in order to generate MRI signal, a short pulse of time-varying magnetic field or so called  $B_1$  field at Larmor frequency disturbs nuclear spins from their equilibrium status under an external static  $B_0$  field and generate nuclear spin precession.  $B_1$  field is emitted from a radiofrequency (RF) coil with oscillating electrical current running on its conductors, similar to antennas used to generate or detect microwave field. Compared with Larmor frequency, the utilized bandwidth of  $B_1$  field is normally extremely small. Therefore, the  $B_1$  field can be treated as a time harmonic field, i.e. with a single frequency component.

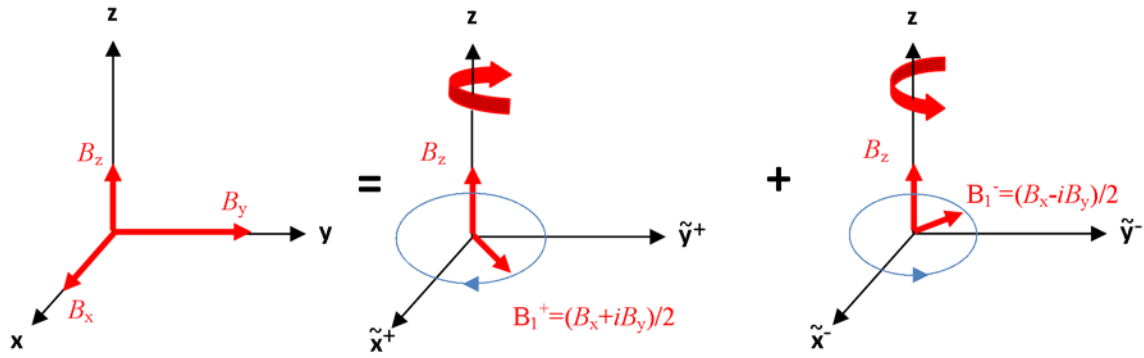


Figure 2.5 Schematic of  $B_1$  field and Rotating Frames

Effects of  $B_1$  field in MRI are twofold: one generating nuclear spin precession and another describing the sensitivity of RF coil to detect Larmor-frequency magnetic field generated by the nuclear spin precession. These two effects are reciprocal to each other. The  $B_z$  component of  $B_1$  field, which is in the direction of  $B_0$ , is not effective on MRI signal. The transverse  $B_1$  ( $B_x$  and  $B_y$ ) can be decomposed into two components:  $B_1^+$  rotating in the clockwise (or positively) direction along  $z$ -axis and  $B_1^-$  counterclockwise



(or negatively). As shown in Figure 2.5, these two components appear stationary in the corresponding coordinates rotating either positively or negatively. Corresponding to the role of  $B_1$  field in MRI, the  $B_1^+$  field effectively generates deviation of magnetization direction from the z-direction; the  $B_1^-$  field describes the sensitivity for detecting induced MRI signal from magnetization precession. Therefore,  $B_1^+$  and  $B_1^-$  are usually called transmit and receive  $B_1$  field, respectively. The detected MRI signal  $S$  has a dependency on  $B_1^+$  and  $B_1^-$  as (Hoult, 2000):

$$S \propto \exp(i\phi^+) \sin\left(v|B_1^+|\right) B_1^- \quad (2.6)$$

where  $\phi$  is the phase of the complex  $B_1^+$  field and  $v$  is a RF pulse-dependent factor determining the angle  $\alpha$  of magnetization flipped away from the z-direction. For example, for a hard pulse, the induced  $\alpha$  is

$$\alpha = \gamma\tau|B_1^+| \quad (2.7)$$

where  $\tau$  is the duration of the RF pulse.

### 2.3.3 Maxwell's Equations

Maxwell's equations are a set of partial differential equations, which form the foundation of classical electrodynamics, optics and electrical circuits. They are named after James Clerk Maxwell who published these equations between 1861 and 1862 (Maxwell, 1865). To describe the  $B_1$  field inside MRI, the time harmonic Maxwell's equations are utilized:

$$\begin{aligned}
\nabla \times \mathbf{B} &= j\omega\mu \left( \varepsilon - i\frac{\sigma}{\omega} \right) \mathbf{E} && \text{Ampere's circuit law} \\
\nabla \times \mathbf{E} &= -j\omega\mathbf{B} && \text{Faraday's law of induction} \\
\nabla \cdot \mathbf{B} &= 0 && \text{Gauss's law for magnetism} \\
\nabla \cdot \mathbf{E} &= \rho && \text{Gauss's law}
\end{aligned} \tag{2.8}$$

In Eq. (2.8),  $\mathbf{B}$  and  $\mathbf{E}$  are the complex magnetic and electric field,  $\omega$  the angular Larmor frequency,  $\rho$  the charge density,  $\sigma$  the conductivity,  $\varepsilon$  the permittivity and  $\mu$  the magnetic permeability. Ampere's circuit law tells that electric field drives the movement of charge to generate current, and current is the source of magnetic field. However, in free space, where charge does not exist, displacement current is introduced to compensate for this deficit. In Faraday's law, it can be seen that time varying magnetic field induce electric field.

### 2.3.4 Central Equations

Combining the time-harmonic Ampere's Law and Faraday's Law in Maxwell's equations, we can derive the following core equation underlying the EPT theory (Liu et al., 2014; Seo et al., 2012; Sodickson et al., 2013; Zhang et al., 2010):

$$-\nabla^2 \mathbf{B}(\mathbf{r}) = \omega^2 \varepsilon_c(\mathbf{r}) \mu_0 \mathbf{B}(\mathbf{r}) + \nabla \varepsilon_c(\mathbf{r}) \times \left[ \frac{\nabla \times \mathbf{B}(\mathbf{r})}{\varepsilon_c(\mathbf{r})} \right] \tag{2.9}$$

where  $\mathbf{r}$  denotes position and  $\mu_0$  the magnetic permeability of free space, respectively. For simplicity, the spatial coordinate variable  $\mathbf{r}$  will not be mentioned in the rest of this chapter.

Following the rule of cross product and curl operation, equation (2.9) can be rewritten as

$$\begin{aligned}
-\nabla^2 B_x &= \omega^2 \varepsilon_c \mu_0 B_x + g_y \left( \frac{\partial B_y}{\partial x} - \frac{\partial B_x}{\partial y} \right) + g_z \left( \frac{\partial B_z}{\partial x} - \frac{\partial B_x}{\partial z} \right) \\
-\nabla^2 B_y &= \omega^2 \varepsilon_c \mu_0 B_y - g_x \left( \frac{\partial B_y}{\partial x} - \frac{\partial B_x}{\partial y} \right) + g_z \left( \frac{\partial B_z}{\partial y} - \frac{\partial B_y}{\partial z} \right) \\
-\nabla^2 B_z &= \omega^2 \varepsilon_c \mu_0 B_z - g_x \left( \frac{\partial B_z}{\partial x} - \frac{\partial B_x}{\partial z} \right) - g_y \left( \frac{\partial B_z}{\partial y} - \frac{\partial B_y}{\partial z} \right)
\end{aligned} \tag{2.9}$$

In the rotating frame, the effective transmit and receive  $B_1$  field components can be expressed via the combination of the Cartesian  $B_1$  components (Hoult, 2000) as

$$\begin{aligned}
B_1^+ &= (B_x + iB_y)/2 \\
B_1^- &= (B_x - iB_y)/2
\end{aligned} \tag{2.9}$$

Utilizing Gauss's Law for Magnetism  $\nabla \cdot \mathbf{B} = 0$ , it gives us

$$\frac{\partial B_y}{\partial x} - \frac{\partial B_x}{\partial y} = -2 \left( i \frac{\partial B_1^+}{\partial x} + \frac{\partial B_1^+}{\partial y} + i \frac{1}{2} \frac{\partial B_z}{\partial z} \right) = 2 \left( i \frac{\partial B_1^-}{\partial x} - \frac{\partial B_1^-}{\partial y} + i \frac{1}{2} \frac{\partial B_z}{\partial z} \right) \tag{2.9}$$

Adding the first two identities in Eq. (2.10) with coefficients of  $(1, i)$  or  $(1, -i)$ , using the identities in Eq. (2.12), equation (2.9) can be further transformed into the expression of transmit ( $B_1^+$ ) or receive ( $B_1^-$ )  $B_1$  fields (Liu et al., 2014):

$$-\nabla^2 B_1^+ = \omega^2 \varepsilon_c \mu_0 B_1^+ + (ig_x - g_y) \left( i \frac{\partial B_1^+}{\partial x} + \frac{\partial B_1^+}{\partial y} + i \frac{1}{2} \frac{\partial B_z}{\partial z} \right) + g_z \left( -\frac{\partial B_1^+}{\partial z} + \frac{1}{2} \frac{\partial B_z}{\partial x} + i \frac{1}{2} \frac{\partial B_z}{\partial y} \right) \tag{2.10}$$

and

$$-\nabla^2 B_1^- = \omega^2 \varepsilon_c \mu_0 B_1^- + (ig_x + g_y) \left( i \frac{\partial B_1^-}{\partial x} - \frac{\partial B_1^-}{\partial y} + i \frac{1}{2} \frac{\partial B_z}{\partial z} \right) + g_z \left( -\frac{\partial B_1^-}{\partial z} + \frac{1}{2} \frac{\partial B_z}{\partial x} - i \frac{1}{2} \frac{\partial B_z}{\partial y} \right) \tag{2.11}$$

Here,  $\mathbf{g}$  denotes  $\nabla \ln \varepsilon_c$ , the gradient field of the natural logarithm of  $\varepsilon_c$ .

Although  $B_z$  is not directly measurable in MRI, in this thesis, we assume the contribution

of  $B_z$  could be ignored compared to  $B_1^+$  or  $B_1^-$  when an RF coil with conducting elements in parallel to  $B_0$  field is utilized (Katscher et al., 2012; Zhang et al., 2013b).

After the removal of  $B_z$ -related terms, defining  $g_+ \equiv g_x + ig_y$  and  $g_- \equiv g_x - ig_y$ , the central equations of EPT can be rewritten as

$$\nabla^2 B_1^+ \approx -\omega^2 \mu_0 B_1^+ \varepsilon_c + \nabla B_1^+ \cdot [g_+, -ig_+, g_z] \quad (2.12)$$

and

$$\nabla^2 B_1^- \approx -\omega^2 \mu_0 B_1^- \varepsilon_c + \nabla B_1^- \cdot [g_-, ig_-, g_z] \quad (2.13).$$

### 2.3.5 Helmholtz Equation and Electrical Properties Tomography

Inside a homogeneous medium with uniform  $\varepsilon$ ,  $\sigma$  and  $\mu$ , Helmholtz equations can be derived by eliminating  $\mathbf{g}$  in Eqs. (2.15) and (2.16) as

$$\nabla^2 B_1^+ \approx -\omega^2 \mu_0 B_1^+ \varepsilon_c \quad (2.14)$$

and

$$\nabla^2 B_1^- \approx -\omega^2 \mu_0 B_1^- \varepsilon_c \quad (2.15)$$

which show that the electrical conductivity and permittivity can be calculated once the magnetic field is available at each location. Helmholtz equation essentially describes the wave propagation of magnetic field inside a homogeneous medium. Using MRI, the distribution of  $|B_1^+|$  is readily measurable based on its relationship with the flip angle (Akoka et al., 1993; Van de Moortele and Ugurbil, 2009; Yarnykh, 2007) or MRI image phase (Duan et al., 2013; Sacolick et al., 2010). On the other hand, the absolute phase of transmit or receive  $B_1$  field cannot be directly measured with current techniques.

At lower field strength ( $\leq 3T$ ), using a birdcage quadrature transceiver RF coil, the absolute  $B_1^+$  phase has been assumed to be half of the transceiver phase (Wen, 2003).

In the early work of EPT, Helmholtz equation and the half-transceiver-phase (HTP) assumption have served as the core solution (Haacke et al., 1991; Ulrich Katscher et al., 2009; van Lier et al., 2012; Voigt et al., 2011; Wen, 2003). However, due to the assumed homogeneity of medium and inaccurate phase assumption, the Helmholtz-based EPT methods have several problems: 1) reconstruction errors will arise in regions with spatially varying electrical properties which is a common situation in tissue; 2) the reconstructed result is sensitive to noise in measured  $B_1$  field data because the second order derivative on  $B_1$  field magnifies the noise effect by a magnitude of squared spatial frequency; 3) The half-transceiver-phase assumption is only valid within a limited region inside the sample using a birdcage quadrature transceiver coil at lower field strength. This limits the application of EPT from other types of coils and higher field strength when the intrinsic signal to noise ratio (SNR) of MRI is high and it is more demanding for an accurate model of subject-specific electrical properties to calculate tissue heating.

In this thesis, both absolute phase and electrical properties will be derived based on measurable  $B_1$  field information including magnitude and relative phase using a multichannel transmit or receive RF coil. The new methods are not limited by phase assumption or main magnetic field strength. Because of abundant  $B_1$  information provided by multiple RF channels, the full equations (2.15) and (2.16) can be derived to overcome the problems related to inhomogeneous electrical properties encountered when Helmholtz equation is used.

# Chapter 3

## Helmholtz-based Multichannel Electrical Properties Tomography

### 3.1 Introduction

EPT requires a reliable measurement of complex  $B_1$  field maps (magnitude and phase) to calculate electrical tissue properties. Although the absolute magnitude of transmit  $B_1$  fields ( $B_1^+$ ) can be accurately measured on an MR scanner, the signal phase measured with coil elements, that are used for both transmission and reception ("transceivers"), is typically a combination of transmit, receive and system phase components (Van de Moortele et al., 2005). In most previous EPT studies, using a quadrature coil,  $B_1^+$  phase was simply estimated as roughly one half of the measured transceiver phase, with the transceiver phase representing the sum of  $B_1^+$  phase and  $B_1^-$  phase (van Lier et al., 2012; Voigt et al., 2011; Wen, 2003). However, the underlying assumption that  $B_1^+$  phase and  $B_1^-$  phase are approximately equal quantities cannot be sustained as the field strength increases and/or when a non-quadrature coil is used (Van de Moortele et al., 2005).

Still, *relative* transmit or receive  $B_1$  phases between channels can be easily obtained as the difference of two MRI phase using two transmit or receive channels. In this chapter, we introduce the framework of a new general approach to calculate conductivity  $\sigma$  and relative permittivity  $\epsilon_r$ , only utilizing quantities that are measurable in an MR scanner, i.e. magnitude and relative phase of  $B_1^+$  and  $B_1^-$  from multiple channels (Liu et al., 2013). Assuming the electrical properties of sample to be piecewise homogeneous, this approach does not depend on assumptions such as sample symmetry,

phase distribution, coil structure or field strength. Simulation studies were conducted at 298 MHz (the Larmor frequency of protons at 7T) to evaluate this approach under different noise levels, and experimental feasibility was demonstrated in a phantom experiment at 7T.

### 3.2 Theory

We assume that the imaging object is piecewise homogeneous and sufficiently high spatial resolution can be achieved to reconstruct the electrical properties inside a homogeneous piece. Inside a homogeneous region, the Helmholtz equations (2.17) and (2.18) are valid. By expanding the Laplacian on the left hand side of Eq. (2.17) and separating real and imaginary components, the expressions of  $\sigma$  and  $\varepsilon_r$  become

$$\begin{cases} \sigma = \frac{1}{\omega\mu_0} \left[ \nabla^2 \phi_j^+ + 2 \frac{(\nabla |B_{1j}^+|)^T}{|B_{1j}^+|} \cdot \nabla \phi_j^+ \right] \\ \varepsilon_r = \frac{1}{\omega^2 \mu_0 \varepsilon_0} \left[ -\frac{\nabla^2 |B_{1j}^+|}{|B_{1j}^+|} + (\nabla \phi_j^+)^T \cdot \nabla \phi_j^+ \right] \end{cases} \quad (3.1).$$

Channel  $n$  is arbitrarily selected as the reference channel. By subtracting both hand sides of Eq. (3.1) between channel  $j$  and channel  $n$ ,  $\sigma$  and  $\varepsilon_r$  vanish, and the following equation is obtained

$$\begin{cases} \left( \frac{\nabla |B_{1j}^+|}{|B_{1j}^+|} - \frac{\nabla |B_{1n}^+|}{|B_{1n}^+|} \right)^T \cdot \nabla \phi_n^+ = -\frac{1}{2} \nabla^2 \phi_{rj}^+ - \frac{(\nabla |B_{1j}^+|)^T}{|B_{1j}^+|} \cdot \nabla \phi_{rj}^+ \\ (\nabla \phi_{rj}^+)^T \cdot \nabla \phi_n^+ = \frac{1}{2} \left[ \frac{\nabla^2 |B_{1j}^+|}{|B_{1j}^+|} - \frac{\nabla^2 |B_{1n}^+|}{|B_{1n}^+|} - (\nabla \phi_{rj}^+)^T \cdot \nabla \phi_{rj}^+ \right] \end{cases} \quad (3.2)$$

where  $\phi_{rj}^+$  is the *relative* transmit phase of channel  $j$  ( $j \neq n$ ) with channel  $n$  as the reference channel. More details on how Eq. (3.2) was derived can be found in the

Appendix of this chapter. In Eq. (3.2), there are three unknowns of  $\nabla\phi_n^+ : \partial\phi_n^+/\partial x, \partial\phi_n^+/\partial y$  and  $\partial\phi_n^+/\partial z$ . Equation (3.2) is linear and can be solved by measuring the magnitude and relative phase of  $B_{1j}^+$  from as few as three channels, of which one is taken as the reference. Careful channel selection should consider covering the considered region of interest (ROI) with sufficient SNR for  $B_1$  measurement. One particular strategy is to choose adequate number of channels covering a specific ROI with stronger  $B_1$  magnitude as can be observed in the measured  $B_1$  maps of all channels. Naturally, using more channels will improve numerical accuracy and stability of the solution, as long as they contribute with sufficient SNR. Once  $\nabla\phi_n^+$  is derived from this set of equations (using three or more channels),  $\sigma$  and  $\varepsilon_r$  can be calculated using Eq. (3.1).

In principle, a similar equation, based on the same Helmholtz magnetic equation but in the form of  $B_{1k}^-$ , could also be derived. However, only  $|\rho B_{1k}^-|$ , rather than  $|B_{1k}^-|$ , can be measured in practice. Thus, within restricted regions where  $\rho$  is assumed to be approximately homogeneous, equation (3.1) can be re-written as

$$\left\{ \begin{array}{l} \sigma = \frac{1}{\omega\mu_0} \nabla^2 \phi_k^- + 2 \frac{(\nabla |\rho B_{1k}^-|)^T}{|\rho B_{1k}^-|} \cdot \nabla \phi_k^- \\ \varepsilon_r = \frac{1}{\omega^2 \mu_0 \varepsilon_0} \left[ -\frac{\nabla^2 |\rho B_{1k}^-|}{|\rho B_{1k}^-|} + (\nabla \phi_k^-)^T \cdot \nabla \phi_k^- \right] \end{array} \right. \quad (3.3).$$

Within these limits, equation (3.1) in the form of  $B_{1j}^+$  and its equivalent Eq. (3.3) in the form of  $\rho B_{1k}^-$  can even be summed to calculate  $\sigma$  and  $\varepsilon_r$  utilizing the measurable transceiver phase (Katscher et al., 2012; Van de Moortele et al., 2005; Voigt et al., 2011)



$\phi_{jk} = \phi_j^+ + \phi_k^-$  in order to reduce artifacts that may result from cumulative numerical errors in phase calculation.

Note that compared to another algorithm (Zhang et al., 2013b), in which the z-component of the magnetic field is assumed to be negligible in order to calculate the gradient of the absolute  $B_1$  phase, the present approach solves the phase gradients only using measurable transverse magnetic field components. Each set of selected channels determines the phase gradients voxel by voxel, without the assumption of a global phase approximation (Katscher et al., 2012). In addition, without assumption about RF coils, it enables optimized coil constructions for an improved EPT solution in the ROI.

### **3.3 Materials and Methods**

#### **3.3.1 Computer Simulation**

As illustrated in Figure 3.1, a simulation was performed with the numerical model of a 16-channel transmit/receive array coil (Adriany et al., 2008) loaded with an isotropic human head, which includes gray matter (GM), white matter (WM), cerebrospinal fluid (CSF), etc. The tissue electrical properties were assigned based on values reported in literature (S. Gabriel et al., 1996a). Based on the finite-difference-time-domain-method (FDTD), sixteen complex transmit and receive  $B_1$  fields, with a resolution of  $2 \times 2 \times 2.5$  mm<sup>3</sup>, were calculated by exciting one channel at a time at Larmor frequency for protons at 7T (298 MHz), using the XFDTD software (version 6.3, Remcom Inc., PA, USA).

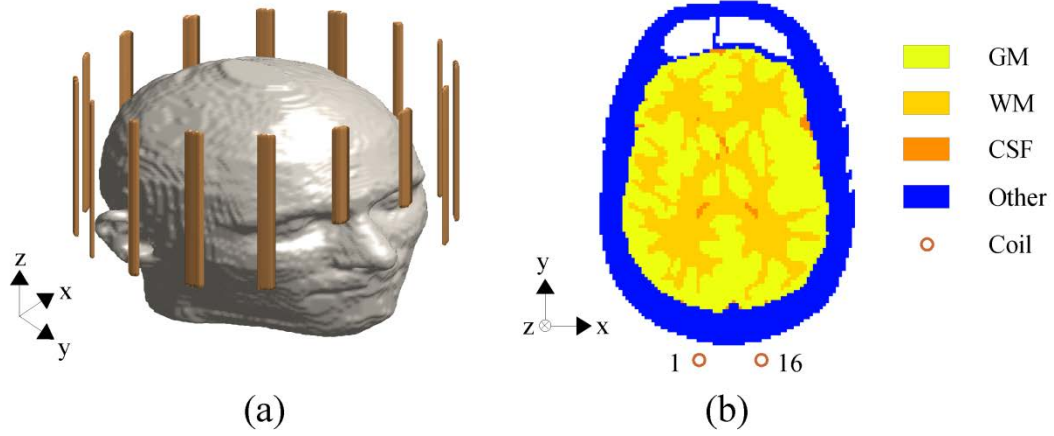


Figure 3.1 Schematic of simulation with multiple channels. (a) 3D view of the head model and coil elements. (b) Transverse view of the simulation model and numbering order of the coil element.

Four channels of complex  $B_{1,j}^+$  at a time, including one assigned as the reference channel, were used to reconstruct one set of  $\partial \phi_n^+ / \partial x$ ,  $\partial \phi_n^+ / \partial y$  and  $\partial \phi_n^+ / \partial z$  for the aforementioned reference channel. These quantities were inserted into Eq. (3.1) to calculate one set of parametric  $\varepsilon_r$  map. In order to reduce artifacts inherently amplified by the Laplacian operator over the reconstructed phase, equations (3.1) and (3.3) were summed to obtain  $\sigma$ , utilizing the additional measurable quantities  $|\rho B_{1k}^-|$  and transceiver phase  $\phi_n = \phi_n^+ + \phi_n^-$  for channel  $n$ . In order to utilize RF channels with the most distinctive  $B_1$  patterns, every fourth channel was picked, following azimuthal geometric order, to form each set of four channels. This process was repeated with each of the sixteen channels used as the reference, yielding a total of sixteen sets of  $\sigma$  and  $\varepsilon_r$  for the same head model to be combined to produce the final parametric maps. At the boundaries separating tissues with different electrical properties, artifactual errors would be induced as a direct consequence from the local violation of the piecewise homogeneous

assumption. These errors, which typically yielded locally out-of-range electrical property values, were identified by applying predefined upper and lower thresholds of valid electrical properties, and the corresponding values were recalculated by interpolation between nearby voxels.

The aforementioned reconstruction was performed after adding different levels of Gaussian white noise to the real and imaginary parts of the complex  $B_1$  fields, with standard deviation set to 1% and 2% of the average  $B_1$  magnitude for each channel in the ROI. The noise level was determined based on noise analysis in the experimental data. The noise-contaminated  $B_1$  data were firstly spatially smoothed using a Gaussian low-pass filter before the Laplacian operator was applied.

To evaluate the performance of the method, we used the averaged relative error (RE) and correlation coefficient (CC) to measure accuracy and similarity between the distributions of reconstructed and target maps, respectively. For a given parameter  $q$ , RE and CC are defined as

$$RE_q = \frac{\sum_{i=1}^N \left| \frac{q_{ri} - q_i}{q_i} \right|}{N} \quad (3.4)$$

and

$$CC_q = \frac{\sum_{i=1}^N (q_{ri} - \bar{q}_r) \cdot (q_i - \bar{q})}{\sqrt{\sum_{i=1}^N (q_{ri} - \bar{q}_r)^2 \cdot \sum_{i=1}^N (q_i - \bar{q})^2}} \quad (3.5)$$

### 3.3.2 Experiment Protocol

Experimental data were acquired in a phantom to further evaluate the proposed algorithm. The experiments were carried out on a 7T MR system (Siemens, Erlangen,

Germany; Magnex Scientific, Oxford, UK). A 16-channel transmit/receive head coil, which had been modeled for the simulation data, was utilized to transmit and receive RF energy, with the transmit channels powered by 16×1kW amplifiers (CPC, Hauppauge, NY, USA) interfaced with a remotely controlled phase/amplitude gain unit. A single-compartment cylindrical phantom was built with a diameter of 8.7 cm and a length of 20 cm. It was filled with a gel of saline solution composed of distilled water, NaCl, Gelatin (G2500, SIGMA) and  $\text{CuSO}_4 \cdot 5\text{H}_2\text{O}$  in the mass ratio of 100:0.12:3:0.025. Its conductivity and relative permittivity were measured as  $\sigma=0.34$  S/m and  $\epsilon_r=77$  at 298 MHz, using an Agilent 85070D dielectric probe kit and an Agilent E4991A network analyzer at Pennsylvania State University College of Medicine. During the experiment, the phantom was placed in the center of the coil with its longitudinal direction parallel to  $B_0$  field. In general, mapping transmit  $B_1$  field has the inherent advantage of avoiding the issue of proton density bias that typically occurs when mapping receive  $B_1$  field, where the relative contributions of proton density  $\rho$  and  $B_1$  magnitude  $|B_{1k}^-|$  cannot be distinguished in the measured product  $|\rho B_{1k}^-|$ . However, in the particular case of a homogeneous phantom, as in the present study,  $\rho$  is by definition constant throughout the entire phantom, and thus, is canceled out in equation (4), making it possible to utilize measured  $|\rho B_{1k}^-|$  and  $e^{i\phi_{rk}^-}$  for reconstruction. A straightforward advantage of this approach is that a higher SNR can typically be achieved per unit of acquisition time when mapping proton density weighted receive  $B_1$  field data. Thus, electrical properties reconstruction was performed based on the latter, rather than on transmit  $B_1$  information. Details of imaging protocols and sequences utilized to acquire magnitude and relative

phase maps, including  $|\rho B_{1k}^-|$  and  $\phi_{rk}^-$  for multiple channels can be found in a previous study (Zhang et al., 2013b). Briefly, a 3D flip angle (FA) map was measured using the Actual Flip Angle technique (AFI) (Yarnykh, 2007), all channels transmitting together with RF power adjusted to reach a high flip angle regime. Subsequently, with all channels still transmitting together, GRE images (gradient-recalled echo) were obtained, using the same FA as for AFI, with long  $T_R$  and short  $T_E$  to minimize the impact of  $T_1$  and  $T_2^*$ . The corresponding signal magnitude of the 16 receive channels was normalized by the sine of the acquired 3D FA map to generate  $|\rho B_{1k}^-|$  for the 16 channels ( $\rho$  being constant) (Van de Moortele et al., 2005). Corresponding relative phase maps were obtained from the phase of the same high SNR data set. Relevant acquisition parameters for 3D AFI:  $T_E/T_{R1}/T_{R2}=3.23/20/120$  ms, nominal FA=60°, eight averages, acquisition time ~170 min, and high SNR GRE images:  $T_E/T_R=3.73/5000$  ms, nominal FA=60°, 20 averages, acquisition time ~210 min. Twelve continuous slices were measured with a spatial resolution of  $1.5 \times 1.5 \times 1.5$  mm<sup>3</sup>.

The acquired data were firstly smoothed with a Gaussian filter to reduce high frequency noise. During the reconstruction, four channels of  $\rho B_{1k}^- e^{i\phi_{rk}^-}$  were used at a time to calculate  $\nabla \phi_k^-$ , with one of the four channels taken as a reference. In the absence of available transceiver phase, both  $\sigma$  and  $\varepsilon_r$  were calculated using (4) once  $\nabla \phi_k^-$  was obtained.

### 3.4 Results

Using the numerical simulation of the coil array loaded with a head model, we evaluated the performance of our proposed method to image the electrical property maps

of soft brain tissues, including gray matter (GM), white matter (WM) and cerebrospinal fluid (CSF).

Figure 3.2 illustrates, within a slice of interest, reconstructed phase maps of the transmit  $B_1$  field in comparison with the target phase maps, i.e. as obtained in the simulation data, under noise free condition. Here, the magnitude and relative phase of transmit  $B_1$  field from channel #3, #7, #11 and #15 were sent into (3), with channel #3 as the reference. The reconstructed phase maps agreed well with simulated ones, with a mean error of 0.13 radians and a CC of 97.2%.

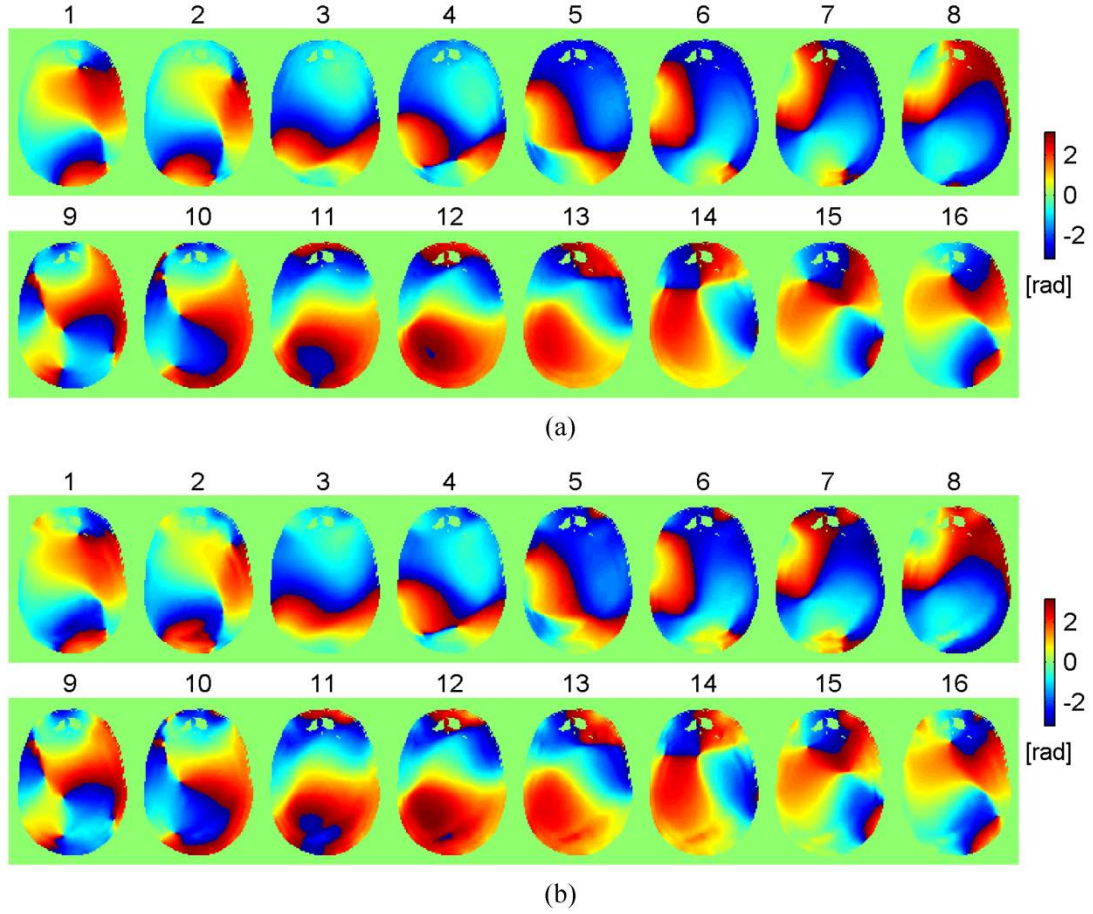


Figure 3.2 Reconstructed absolute transmit  $B_1$  phase. (a) Simulated phase maps of transmit  $B_1$  field for 16 channels. (b) Reconstructed phase maps of transmit  $B_1$  field for corresponding channels.

Under the same noise free condition, the reconstructed electrical property maps of the tissues of interest (GM, WM and CSF) are shown in Figure 3.3 for the same slice as in Figure 3.2, with other tissues masked by the target electrical property values around the periphery. The predefined [min, max] thresholds for removing boundary artifacts were set to  $[0, 3]$  S/m for  $\sigma$  and  $[0, 100]$  for  $\epsilon_r$ , based on reported values for brain tissues (C. Gabriel et al., 1996). Due to the violation of piecewise homogeneous assumption, noticeable residual error can be observed near the boundaries of tissues. Overall, the electrical properties of the brain tissues are successfully reconstructed, and in comparison

with the target images, anatomical structures of GM, WM and CSF are clearly identified in the estimated maps for both  $\sigma$  and  $\varepsilon_r$ . Within the ROIs of GM and WM, the reconstructed mean  $\pm$  SD (standard deviation) of  $\sigma$  are  $0.84 \pm 0.19$  and  $0.55 \pm 0.08$  S/m, respectively, with respect to the target values of 0.83 and 0.49 S/m; the reconstructions of  $\varepsilon_r$  are  $54.1 \pm 11.2$  and  $48.1 \pm 10.1$ , respectively, comparing to target values of 58.3 and 42.8.

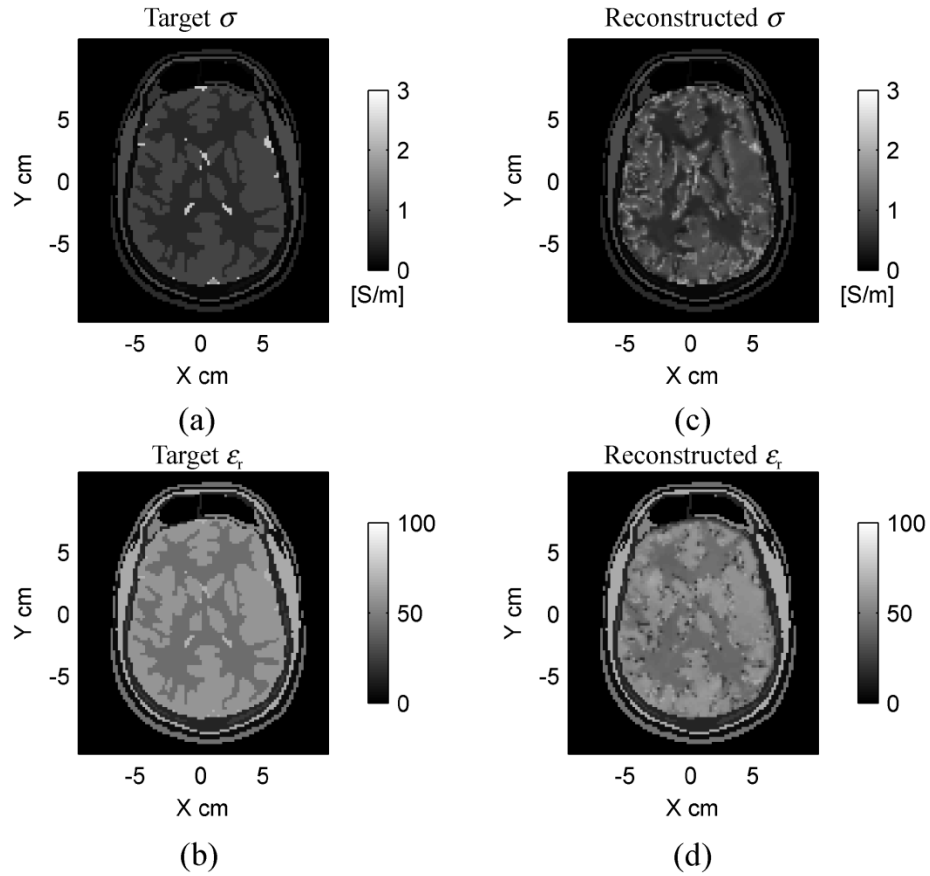


Figure 3.3 Reconstruction of  $\sigma$  and  $\varepsilon_r$  using the proposed algorithm applied on simulation data at 7T under noise free condition. (a)-(b) Target electrical properties. (c)-(d) Reconstructed properties.

The imaging results under noise levels of 1% (SNR=100) and 2% (SNR=50) are shown in Figure 3.4. A Gaussian filter with kernel size of 7 was applied to the  $B_1$  field. As a result of the spatial filtering on the  $B_1$  field, the reconstructed electrical property maps were spatially smoothed as we can see in Figure 3.4(c)-(f). Thus, CSF, which



covers a minor area in the original target images in Figure 3.4(a) and (b) is not seen in the reconstructed images. A smaller kernel size would help better define the image structure, but may compromise the accuracy due to intrinsic sensitivity of the Laplacian operator in EPT algorithms. When SNR=100, the reconstructed electrical properties in ROIs of GM and WM are  $\sigma=0.81\pm0.19$  and  $0.66\pm0.14$  S/m, respectively, and  $\varepsilon_r=57.1\pm7.6$  and  $48.7\pm5.8$ , respectively; when SNR=50, the corresponding results are  $\sigma=0.81\pm0.18$  and  $0.65\pm0.14$  S/m, and  $\varepsilon_r=57.7\pm7.7$  and  $49.0\pm6.5$ .

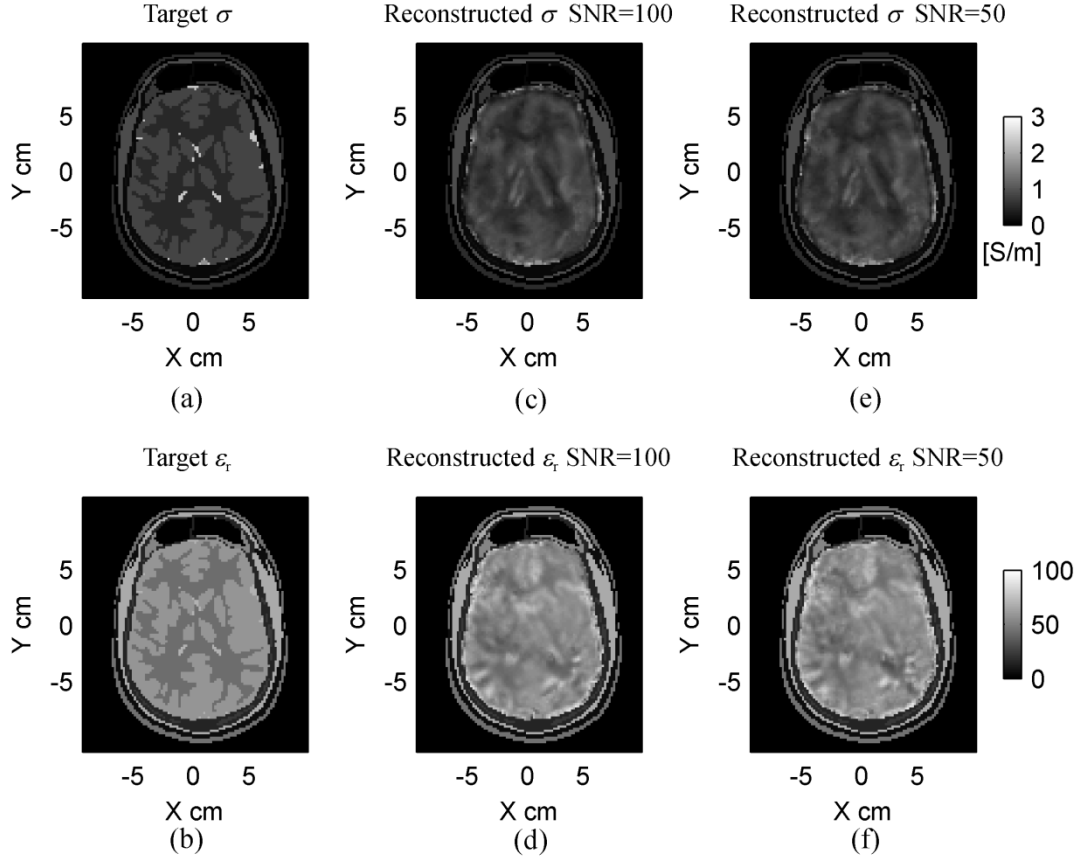


Figure 3.4 Reconstruction of  $\sigma$  and  $\epsilon_r$  using the proposed algorithm applied on simulation data at 7T under different noise levels. (a)-(b) Target electrical properties. (c)-(d) Reconstructed properties with SNR=100. (e)-(f) Reconstructed properties with SNR=50.

In order to verify the appropriateness of using every fourth channel to generate each group of four channels to calculate electrical properties maps, we investigated the impact of the distance between channels within a group by comparing RE in calculated  $\sigma$  and  $\epsilon_r$  maps when using every first, second, third or fourth channels to form each group. As shown in Figure 3.5, keeping the maximum distance of 4 coil elements between channels within a group clearly provided the smallest residual errors. This can be explained by the fact that the electromagnetic coupling between coil elements, which are utilized in the computation, decreases as the distance between them increases.

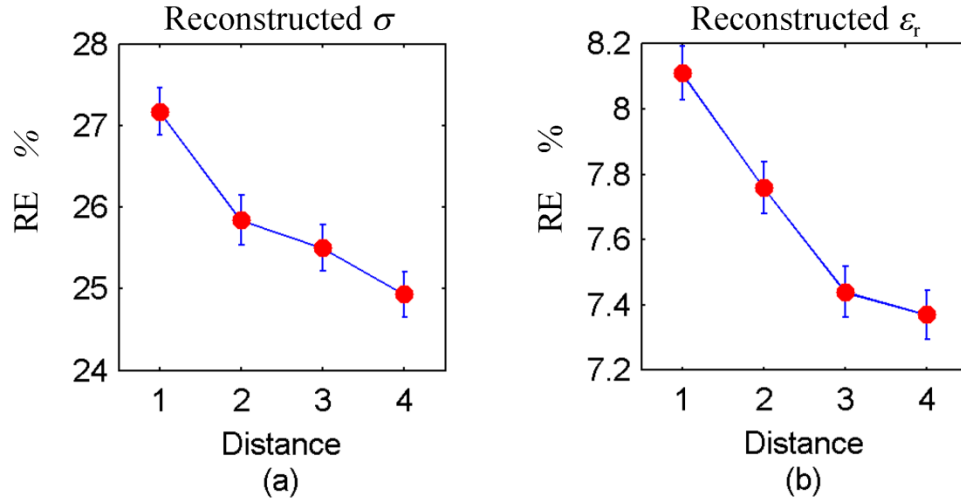


Figure 3.5 Mean REs for reconstructed electrical properties maps as a function of distance between neighboring channels expressed as number of coil elements. (a) Conductivity. (b) Relative permittivity.

Line profiles through the reconstructed  $\sigma$  and  $\epsilon_r$  maps along the x-direction, crossing the center of the phantom, are shown in Figure 3.6. In the region where FA was greater than  $36^\circ$  (providing high SNR), which covers more than half of the slice and includes the entire central profile, the reconstruction results (mean  $\pm$  SD) are  $\sigma=0.33\pm0.08$  S/m and  $\epsilon_r=78.2\pm5.4$ . As a reference, the aforementioned values of  $\sigma$  and  $\epsilon_r$  measured by a probe are 0.34 S/m and 77, respectively. Meanwhile, the reconstruction results throughout the entire slice are  $\sigma=0.39\pm0.14$  S/m and  $\epsilon_r=71.0\pm14.0$ .

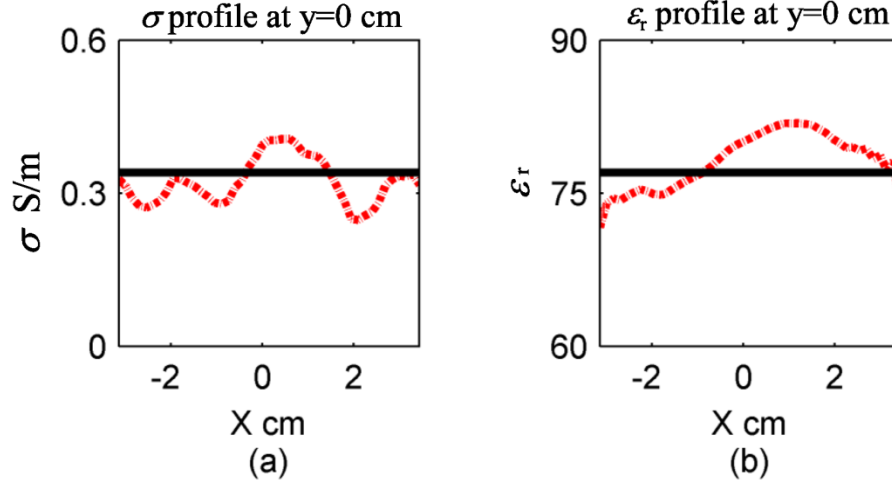


Figure 3.6 Reconstructed electrical property profiles along x-direction across the center of the phantom. The black solid lines are the probe measured value; the red dash lines indicate the reconstructed value.

### 3.5 Discussion and Conclusion

In the present study, a general approach for calculating conductivity and permittivity, using the  $B_1$  field data from multiple transmit/receive channels measured in an MR scanner, was introduced. Using simulation data based on the model of a multi-channel transmit/receive coil loaded with a human head at 7T, feasibility has been shown for imaging electrical properties of human tissue under both noise-free and noisy situations. Furthermore, the validity of the approach was experimentally demonstrated in a phantom on a 7T MR scanner.

Until now, lack of measurable absolute phase for transmit/receive  $B_1$  field has imposed serious limitations on EPT approaches. Thus, various assumptions for coil, sample and field strength have been necessary to meet certain condition for the  $B_1$  field in order to solve the Helmholtz equation (van Lier et al., 2012; Voigt et al., 2011; Zhang et al., 2013b). In the present study, the framework of the proposed method does not rely on any of these assumptions, offering the potential of significantly broadening the range of

applications for EPT. For example, with flexible channel selection and unconstrained field distribution, EPT could contribute as a diagnostic tool for characterizing malignant liver tissue (O'Rourke et al., 2007), while other EPT approaches, which depend on symmetry of the sample or equal-phase assumption, may suffer from asymmetry or large scale of the abdomen. Without limitation on field strength, EPT can potentially benefit from higher magnetic fields taking advantage from the more rapid spatial change of  $B_1$  fields and from improved SNR of the acquired  $B_1$  data. In turn, improved EPT could provide reliable real-time and patient-specific SAR calculation, which is especially significant at ultra-high field.

Different from quadrature coils, where transmit and receive  $B_1$  fields exhibit fixed spatial patterns with very limited degrees of freedom, RF coils with multiple transmit/receive channels can shape the  $B_1$  field distribution dynamically for imaging benefit; in addition, multi-channel  $B_1$  magnitude and relative phase between channels can be obtained, after which the non-measurable absolute phase of each channel can be derived through different ways. The method proposed by Zhang *et al* (2012) was based on the observation of mirroring relationship between transmit and receive  $B_1$  magnitude and on neglecting the  $B_z$  component to obtain the phase solution, requiring both within-plane object symmetry and channels aligned in parallel with the z-direction. In the study by Katscher *et al* (2012), the absolute phase was estimated based on a global polynomial approximation of the phase distribution throughout the region of interest. However, errors that resulted from eliminated higher order components of the spatial phase distribution can propagate into the calculation of electrical properties and SAR through subsequent spatial derivation. By contrast, the method proposed here can calculate the absolute phase

without dependency on sample symmetry, coil structure or distribution of the  $B_z$  component.

With the formalism of the proposed approach, it is the first time that only the magnitude and the relative phase of transmit or receive  $B_1$  fields are sufficient to calculate the parametric maps of the desired electrical properties and accurately estimate the corresponding absolute  $B_1$  phase. This approach merits further investigation in the context of real time, subject-specific SAR estimation during an MR scanning session. However, in the simulation study performed in the current work, in order to avoid Laplacian operation on the calculated absolute transmit or receive  $B_1$  phase, the transceiver phase was used to calculate the conductivity. In actual experiments, this will lead to additional scanning time because the transceiver phase and information on both transmit and receive  $B_1$  fields are needed when equation (2) and (4) are summed to calculate the conductivity. Further optimization in acquisition methods, however, can help addressing this issue. For example, the transceiver phase could be measured using faster imaging sequences while providing satisfactory SNR (Stehning et al., 2011). On the other hand, investigation on imaging processing tools on the retrieved  $B_1$  phase will be useful to eliminate using the transceiver phase.

Violation of the homogeneous assumption near tissue boundaries is the major source of residual errors in the proposed method. Although boundary errors were effectively suppressed by using predefined thresholds on the parametric maps, as shown in the simulation study, valuable information may be lost under exceptional situation such as a tumor with electrical properties significantly differing from that of surrounding tissues. More advanced filtering algorithms could be developed to address boundary

errors arising in calculated phase gradient maps. In addition, the mathematical formalism allowing for the inhomogeneous version of the Helmholtz equation (Zhang *et al* 2010) could be further developed in order to be integrated within the general theoretical framework proposed here. Meanwhile, it is worth noting that in the simulation study, a piecewise homogeneous head model was used with discrete discontinuities of electrical properties at tissue boundaries; it remains to be seen whether *in vivo* experimental data may provide smoother transition of electrical properties, that would inherently mitigate the aforementioned boundary issues.

Directly benefiting from high spatial resolution accessible with MRI data, in completely non-invasive settings, MR-based EPT methods hold strong promises towards *in-vivo* characterization of tissue electrical properties. In this study, a new general framework was introduced to further enable the development of EPT methods with the ultimate goal of enabling clinical EPT applications.

### 3.6 Appendix

Expanding the Laplacian operation on the complex  $B_1$  field  $B_{1j}^+ = |B_{1j}^+| e^{i\phi_j^+}$  of channel  $j$ , we have

$$\nabla^2 B_{1j}^+ = e^{i\phi_j^+} \left[ \nabla^2 |B_{1j}^+| + 2i \left( \nabla |B_{1j}^+| \right)^T \cdot \nabla \phi_j^+ + i |B_{1j}^+| \nabla^2 \phi_j^+ - \left( \nabla \phi_j^+ \right)^T \cdot \left( \nabla \phi_j^+ \right) |B_{1j}^+| \right] \quad (3.6)$$

Now dividing Eq. (3.6) by  $-B_{1j}^+ \omega^2 \mu_0$ , equation (2.17) can be rewritten as

$$\begin{aligned} & \varepsilon_r \varepsilon_0 - i\sigma / \omega \\ &= \frac{1}{\omega^2 \mu_0} \left[ -\frac{\nabla^2 |B_{1j}^+|}{|B_{1j}^+|} + \left( \nabla \phi_j^+ \right)^T \cdot \left( \nabla \phi_j^+ \right) \right] - i \frac{1}{\omega^2 \mu_0} \left[ \nabla^2 \phi_j^+ + 2 \frac{\left( \nabla |B_{1j}^+| \right)^T}{|B_{1j}^+|} \cdot \nabla \phi_j^+ \right] \end{aligned} \quad (3.7)$$

Separating the real and imagery components in Eq. (3.7), equation (3.1) can be derived immediately.

Given a reference transmit channel  $n$ , the absolute transmit  $B_1$  phase of any transmit channel  $j$  can be expressed as:

$$\phi_j^+ = \phi_{rj}^+ + \phi_n^+ \quad (3.8)$$

Based on Eq. (3.8), we can further expand the phase-related items in Eq. (3.1) and get

$$\begin{aligned} \sigma &= \frac{1}{\omega\mu_0} \left[ \nabla^2 \phi_{rj}^+ + \nabla^2 \phi_n^+ + 2 \frac{(\nabla |B_{1j}^+|)^T}{|B_{1j}^+|} \cdot (\nabla \phi_{rj}^+ + \nabla \phi_n^+) \right] \\ \varepsilon_r &= \frac{1}{\omega^2 \mu_0 \varepsilon_0} \left[ -\frac{\nabla^2 |B_{1j}^+|}{|B_{1j}^+|} + (\nabla \phi_{rj}^+)^T \cdot \nabla \phi_{rj}^+ + 2(\nabla \phi_{rj}^+)^T \cdot \nabla \phi_n^+ + (\nabla \phi_n^+)^T \cdot \nabla \phi_n^+ \right] \end{aligned} \quad (3.9)$$

At a specific position,  $\sigma$  and  $\varepsilon_r$  do not depend on channels. Subtracting Eq. (3.9) for channel  $n$  from Eq. (3.9) for channel  $j$ , we obtain Eq. (3.2).

Similar derivation can be applied to acquire the corresponding equations based on receive  $B_1$  field.



## Chapter 4 Gradient-based Electrical Properties Tomography

### 4.1 Introduction

In Chapter 3, the Helmholtz equation was utilized to develop a framework for accurately calculate absolute  $B_1$  phase and electrical properties (EP) assuming piecewise homogeneous tissue. Since the beginning when EPT concept was introduced (Haacke et al., 1991; Ulrich Katscher et al., 2009; Wen, 2003) and implemented (Liu et al., 2013; Sodickson et al., 2012; van Lier et al., 2012; Voigt et al., 2011; Zhang et al., 2013b), the homogeneous Helmholtz equation has been utilized in the majority of EPT studies. However, biological tissues may exhibit rapid spatial changes in EP due to their complicated structures. Reconstruction error will occur near boundary of different electrical properties based on the Helmholtz equation.

In this chapter, a new gradient-based EPT (gEPT) approach is proposed (Liu et al., 2014), in which the spatial gradient of EP are explicitly considered in the algorithm and utilized to reconstruct EP maps through spatial integration. Simulation studies, phantom validation and in vivo human experiments have been conducted at 7 T to investigate the gEPT algorithm, with a special focus on its enhanced boundary reconstruction and robustness against noise contamination in the context of highly refined structural details that characterize real life experiments.

A schematic diagram of the gEPT approach is shown in Figure 4.1. A multi-channel transceiver RF array coil is utilized for RF power transmission and MR signal reception. The spatial gradient of EP is derived using the magnitude and relative phase of

multiple transmit and receive  $B_1$  fields from the multiple channels. The final EP maps are reconstructed via spatial integration on the obtained gradient field.

Figure 4.1 Schematic diagram of the gradient-based electrical properties tomography using a multi-channel transceiver radiofrequency array coil.

Neglecting the  $B_z$  component of  $B_1$  field, the central equations of EPT have been derived as Eqs. (2.15) and (2.16). Taking measurable magnitude and relative phase of transmit and receive  $B_1$  field as input, the goal is to derive the unknown absolute phase, EP and gradient  $\mathbf{g}$ . We can define the relative transmit or receive  $B_1$  field as  $B_{ij}^+ = |B_{1j}^+| e^{i\phi_{ij}^+}$  or  $B_{rk}^- = |B_{1k}^-| e^{i\phi_{rk}^-}$  where  $i$  and  $k$  indicate the index of transmit and receive channel, respectively. The central equations (2.15) and (2.16) can be rewritten in the form of the relative  $B_1$  fields as

$$\begin{aligned}
-\nabla^2 B_{rj}^+ &\approx \nabla B_{rj}^+ \cdot \left[ 2i\nabla \phi_0^+ - (g_+, -ig_+, g_z) \right] \\
&+ B_{rj}^+ \cdot \left[ \omega^2 \mu_0 \varepsilon_c + i\nabla^2 \phi_0^+ - \nabla \phi_0^+ \cdot \nabla \phi_0^+ - i\nabla \phi_0^+ \cdot (g_+, -ig_+, g_z) \right]
\end{aligned} \tag{4.1}$$

and

$$\begin{aligned}
-\nabla^2 B_{rk}^- &\approx \nabla B_{rk}^- \cdot \left[ 2i\nabla \phi_0^- - (g_-, ig_-, g_z) \right] \\
&+ B_{rk}^- \cdot \left[ \omega^2 \mu_0 \varepsilon_c + i\nabla^2 \phi_0^- - \nabla \phi_0^- \cdot \nabla \phi_0^- - i\nabla \phi_0^- \cdot (g_-, ig_-, g_z) \right]
\end{aligned} \tag{4.2}$$

where  $\phi_0^+$  and  $\phi_0^-$  are the unknown absolute phase of a reference transmit and receive channel, respectively. Equations (4.1) and (4.2) can be transformed into linear equations by treating the items associated with  $B_{rj}^+$  or  $B_{rk}^-$  as a new unknown. Using a number of channels of  $B_{rj}^+$  and  $B_{rk}^-$ ,  $g_+$  and  $g_-$  can be derived from Eqs. (4.1) and (4.2) based on linear least square, respectively. To improve the reliability of the result, this procedure was repeated using each of the transmit or receive channels as a reference channel. Weighted by the magnitude of the local  $B_1$  field of the corresponding reference channel, the resulting  $g_+$  and  $g_-$  on the same voxel were combined to yield the final  $g_+$  and  $g_-$ , which were transformed into  $g_x$  and  $g_y$ .

Once the gradient  $\nabla \ln \varepsilon_c$  is obtained, with the additional information of a small number of  $S$  seed points to provide initial value, final maps of the electrical properties were reconstructed using a 2D finite-difference method (Iserles, 2009).

## 4.3 Materials and Methods

### 4.3.1 Computer Simulation

#### *Simulation Setup*

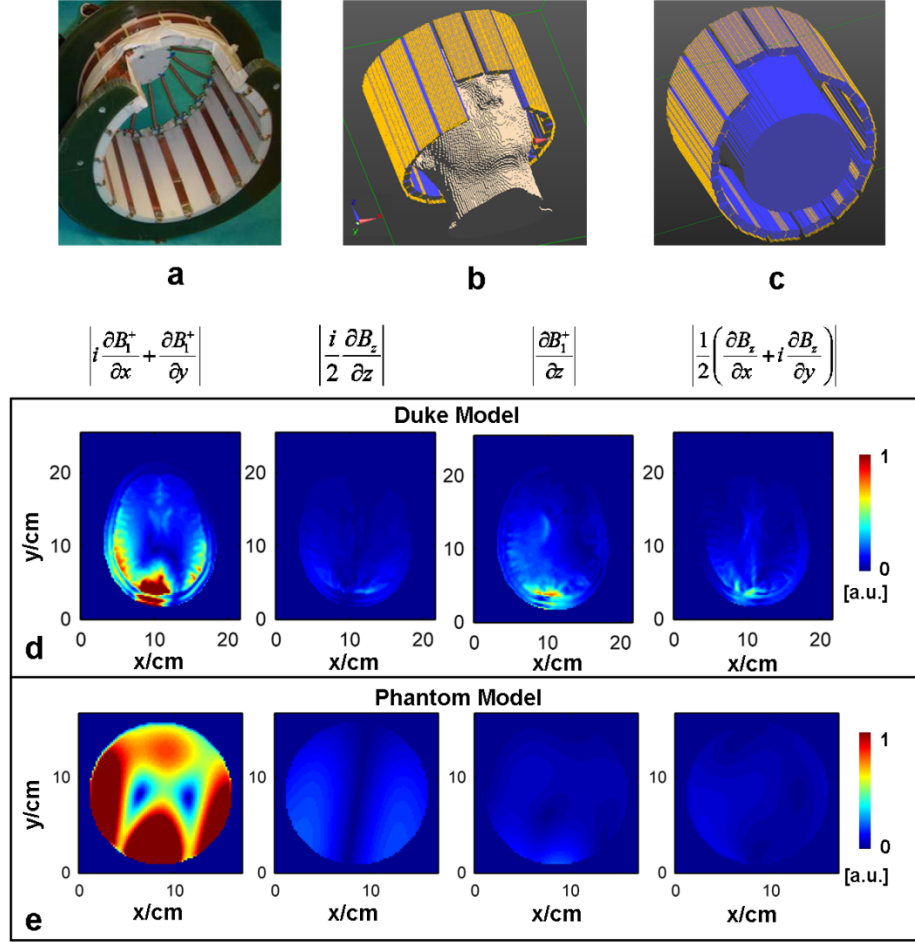


Figure 4.2 (a): Photograph of the sixteen-channel RF coil used in experiments. (b): Simulation setup of the coil and a head model. (c): Simulation setup of the coil and a cylindrical phantom model. (d) and (e): The relative magnitude of derivative components related to  $B_1^+$  or  $B_z$  in a slice near the middle of the RF coil in the z-axis of the Duke head (d) and of a homogeneous phantom model (e), respectively.

Electromagnetic simulation was performed based on the finite-difference time-domain (FDTD) method in software SEMCAD (Schmid & Partner Engineering AG, Zurich, Switzerland). A 16-channel microstrip array coil as shown in Figure 4.2 (a) (Adriany et al., 2008), which is used in the experimental part of the study, was numerically modeled and loaded with either the Duke head model of the Virtual Family as shown in Figure 4.2 (b) (Christ et al., 2010) or a head-sized phantom in Figure 4.2 (c) (diameter of 15 cm and height of 20 cm) with the average electrical properties of the

brain ( $\sigma = 0.55 \text{ Sm}^{-1}$  and  $\varepsilon = 52 \varepsilon_0$ ) at 298 MHz (Larmor frequency of proton at 7 T). For each coil element, the complex magnetic field at 298 MHz was simulated with a voxel size of  $2 \times 2 \times 2 \text{ mm}^3$ . Target EP maps, which were calculated using the simulated magnetic and electric fields based on Maxwell's equations, were employed as a ground truth to evaluate the performance of the gEPT algorithm.

### ***Evaluating Accuracy and Noise Robustness of gEPT Based on Simulation***

Using the proposed gEPT, estimated EP maps were calculated using simulated magnitude  $|B_1^\pm|$  and *relative* phase  $\Delta\phi^\pm$  maps of the 16 coil elements. A comparison was made between gEPT and the conventional EPT approach based on the homogeneous Helmholtz equation  $\nabla^2 B_1 = -\omega^2 \mu_0 B_1 \varepsilon_c$  and utilizing multiple transmit/receive RF channels (Katscher et al., 2012; Sodickson et al., 2012). To derive  $\varepsilon_c$  using the latter, simulated  $|B_1^+|$  and *absolute* phase  $\phi^+$  maps of the 16 channels (*absolute*  $\phi^+$  phase maps cannot be experimentally measured), were utilized to create 16 instances of equations  $\nabla^2 B_{1k}^+ = -\omega^2 \mu_0 B_{1k}^+ \varepsilon_c$  ( $1 \leq k \leq 16$ ), from which  $\varepsilon_c$  was calculated by minimizing the sum of the squares of the residual errors of the 16 equations.

Relative error (RE) and correlation coefficient (CC) were employed as metrics to evaluate reconstructions. For a specific spatial distribution of quantity  $q$ , the *RE* and *CC* are defined as

$$\begin{aligned}
RE_q &= \sqrt{\frac{\sum_{i=1}^L (q_{ri} - q_i)^2}{\sum_{i=1}^L q_i^2}} \\
CC_q &= \frac{\sum_{i=1}^L (q_{ri} - \bar{q}_r) \cdot (q_i - \bar{q})}{\sqrt{\sum_{i=1}^L (q_{ri} - \bar{q}_r)^2 \cdot \sum_{i=1}^L (q_i - \bar{q})^2}}
\end{aligned} \tag{4.3}$$

where  $L$  is the total number of reconstructed voxels and subscript  $r$  denotes reconstructed value. Because of technical challenges to acquire reliable  $B_1$  information in structures surrounding the brain, such as skull, subcutaneous tissues and skin, we only included three soft tissues (grey matter, white matter and cerebrospinal fluid) to evaluate EP reconstruction within the brain.

In order to account for thermal noise present in actual MRI measurements, we further investigated the behavior of gEPT under noise contamination by adding Gaussian white noise, whose variance was  $1/50^{\text{th}}$  of the magnitude of the simulated  $B_1$  field (SNR=50, determined to match experimental data), to the real and imagery parts of simulated  $B_1$  data in both Duke head and homogeneous phantom model. A comparison was carried out between gEPT and aforementioned Helmholtz-based approach in the phantom model in identical noise-contaminated  $B_1$  simulation data smoothed with a Gaussian filter.

### 4.3.2 Experiments

Experiments were carried out on a 7 T whole body MRI scanner (Siemens, Erlangen, Germany). A 16-channel microstrip array RF coil (Adriany et al., 2008), shown in Figure 4.2 (a), was utilized for all experiments, powered by  $16 \times 1\text{kW}$  amplifiers (CPC, Hauppauge, NY, USA) controlled by a remotely operated 16-channel RF

phase/amplitude gain unit. As previously described in more details (Metzger et al., 2010; Zhang et al., 2013b), global SAR was continuously monitored, with a maximum upper limit, based on International Standard IEC 60601-2-33 2010, determined from the ratio between peak local SAR and global SAR derived from electromagnetic model of the 16-channel coil loaded with a human head.

### ***B<sub>1</sub>-mapping Protocols***

Using a previously proposed hybrid B<sub>1</sub>-mapping technique consisting of a series of MRI sequences (Van de Moortele et al., 2007, 2005; Van de Moortele and Ugurbil, 2009; Zhang et al., 2013b), the magnitude  $|B_1^+|$ , proton density biased magnitude  $|\rho B_1^-|$ , and relative phase  $\phi_r^+$  and  $\phi_r^-$  were collected for the 16 transmit and receive channels. First of all, a 3D flip angle (FA) map was measured using the Actual Flip Angle technique (AFI) (Yarnykh, 2007), all channels transmitting together with a large nominal FA of 90° (phantom experiments) or 60° (in-vivo experiments). To obtain  $|B_1^+|$  and  $\phi_r^+$  for each individual channel, a series of low FA 2D GRE (gradient-recalled echo, nominal FA=10°) images were acquired with one channel transmitting at a time and all channels receiving together. The raw data from the low FA GRE was converted to  $|B_1^+|$  after being normalized by the measured 3D FA map (Van de Moortele et al., 2007). The proton density weighted magnitude  $|\rho B_1^-|$  and  $\phi_r^-$  of receive B<sub>1</sub> field were acquired via another series of 2D GRE images obtained with all channels transmitting together (using the same B<sub>1</sub> excitation configuration as the 3D AFI), with a long TR of 10s ( $\gg T_1$ ) and with a large nominal FA the same as that of 3D AFI to reach high SNR, normalized by the sine of the corresponding 3D FA map (Van de Moortele et al., 2005).

### ***Phantom Setup and Experiment***

A three-compartment 3D phantom, as shown in Figure 4.6 (e), was built out of different saline gel solutions. The EP values of the three compartments of the phantom were  $\sigma=0.34, 0.71$  and  $1.12 \text{ Sm}^{-1}$  and  $\varepsilon=77, 61$  and  $65 \varepsilon_0$  at the frequency of 298 MHz, respectively, measured with an Agilent 85070D dielectric probe kit and an Agilent E4991A network analyzer (Agilent, Santa Clara, CA, USA). The three solutions consisted of distilled water, NaCl, Sucrose,  $\text{CuSO}_4 \cdot 5\text{H}_2\text{O}$  and Gelatin in the mass ratio of 100:0.12:0:0.025:3, 100:2.54:73.97:0.025:3 and 100:2.5:49.92:0.025:3, respectively.

The phantom was positioned at the isocenter of the coil with its “nose” facing up. Two separate  $B_1$  shimming combinations were performed, one tending to reproduce a circularly polarized CP mode with  $|B_1^+|$  maximized at the center of the phantom and another one tending to reproduce a so-called CP2+ mode (Orzada et al., 2013) with  $|B_1^+|$  maximized in a peripheral ring; this strategy, somehow similar to the TIAMO approach (Orzada et al., 2013), helped to circumvent dark spots that were virtually impossible to avoid in individual  $B_1$  shimming configurations due to the overall high relative permittivity of the phantom ( $\sim 77$  in majority of the volume). Two full sets of  $B_1$ -mapping sequences were conducted using the two  $B_1$  shimming configurations described above. For each shimming configuration, the 3D AFI images were acquired with  $\text{TE}/\text{TR}_1/\text{TR}_2 = 3.23/20/120 \text{ ms}$  and two averages in 18 mins; the small FA 2D GRE images with  $\text{TE}/\text{TR} = 3.3/76 \text{ ms}$ , nominal FA of  $12^\circ$ , and ten averages in 28 mins; the large FA 2D GRE images with  $\text{TE}/\text{TR} = 3.1/10000 \text{ ms}$  and two averages in 42 mins. These acquisitions were performed in a total number of twelve 3-mm thick slices centered on the phantom



center along the  $z$ -direction, with a spatial resolution of  $1.5 \times 1.5 \text{ mm}^2$  within slices in a FOV of  $288 \times 189 \text{ mm}^2$ .

Prior to EP reconstruction, the data were smoothed using a Gaussian filter with a kernel size of  $5 \times 5 \times 3$  voxels and standard deviation (SD) of  $1.2 \times 1.2 \times 0.8$  voxels to reduce noise, with a resulting effective voxel size of  $4.8 \times 4.8 \times 6.4 \text{ mm}^3$  (see Appendix B for definition). In order to remove the proton density from the acquired  $|\rho B_1^-|$  maps, the phantom was segmented utilizing *a priori* knowledge of the spherical shape and location of its compartments, and within individual compartment a uniform  $\rho$  was assigned so as to maximize continuity of the resulting magnitude map of  $|B_1^-|$  across compartment boundaries. Utilizing two sets of  $B_1$  fields measured under the two  $B_1$  shimming settings, two maps of  $\mathbf{g}$  were calculated and merged based on the respective AFI maps. Three voxels in compartment #1 were chosen as seed points.

### ***In Vivo Human Experiments***

We studied two healthy human subjects, with signed consent forms approved by the Institutional Review Board at the University of Minnesota, using the proposed gEPT to generate EP maps in the brain in vivo. In contrast to the phantom experiment, a single  $B_1$  shimming configuration, approaching a CP mode, was sufficient to collect  $B_1$  maps in the human head without excessively weak  $|B_1^+|$  areas. The 3D AFI images were acquired with  $TE/TR_1/TR_2 = 3.23/20/120 \text{ ms}$  and one average in 9 mins; the small FA 2D GRE images with  $TE/TR = 3.3/76 \text{ ms}$ , nominal FA of  $10^\circ$ , and ten averages in 28 mins; the large FA 2D GRE images with  $TE/TR = 3.1/10000 \text{ ms}$  and one average in 21 mins. A total of twelve axial slices of  $B_1$  field data were acquired with a voxel size of  $1.5 \times 1.5 \times 5 \text{ mm}^3$  with a FOV of  $288 \times 189 \text{ mm}^2$ . A Gaussian filter with kernel size of  $5 \times 5 \times 3$

voxels and SD of  $1.2 \times 1.2 \times 0.8$  voxels was used to remove high-frequency noise in the  $B_1$  data with a resulting effective voxel size of  $4.8 \times 4.8 \times 10.7$  mm<sup>3</sup>. Using a left-right symmetrical RF array coil loaded with an approximately symmetrical normal human head, proton density  $\rho$  was estimated based on the left-right mirroring symmetry previously reported of  $\sum_i |B_{1,i}^+(x, y)| \approx \sum_j |B_{1,j}^-(-x, y)|$  where  $i$  and  $j$  indicate sixteen transmit and receive channels, respectively (Van de Moortele and Ugurbil, 2009; Zhang et al., 2013b).

## 4.4 RESULTS

### 4.4.1 Simulations

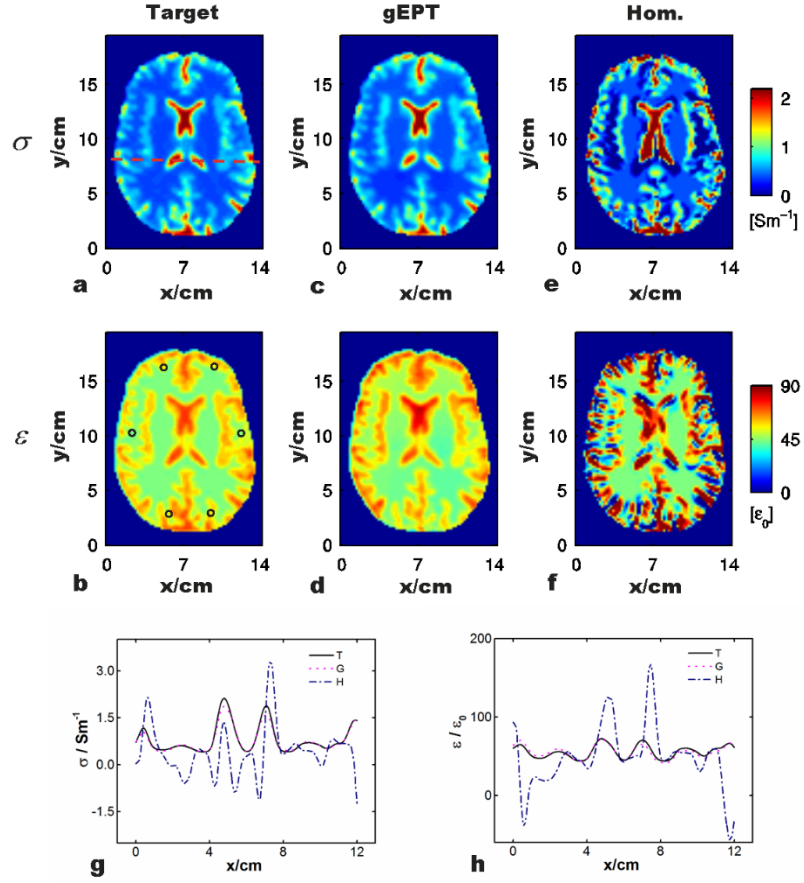


Figure 4.3 Comparison of the reconstructed electrical properties based on gEPT and homogeneous Helmholtz equation, respectively, with respect to the target values. (a) and (b): Target  $\sigma$  and  $\epsilon$ . 'o': location of seed points. (c) and (d): Reconstruction using gEPT. (e) and (f): Reconstruction based on homogeneous equation. (g) and (h): Profiles of the reconstructed  $\sigma$  and  $\epsilon$  using the two methods along the red dash line as shown in (a). 'T': target, 'G': gEPT and 'H': homogeneous Helmholtz equation.

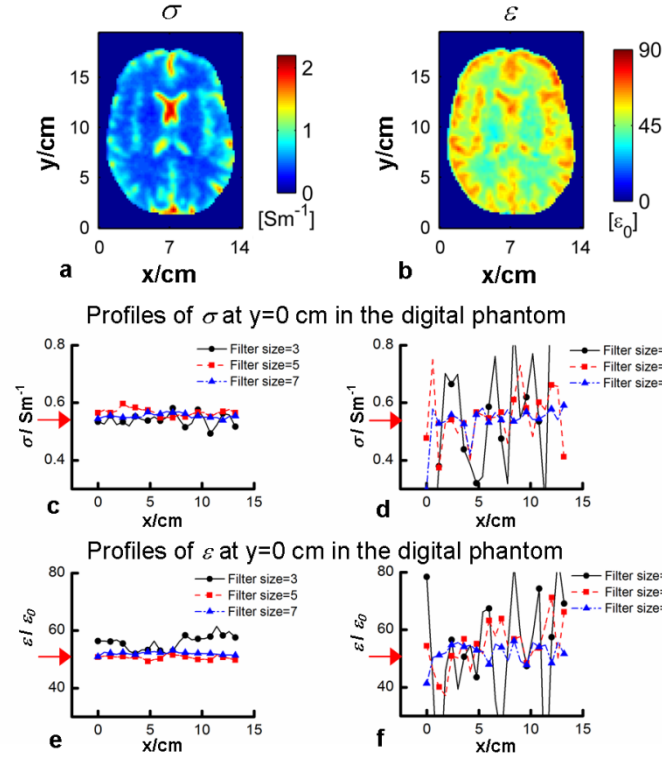


Figure 4.4 (a) and (b): Reconstruction of the electrical properties of the Duke head model using gEPT when SNR=50. Reconstruction of the electrical properties using gEPT (c) and (e) or based on the Helmholtz equation (d) and (f) in the homogeneous phantom model when SNR=50 and different Gaussian filter was applied. Red arrows indicate the true target EP values of the phantom model.

Figure 4.3(a)-(b) shows the target electrical properties in a transverse slice of the Duke head model. As marked in Figure 4.3(b) (circles), six seed points were selected evenly distributed around the periphery of the brain region for gEPT reconstruction. Figure 4.3(c)-(d) shows the results of reconstructed  $\sigma$  and  $\varepsilon$  in the same slice using the proposed gEPT under noise-free condition. Profiles of the results, along the dash line shown in Figure 4.3(a), are shown in Figure 4.3 (g)-(h) for a closer comparison to the target values. In general, it can be seen in Figure 4.3(c)-(d) that the detailed structural information present in the target maps was accurately reproduced in the reconstructed maps of  $\sigma$  and  $\varepsilon$  using gEPT; in Figure 4.3 (g)-(h), the reconstruction profiles closely

follow those of target values. Within the brain region, the overall RE and CC of the reconstruction are  $RE=8.5\%$  /  $CC=0.98$  for  $\sigma$  reconstruction, and  $RE=7.6\%$  /  $CC=0.90$  for  $\varepsilon$  reconstruction, respectively. In contrast, as shown in Figure 4.3(e)-(f) as well as in the profiles in Figure 4.3(g)-(h), results using the homogeneous Helmholtz equation exhibit substantial errors near the boundaries with  $RE=99.7\%$  /  $CC=0.38$  for  $\sigma$  reconstruction and  $RE=58.0\%$  /  $CC=0.25$  for  $\varepsilon$  reconstruction, respectively. The reconstruction performance of using gEPT under noise situation (SNR=50) based on the Duke head model is depicted in Figure 4.4(a)-(b). A 3D Gaussian filter, with a kernel size of 3 voxels and SD of 0.8 voxels in all three directions, was utilized to smooth the data before gEPT reconstruction. As can be seen in Figure 4.4(a)-(b), the resulting maps using gEPT show consistency in comparison with the target images in Figure 4.3(a)-(b). Overall  $RE=15.7\%$  and  $CC=0.96$  for the reconstructed  $\sigma$ , and  $RE=10.2\%$  and  $CC=0.80$  for the reconstructed  $\varepsilon$  were achieved, respectively, with the results for individual tissues summarized in Table 4.1. Note the slightly smoothed patterns of the reconstructed EP maps, especially the permittivity, that we attributed to the use of the smoothing filter.

Table 4.1 Relative errors and correlation coefficients of EP reconstruction using gEPT in the Duke head model based on various assumptions when SNR=50.

<i>REs</i>		SNR=50 without $B_z$		SNR=50 without $B_z$ Estimated PD		SNR=50 with $B_z$	
GM	$\sigma$	13.6%		13.6%		13.4%	
	$\varepsilon$	9.3%		11.3%		6.3%	
WM	$\sigma$	12.2%		11.6%		11.7%	
	$\varepsilon$	8.4%		10.6%		8.2%	
CSF	$\sigma$	19.1%		19.3%		18.7%	
	$\varepsilon$	16.2%		14.9%		6.6%	
Total ( <i>REs/CCs</i> )	$\sigma$	15.7%	0.96	15.7%	0.96	15.3%	0.96
	$\varepsilon$	10.2%	0.80	11.6%	0.82	7.1%	0.90

For the numerical homogeneous phantom study, Gaussian filters of different sizes were utilized to smooth the noise-contaminated  $B_1$  data (SNR=50), including 3-, 5- and 7-voxel kernels with corresponding SD of 0.8, 1.2 and 1.6 voxels. Using gEPT, a voxel in the center of the slice of interest was used as the seed point. The results shown in Figure 4.4(c)-(f) indicate that, compared to the Helmholtz-based approach (even though the latter is free of boundary errors in this homogeneous phantom model), gEPT is more robust against measurement noise, and does not require the use of strong Gaussian filter with large kernel size and/or SD value to reduce the noise level. Using gEPT, no significant accumulation of noise-induced error was observed as the distance increases from the central seed point.

As can be observed in Figure 4.2, in the center slice of the Duke head or of the phantom model, the component related to the x- and y-direction derivatives of  $B_1^+$  is the dominant one among the coefficients of Eq. (2.13), and similar observations can be made for the receive  $B_1$  field. It was thus considered reasonable to ignore  $B_z$ -related components to calculate the solution of Eq. (4.1) and (4.2). In order to further evaluate the impact of omitting these components, gEPT based reconstructions were performed

while also using  $B_z$ , obtained from simulations, with SNR=50. As can be seen in Table 4.1, the corresponding conductivity results were similar to those obtained without  $B_z$ , both for individual tissue and overall brain, while the corresponding permittivity results slightly deteriorated.

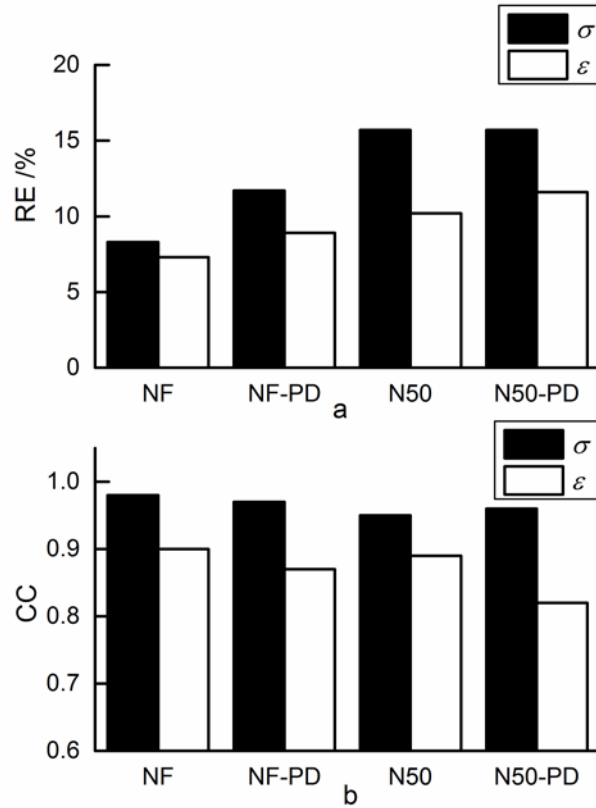


Figure 4.5 Summary of RE and CC of gEPT under different conditions. “NF”: noise-free with no proton density bias. “NF-PD”: noise-free with proton density estimated by symmetry assumption. “N50”: noisy condition SNR=50 with no proton density bias. “N50-PD”: noisy condition SNR=50 with proton density estimated by symmetry assumption. (a): RE. (b): CC.

The impact of empirically estimating proton density in Duke head based on the symmetrical assumption on the gEPT performance is shown in Table 4.1 and Figure 4.5. As can be seen, in the most realistic scenario, i.e. with unknown proton density and added measurement noise, the RE for  $\sigma$  and  $\epsilon$  were 15.7% and 11.6%, and CC 0.96 and 0.82,

respectively. In comparison with the noise-free situation, the effect of empirical proton density estimation was not as significant as the effect of measurement noise.

#### 4.4.2 Phantom Studies

The estimated proton densities were 1.00, 0.64 and 0.74 for the three compartments of the phantom used as shown in Figure 4.6 (e), respectively. In Figure 4.6, examples of the extracted gradient of relative phase  $\phi_{r,6}$  (between channel #6 and #1) and  $\mathbf{g}$  are compared to the target values, showing high accuracy even in the vicinity of the boundaries where EPT algorithms based on the homogeneous Helmholtz equation typically tend to fail. Three voxels within component #1, one located at the iso-center and two near the circumference, were chosen as the seed points to provide EP information using their probe-measured values. The reconstructed EP maps are shown in Figure 4.6(g)-(i) and summarized as  $\sigma=0.34\pm0.07$ ,  $0.71\pm0.08$ , and  $0.97\pm0.13 \text{ Sm}^{-1}$  /  $\varepsilon=75.6\pm2.7$ ,  $63.3\pm5.3$  and  $64.3\pm3.2 \varepsilon_0$  for the corresponding components of the phantom, respectively, depicting large agreement compared with measurements using the dielectric probe.



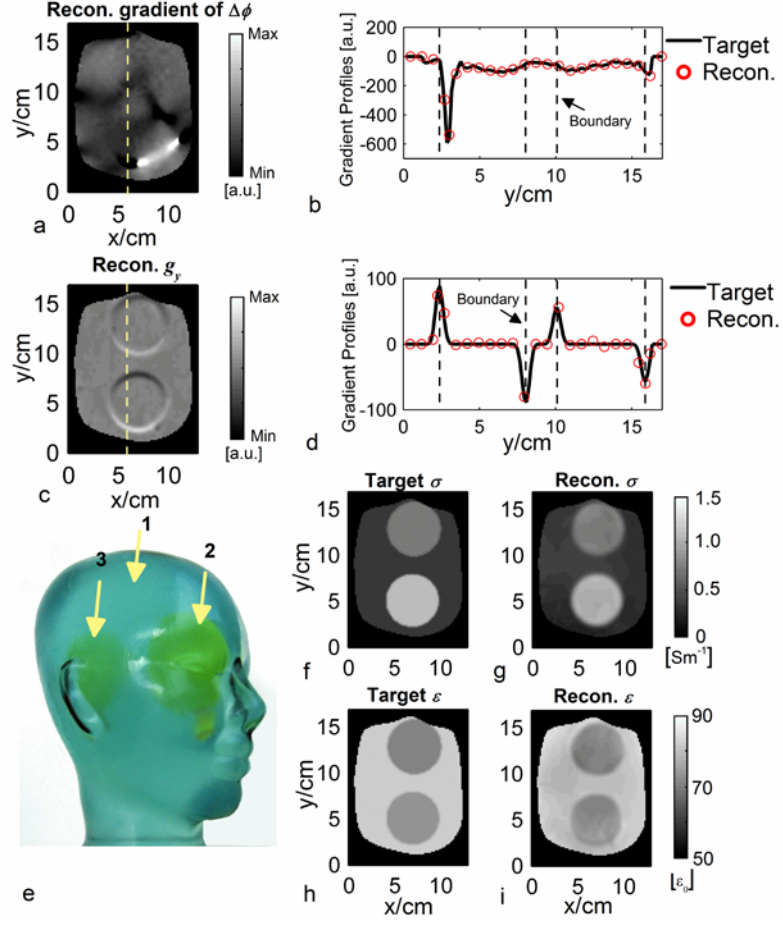


Figure 4.6 Physical phantom results. (a): Reconstructed images of  $\partial\phi_{r1,6}/\partial y$ .  $\phi_{r1,6}$ : relative phase between channel #6 and #1. (b): Profiles of reconstructed  $\partial\phi_{r1,6}/\partial y$  and the MRI measurement as the target along the dashed line in (a). (c): Reconstructed images of imagery part of  $\mathbf{g}_y$ . (d): Profiles of reconstructed imagery part of  $\mathbf{g}_y$  and the probe measurement as the target along the dashed line in (c). (e): Photograph of the phantom. Arrows indicate the interior components. (f) and (h): The target images of  $\sigma$  and  $\epsilon$ , respectively. (g) and (i): The reconstructed images of  $\sigma$  and  $\epsilon$  using gEPT, respectively.

### 4.4.3 In Vivo Human Experiments

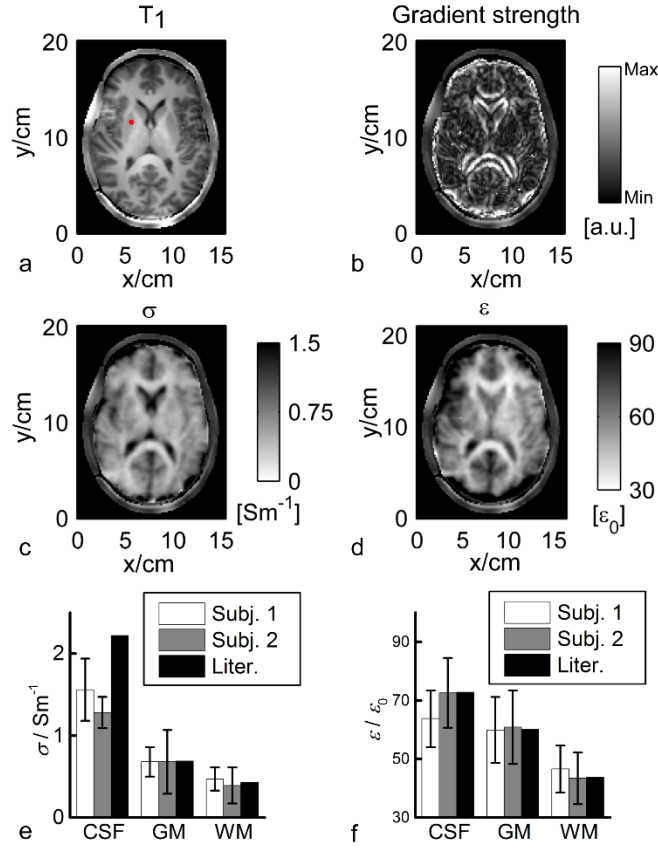


Figure 4.7 In vivo experimental results in humans. (a): T<sub>1</sub>-weighted image. The red dot indicates the seed point. (b): Reconstructed magnitude image of the real part of  $\nabla \ln \epsilon_c$ . (c): Reconstructed  $\sigma$ . d: Reconstructed  $\epsilon$ . e and f: Summary of the reconstruction results of  $\sigma$  and  $\epsilon$  of the two human subjects with reference to the literature values.

Figure 4.7 shows in vivo results in two healthy human subjects. As indicated by the red dot in Figure 4.7(a), one seed point within the right putamen was used to provide the initial EP information, assigned with  $\sigma$  and  $\epsilon$  of grey matter based on previously reported ex vivo measurement (S. Gabriel et al., 1996a). In the brain, transverse slice #6 was chosen to illustrate the results of gEPT because it is the closest to the middle of the RF coil along  $z$ -direction, where  $B_z$  variations are expected to be the smallest and thus can be ignored. From subject #1, magnitude of the extracted  $\nabla \ln \epsilon_c$  (real part) is shown in

Figure 4.7 (b), as well as the estimated  $\sigma$  and  $\varepsilon$  in Figure 4.7(c) and (d), respectively. When comparing Figure 4.7(a) (T1w image) with Figure 4.7(b) (gradient strength derived from measured  $B_1$  maps), one can appreciate the spatial correspondence between contours of anatomical structures (ventricles, gyri/sulci) and local high values of estimated gradient. Likewise, the conductivity and permittivity maps shown in Figure 4.7 (c) and (d) reconstitute with remarkable accuracy the spatial distribution of white matter, grey matter and ventricles, as well as the curvature of the cortex. Importantly, EP imaging results from two more adjacent slices further confirm these observations, as shown in Figure 4.8, as structural variations from one slice to another identified on T1w images can be followed on corresponding EP maps as well. As anticipated, errors arise at the periphery of the brain when approaching the vicinity of the skull as almost no MR signal is detected in bones with standard MR sequence so that no reliable  $B_1$  information could be collected. Using a segmentation of the brain tissues obtained with the T1w image, the statistics (mean $\pm$ SD) for three types of tissues, grey matter (GM), white matter (WM) and cerebrospinal fluid (CSF) on slice #6 of the two subjects were summarized in Figure 4.7 (e) and (f) in comparison with literature-reported values (S. Gabriel et al., 1996a). Note the high consistency between the gEPT reconstructed values and ex vivo measurements. One exception concerns the mean conductivity of CSF, which is lower than the literature value. Factors, such as partial volume effect (large difference between conductivity of CSF and surrounding tissues) or the weaker average magnitude of  $B_1$  for each coil element at the center of the brain, with reduced SNR, could contribute to the drop in value of the mean reconstructed conductivity in CSF.

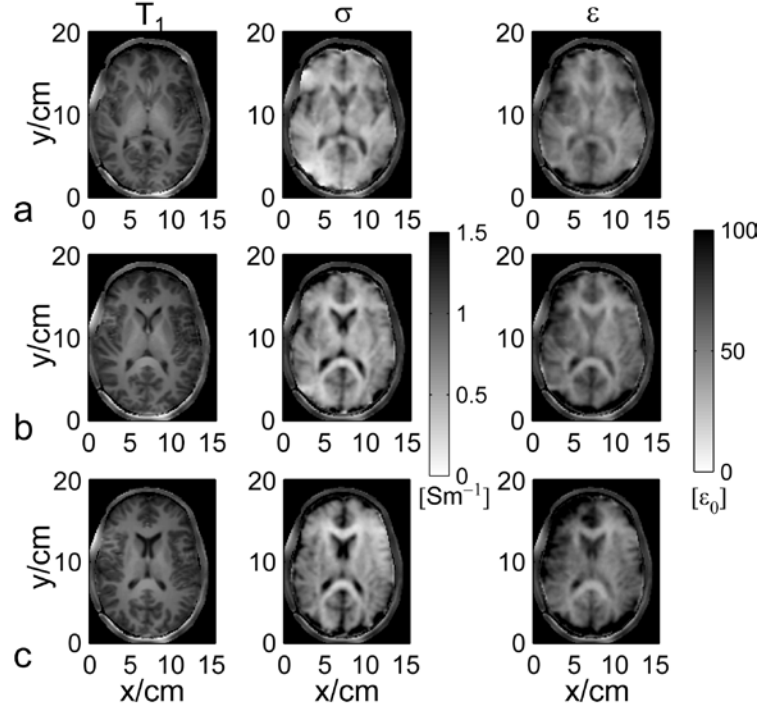


Figure 4.8 (a)-(c): The reconstructed electrical properties in three transverse slices in the brain of human subject #1 using gEPT with respect to the  $T_1$ -weighted images.

## 4.5 Discussion

The fundamental novelty in our proposed gEPT approach consists in recognizing and explicitly utilizing the fact that the gradient  $\mathbf{g}$  bears the necessary information to reconstruct EP boundaries. Although in vivo EPT in the human brain have been reported, at different magnetic fields (1.5, 3 and 7 T) and with different RF coil designs (Sodickson et al., 2012; van Lier et al., 2013; Voigt et al., 2011; Zhang et al., 2013b), it is our understanding that these maps still suffer from significant deviations in EP values especially near tissue boundaries as a result of the homogeneous Helmholtz equation (Seo et al., 2012). In the proposed gEPT method, measurable information of both  $B_1^+$  and  $B_1^-$  fields from a multi-channel transceiver RF coil was acquired and utilized to solve our central equations, and the derived gradient field  $\mathbf{g}$  was explicitly employed to reconstruct EP maps. We believe that our results (see Figure 4.7 and Figure 4.8) demonstrate a

substantial improvement in the quality of EP maps obtained in vivo on human brain imaging. In attempting to address the boundary issue, an adaptive-filter approach has been proposed and in vivo results have been acquired (Huhndorf et al., 2013). However, it can be challenging to sustain its fidelity in small inhomogeneous regions because its effectiveness heavily relies on the accuracy of a pre-segmentation of imaged objects.

Another merit of our proposed gEPT algorithm comes from the inherent low-pass filtering property (noise reduction) of *integration* on the gradient  $\mathbf{g}$  while most other studies obtained EP maps directly through *differentiation* on  $B_1$  fields without explicitly utilizing  $\mathbf{g}$  information. MR signals are by nature contaminated with noise. Some insight into the high sensitivity of conventional non-gradient-based EPT to measurement noise can be gained by looking at both the homogeneous and inhomogeneous Helmholtz equations: it can be seen that the Laplacian operator will amplify errors that then propagate linearly into the complex permittivity  $\epsilon_c$ , and its derivative  $\mathbf{g}$ . Although a strong spatial filter can attenuate measurement noise without significantly distorting the  $B_1$  field, subsequent EP reconstruction will significantly be affected by such smoothing procedure, especially for the Helmholtz equation-based methods (Seo et al., 2012). As shown in Figure 4.4 (c)-(f) in a homogeneous phantom model, with gEPT, the employed integration method over  $\mathbf{g}$  largely suppresses the amplification of noise-related errors that are still observed with the Helmholtz equation-based method, which is free of boundary errors in the homogeneous model. In this study, the gEPT method which only utilizes the derived  $\mathbf{g}$  separately from  $\epsilon_c$  in the central equation, has been shown with largely improved imaging performance. Nonetheless, it is anticipated that utilizing information

carried in both  $\varepsilon_c$  and  $\mathbf{g}$  may further improve robustness and reliability of the reconstruction.

The increased performance of gEPT against measurement noise will in return contribute to improved boundary reconstruction by eliminating the use of strong spatial filter on  $B_1$  field, so that  $B_1$ -maps could be exploited at higher spatial resolution. As a result, significant improvement in EP map quality may be obtained in vivo. In the current study, additional factors relating with the use of high  $B_0$  field (7 T) may contribute to the robust performance of gEPT even in the presence of measurement noise, such as enhanced curvature of RF field caused by shortened wavelength and boosted SNR of MR signal; likewise, redundant transmit and receive  $B_1$  information resulting from the use of multiple RF channels may give an advantage to our approach. In the future, it will be worth investigating different integration methods to reconstruct EP from its gradient  $\mathbf{g}$ , such as the 2-D layer potential technique utilized in MREIT (Oh et al., 2003b) and MAT-MI (Li and He, 2010).

The assumptions made to establish the central equation are prone to two main sources of errors. The first source of error comes from the elimination of  $B_z$ , a quantity that cannot be measured with existing MR techniques. Using the microstrip RF coil with a uniform geometry along the  $z$ -direction, it was demonstrated that only minimum  $B_z$ -related components are expected in a group of transverse slices positioned at the middle of the coil along the  $z$ -axis as shown in Figure 4.2 (d)-(e); it was furthered shown in Table 4.1, using noise-contaminated  $B_1$  data, that when actually including  $B_z$  (as known), the improvement of gEPT was not significant compared to the case eliminating  $B_z$ . Besides, the assumption that  $B_z$  can be ignored has been adopted in previous EPT studies

(Katscher et al., 2012; Zhang et al., 2013b) and is supported by simulation results using EM modeling (Zhang et al., 2012).

Another modeling error comes from the method of proton density estimation utilized in receive B<sub>1</sub> magnitude mapping. Till now, there has been no direct technique in proton density imaging at UHF; the previously reported approach (Van de Moortele and Ugurbil, 2009; Zhang et al., 2013b), which is based on the symmetrical assumption between the transmit and receive B<sub>1</sub> field, has been employed in this study. As shown in Figure 4.5, when using a left-right symmetric RF coil and an approximately symmetric normal human head model, the left-right symmetry assumption between the summations of the magnitude of transmit and receive B<sub>1</sub> fields performs as a feasible alternative to extract proton density for the purpose of gEPT. In practice, asymmetrical experimental conditions, such as shifted object position from the symmetric axis or unbalanced gains of RF signal in different receive channels, need to be accounted for to minimize errors from less accurate proton density estimation. The symmetry assumption can also be prone to inaccuracies if the imaged sample presents noticeably asymmetrical EP distribution.

A full framework describing EPT without resorting to any assumption has been proposed in another study (Sodickson et al., 2013). Although this general theory may provide a formalism to extract missing components, e.g.  $B_z$  and proton density, it remains to be demonstrated how this theoretical approach could be fully translated into experimental settings. With our proposed method we were able to demonstrate in-vivo EP maps carrying a remarkable accuracy of tissue's electrical properties that include a depiction of underlying anatomical structures (white and grey matter, ventricles) without

significant deterioration due to either measurement noise or boundary artifact while utilizing standard MR imaging sequences.

As explained in the Methods section, some seed point(s) with known EP values is (are) needed to convert the estimated gradient into absolute EP maps. Evaluation in numerical simulation indicated that the performance of gEPT is fairly stable regarding to variable seed point locations and errors in the assigned EP value of chosen seed points (results not shown here). As one would expect, the more seed points are utilized, the more reliable and stable results can be achieved. For future in vivo application, the EP values of a few seed points could be obtained from brain regions expected to exhibit relatively smooth local EP distribution (i.e. no sharp boundaries), identified on standard anatomical MR images (e.g. large white matter bundles). In these locations, homogeneous-Helmholtz-based EPT methods could be utilized to measure absolute EP values in these seed points, even though these methods would likely fail in the vast fraction of brain tissues presenting sharp EP boundaries. It is worth emphasizing that more advanced algorithms could advantageously combine the advantage of gEPT together with those of other EPT algorithms for a more integrated approach and improved performance.

In summary, we have developed a novel gradient-based MR electrical properties tomography (gEPT) approach, and demonstrated that our gEPT significantly improved in vivo EP maps of the human brain. The assumptions regarding the unknown  $B_1$  components were evaluated and shown to be valid on the symmetrical human head using the head coil with stripline channels in parallel with the  $z$ -direction. The gEPT algorithm especially provides greatly enhanced boundary reconstruction and robustness to



measurement noise. By generating more accurate and more stable in vivo EP maps, the gEPT method promises to help develop a more significant role of EPT in the investigation of fundamental aspects of tissues, clinical diagnosis and SAR prediction.

## **Chapter 5 In Vivo Imaging of Animal Tumor Model**

### **5.1 Introduction**

Based on the measured distribution of RF field during MRI scan, EPT provides a convenient way for noninvasive and in vivo imaging of the electrical properties of biological tissue at Larmor frequency with high spatial resolution. One of the potential applications of imaging tissue's electrical properties is tumor diagnosis and characterization. In comparison with normal tissues, significant change of electrical properties in malignant tissues have been reported in different organs based on ex vivo dielectric measurement, including breast (Joines, 1994; Surowiec et al., 1988), liver (Haemmerich et al., 2003; Hu et al., 2011), etc. Those changes can be attributed to changes in water content, tissue electrolyte, cell volume fraction, cell membrane permeability, presence of necrosis, etc (Foster and Schwan, 1989; Schwan, 1957). Therefore, electrical properties can be potentially developed as an imaging contrast to differentiate normal and malignant tissue, and EPT can be a promising candidate owing to its convenience and high spatial resolution.

Based on the homogeneous Helmholtz equation and half-transceiver-phase (HTP) assumption, there have been several EPT applications for in vivo imaging the electrical properties of tumor in human. Two groups (Katscher et al., 2015a; Shin et al., 2014) both applied the phase-based conductivity estimation method (Voigt et al., 2011) to study malignant and benign breast tissue and found significantly different conductivity between them. Another group (Balidemaj et al., 2015a, 2015b) studied cervical tumor; their results showed 10~22% difference of averaged conductivity compared to nearby muscle tissue.

However, using the Helmholtz equation and HTP assumption, the result is subjective to impact of boundary artifact and phase error. In order to reduce boundary artifacts, Katscher et al. and Shin et al. utilized certain adaptive filtering approaches based on a reference image to avoid calculation of derivatives across tissue boundary. In their results, considerable deviation of conductivity in malignant tissue was observed, which could be due to bias induced by the reference image.

Preclinical imaging based on small-animal models has two advantages for studying tumor using EPT. First of all, it provides a bridge to understand the bulk electrical properties of tissue and underlying molecular and cellular structures. Secondly, it has increased repeatability because of better control on the desired tumor type and growth progress and reduced interference from other biological process. The HTP and Helmholtz equation-based EPT approaches are difficult to assess small animals' electrical properties because human birdcage coil is not suitable for studying small animals, or boundary artifact is prone to happen in small animal anatomy. The proposed gradient-based EPT approach as introduced in Chapter 4 in this thesis has high resistance to measurement noise, reconstructs EP boundary based on derived gradient and does not rely on any phase assumption. Therefore, it can potentially be well suited for preclinical EPT studies.

In this chapter, an eight-channel transmission line array transceiver RF coil will be developed to reach close to the body of animals, and the obtained  $B_1$  fields will be applied to reconstruct the electrical properties using the previously proposed gEPT algorithm. Copenhagen rats bearing subcutaneous tumor will be used to study the electrical properties. The experimental setup will also be validated using controlled

animal-mimicking phantom in comparison with measured electrical properties using a dielectric probe.

## 5.2 Materials and Methods

### 5.2.1 Image Reconstruction Algorithm

In the previous chapter, the equations about distribution of electrical properties and  $B_1$  field have been derived. Using  $B_1$  field data from multiple transmit or receive channels, the gradient of electrical properties can be derived. As shown in Chapter 4, utilizing EP gradient, imaging quality can be significantly improved by reducing artifacts near tissue boundaries and noise effect. Given gradient field  $\mathbf{g}$  of EP and certain initial EP map defined as  $\epsilon_{c(0)}$ , an iterative approach can be taken to derive the final EP map as

$$\epsilon_{c(n)} = \min_{\epsilon_c} \left( \left\| \mathbf{G}_x \cdot \ln \epsilon_c - \mathbf{g}_x \right\|^2 + \left\| \mathbf{G}_y \cdot \ln \epsilon_c - \mathbf{g}_y \right\|^2 + \lambda \left\| \ln \epsilon_c - \ln \epsilon_{c(n-1)} \right\|^2 \right) \quad (5.1)$$

where the EP solution  $\epsilon_{c(n)}$  in the  $n$ th step is obtained by minimizing a cost function which is caused by the deviation of the solution from the calculated gradient ( $\mathbf{g}_x$  and  $\mathbf{g}_y$ ) and the derived EP solution  $\epsilon_{c(n-1)}$  in the  $(n-1)$ th step. In detail,  $\mathbf{g}_x$  and  $\mathbf{g}_y$  are the gradient of logarithm of EP in the x- or y-direction calculated from multi-channel  $B_1$  fields, including all the pixels in the ROI,  $\mathbf{G}_x$  and  $\mathbf{G}_y$  are differential operators to derive the corresponding gradient from an EP map, and  $\lambda$  is a constant that regularizes the solution to make a compromise between the input map and the gradient field.  $\lambda$  can be determined following the L-curve method. In this study,  $\epsilon_{c(0)}$  is chosen to be a constant based on the probe-measured EP of tumor and normal tissue.

### 5.2.2 RF Coil Construction

An 8-channel transmission-line-array (TLA) coil was built to fit the size of the animal for better SNR and loading purposes. The transmission line shape of elements was chosen to minimize  $B_z$  component of the RF field. Figure 5.1 shows a cross-section view of the RF coil's structure and a picture of the physical coil, with a similar principle and structure to previously developed TLA coils for human imaging (Adriany et al., 2008, 2005). Eight elements were distributed uniformly around the tube. Each element consists of a thin copper conductor and an RF shield, which can improve transmit efficiency and SNR, on each side of a round Teflon tube. A small gap between the neighboring RF shields exists to reduce the effect of eddy current induced by the switching gradient field of MRI. The Teflon tube has an inner diameter of 10 cm and an outer diameter of 12.7 cm. The length of the tube, conductors and shields is 10 cm. A  $50\Omega$  coaxial cable sends RF power to each element through an adjustable matching/tuning capacitor network. The matching and tuning capacitors have a variable capacitance in the range of 0~10 pF (NMNT 12-6; Voltronic, NJ, USA). For the purpose of EPT reconstruction, it is desirable to have distinctive  $B_1$  patterns between coil elements. Therefore, each element was decoupled from its nearest neighbors using decoupling capacitors which were connected between the nearby conductors and shields, respectively. The value of decoupling capacitors were adjusted when the coil was loaded with a phantom with electrical properties of  $\sigma=0.6$  S/m and  $\epsilon=60 \epsilon_0$  and fixed thereafter.

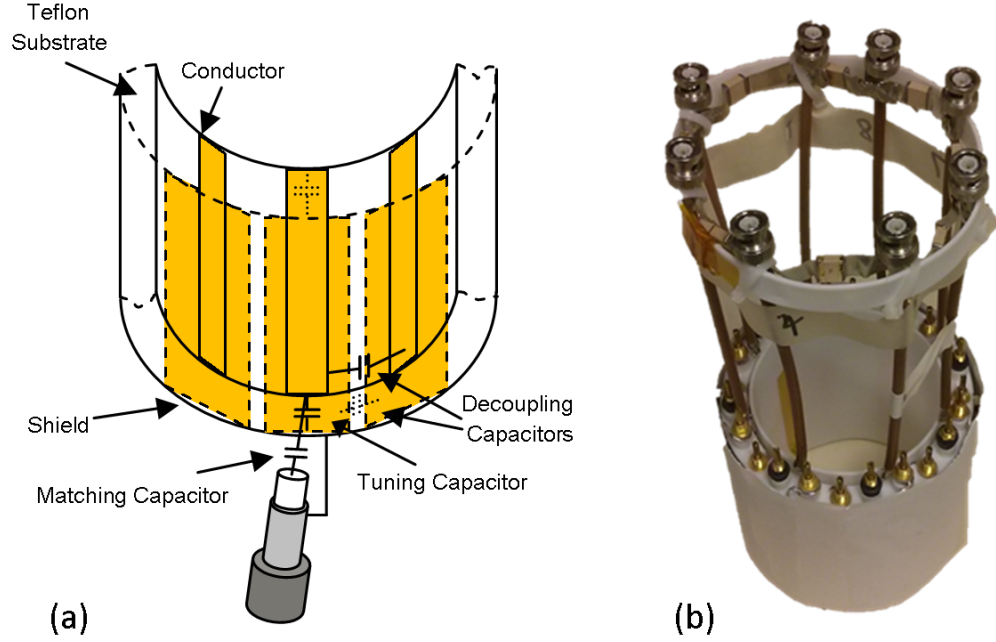


Figure 5.1 (a) A cross-section view of the RF coil structure showing examples of three elements and the tuning/matching/decoupling network. (b) Picture of the RF coil.

### 5.2.3 MRI Techniques

Experiments were carried out on a 7 T whole body MRI scanner (Siemens, Erlangen, Germany). The home-built 8-channel TLA coil as introduced in section 5.2.2 was utilized for all experiments, powered by  $8 \times 1\text{kW}$  amplifiers (CPC, Hauppauge, NY, USA) controlled by a remotely operated 16-channel RF phase/amplitude gain unit. During the experiment, the longitudinal axis of the RF coil was aligned in parallel with the direction of the main magnetic field. The sample was positioned on the center of the coil with the slices of interest near the middle of elements in the z-direction. Data including magnitude and relative phase of the transmit  $B_1$  field from each channel was acquired for calculation of EP gradient field  $g_+$ . First of all,  $B_1$  shimming was performed to maximize transmit  $B_1$  magnitude within the ROI. The resultant flip angle map was acquired with the Actual Flip-angle Imaging (AFI) technique (Yarnykh, 2007). Secondly,

a series of small flip-angle GRE sequences (Van de Moortele et al., 2007) with TR=300 ms and TE=3.3 ms was carried out for the magnitude and relative phase of individual transmit  $B_1$  channel when one channel transmitted after another. The previously acquired flip angle map under the  $B_1$ -shimming mode was utilized as a reference to calculate the magnitude of individual transmit  $B_1$  field. The gain of each transmit RF power amplifier was adjusted so that each transmit channel has a similar maximum  $B_1$  magnitude within the ROI while the corresponding maximum flip angle was controlled to be less than  $10^\circ$ . All  $B_1$  data was acquired with a pixel size of  $1.125 \times 1.125 \text{ mm}^2$  in the axial slice and slice thickness of 2 mm.

After one set of transmit  $B_1$  data was acquired, the entire setup including the sample and RF coil was flipped precisely  $180^\circ$  relative to the  $B_0$  direction in the horizontal plane. The previous  $B_1$ -mapping procedures were repeated to acquire another set of transmit  $B_1$  data. Calculation of the EP gradient from the second  $B_1$  data set equivalently provided  $g_-$  information of the sample in the same angle of view as that before the setup was rotated. Combining the calculated  $g_+$  and  $g_-$  will lead to the full gradient field of  $g_x$  and  $g_y$ .

In the in vivo experiment,  $T_1$ -weighted anatomical images (Van de Moortele et al., 2009), which are unbiased for proton density,  $T_2^*$  contrast and RF coil receive  $B_1$  sensitivity, were acquired to provide the reference for differentiating tumor and normal tissue.

#### **5.2.4 Phantom Construction**

The aforementioned imaging algorithm and experiment setup were first validated in an experiment using a phantom mimicking experiment animals. A cylindrical phantom

containing two compartments of different saline gel solutions was built. The outer diameter of the phantom was 5.5 cm, and its length was 10 cm, similar to the overall size of utilized animals. The main body (compartment #1) of the phantom was filled with a gel solution including Agar, NaCl,  $\text{NiCl}_2 \cdot 6\text{H}_2\text{O}$  and deionized water with a mass ratio of 1.2:0.453:0.01:100. The electrical properties, measured with an Agilent 85070E dielectric probe and E5061B network analyzer (Agilent Technologies, Santa Clara, CA, USA) at 300MHz, were  $\sigma=0.915$  S/m and  $\varepsilon=79 \varepsilon_0$ . A small balloon with a diameter about 2.5 cm (compartment #2), positioned inside the main body as shown in Figure 5.5(b), was filled with a gel solution including Agar, NaCl,  $\text{NiCl}_2 \cdot 6\text{H}_2\text{O}$  Sucrose (S8501-5KG, SIGMA) and deionized water with a mass ratio of 1.2:2.36:0.01:50:100, and the measured electrical properties were  $\sigma=1.19$  S/m and  $\varepsilon=68.2 \varepsilon_0$ .

### **5.2.5 Animal Preparation and Tumor Model**

AT-1 cells derived from a spontaneous Dunning R-3327 rat prostatic cancer are used in this study. The cell line was obtained from John T. Isaacs (John Hopkins University Medical School) (Isaacs et al., 1986). The cells were culture in RPMI 1640 (with 584 ml/L L-Glutamine, Gibco), supplement with 10% FBS (Fetal Bovine Serum, Gibco), Pen Strep (100 U/ml penicillin and 100ug/ml streptomycin, Gibco) and 250nM DXMT (Dexamethasone, Sigma-Aldrich). Cells were maintained in 37°C and 5%  $\text{CO}_2$ . Cells were sub-cultured by applying 0.05% trypsin - 0.53 mM EDTA (Invitrogen) for 5 minutes to detach the cells when reaching 80% in flasks. Cells in log phase of growth (70% confluent) were harvest for tumor inoculation. Cells were rinsed, centrifuged and resuspended by PBS (Phosphate-buffered saline, Gibco) twice, into  $2 \times 10^7$  cells/ml cell suspension.



All animal procedures and care were approved by the University of Minnesota Institutional Animal Care and Use Committee (IACUC) in accordance with federally approved guidelines. Male Copenhagen rats weighting 350-400 g (Charles River Laboratories) were injected with  $2-3 \times 10^6$  cells in 100  $\mu$ L of PBS subcutaneously over the dorsal flanks over the hind limbs under general anesthesia. Experiments were performed 3–5 week after grown to 2-3 cm in the largest dimension.

### **5.2.6 In Vivo Experiment**

Each animal was initially anesthetized in an induction chamber with 5% isoflurane mixed in 70% medical air and 30% oxygen, then maintained during imaging via a nose cone (Kent Scientific) at 1-2% isoflurane. Animal heating was achieved by heating pad during preparation and hot water surrounding the animal holder during MR imaging. The temperature of water flowing through tubing around the animal was controlled by a thermostat integrated with water bath circulator (NESLAB RTE 7, Thermo Scientific). The respiratory rate and body temperature were monitored by a MR-compatible small animal monitoring and gating system (SA Instruments) during the procedures. After the experiment, the animal was euthanized by carbon dioxide inhalation. Immediately following euthanasia, measurement of tissue's electrical properties was performed directly on tumor and surrounding tissue using an Agilent 85070E dielectric probe and E5061B network analyzer (Agilent Technologies, Santa Clara, CA, USA) with opened skin covering the tumor region.

### **5.2.7 Histology**

Tumor samples were fixed by 10% buffered formalin (Sigma-Aldrich) for 48-72 hours, transferred into 70% Ethanol (Decon Labs). The samples were then embedded in

paraffin, sectioned at 5  $\mu\text{m}$  and stained with hematoxylin–eosin (H&E). 40X magnification images were obtained by a digital microscope (ScanScope XT digital slide scanner, Aperio). Histologic images were processed by Aperio ImageScope (Leica Biosystems).

## **5.3 Results**

### **5.3.1 RF Coil Performance**

Before imaging experiments, the RF coil was evaluated based on its scatter matrix using a network analyzer. The results show that satisfactory matching and tuning of all channels can be obtained by adjusting the corresponding capacitors, and the  $S_{11}$ s of all channels were achieved below -20 dB. It was found that the decoupling capacitor network between neighboring conductors and RF shields significantly minimized the electromagnetic coupling of nearest neighboring channels compared to the approach using single decoupling capacitor connecting to either conductors or shields. Using this dual decoupling capacitor strategy, a decoupling between nearest neighbors better than  $S_{12} = -15$  dB was achieved. The noise correlation matrix for all channels was experimentally measured in a noise measurement on the 7T scanner. Figure 5.2 shows a noise correlation matrix when the coil was loaded with a tissue mimicking phantom. The highest coupling happens between the next nearest neighboring channels, such as between channel #5 and #7, #6 and #8, #2 and #8. After the decoupling capacitors were adjusted when loaded with a phantom, each channel can be tuned and matched to 298 MHz without effecting other channels' performance. Figure 5.3 exhibits an example of mapped transmit  $B_1$  field distribution of individual channels. Distinctive  $B_1$  variation

patterns can be observed, which is essential for the performance of multi-channel EPT algorithms.

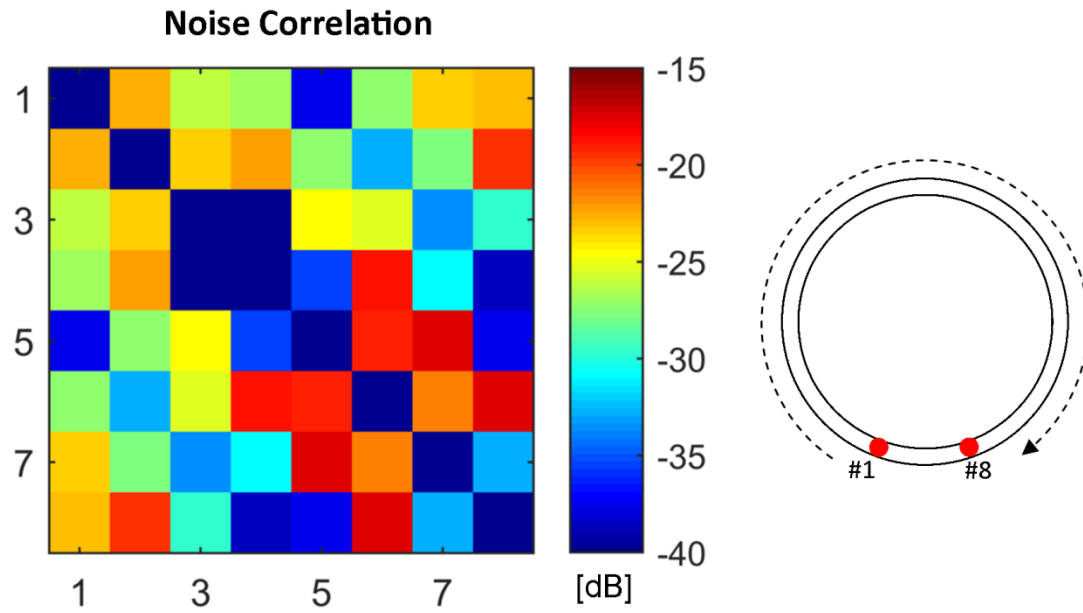


Figure 5.2 Noise correlation matrix of the RF coil. Each dot in the figure represents the correlation coefficient of the noise obtained on the two corresponding channels.

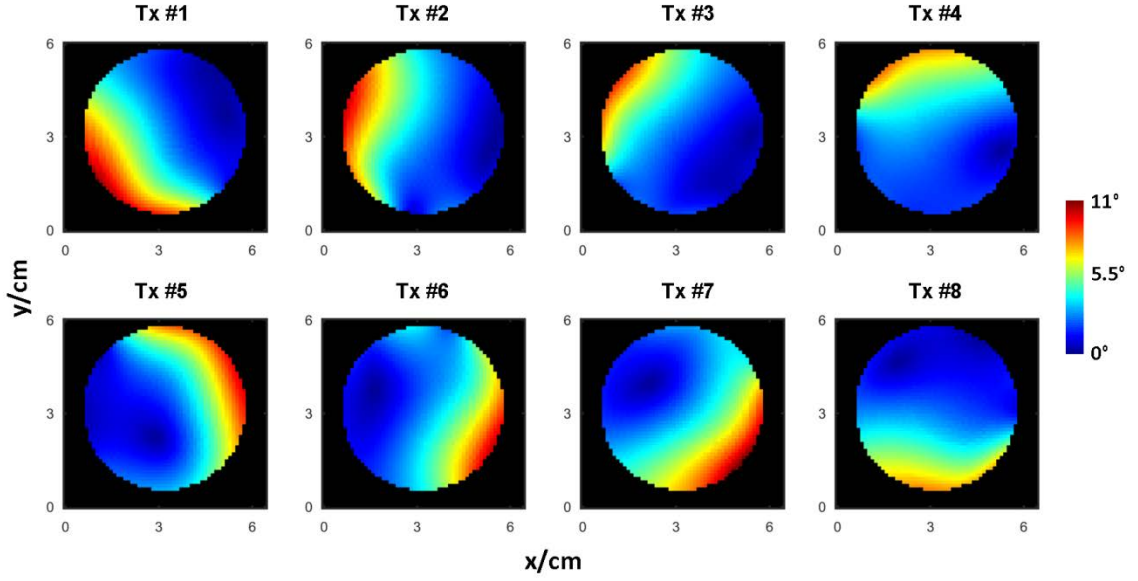


Figure 5.3 Measured transmit  $B_1$  field magnitude maps of all eight channels, showing distinctive patterns.

### 5.3.2 Phantom Validation

Figure 5.4 characterizes the employed imaging algorithm. Figure 5.4 (a) exhibits the so-called L-curve, which shows the  $L^2$ -error between the EP solution's gradient and the calculated gradient based on  $B_1$  measurement and the  $L^2$ -error between the absolute EP value and uniform initial input value  $\epsilon_{c(0)}$ , as a function of the regularization term  $\lambda$ . Here,  $\epsilon_{c(0)}$  was chosen as  $\sigma=1$  S/m and  $\epsilon=75 \epsilon_0$  based on the value of the two phantom components. As can be seen, the L-curve is well behaved, allowing straightforward determination of the optimized regularization term to minimize the induced errors of both gradient and absolute EP value. Here,  $\lambda$  of  $5^6$  was selected for the subsequent iterative EP reconstruction. In Figure 5.4 (b), the relative change of newly derived EP solution in the current iteration compared to the previous one is shown. It can be seen that the solution quickly approaches a stable state after three iterations with less than 0.5% relative change for both conductivity and permittivity.

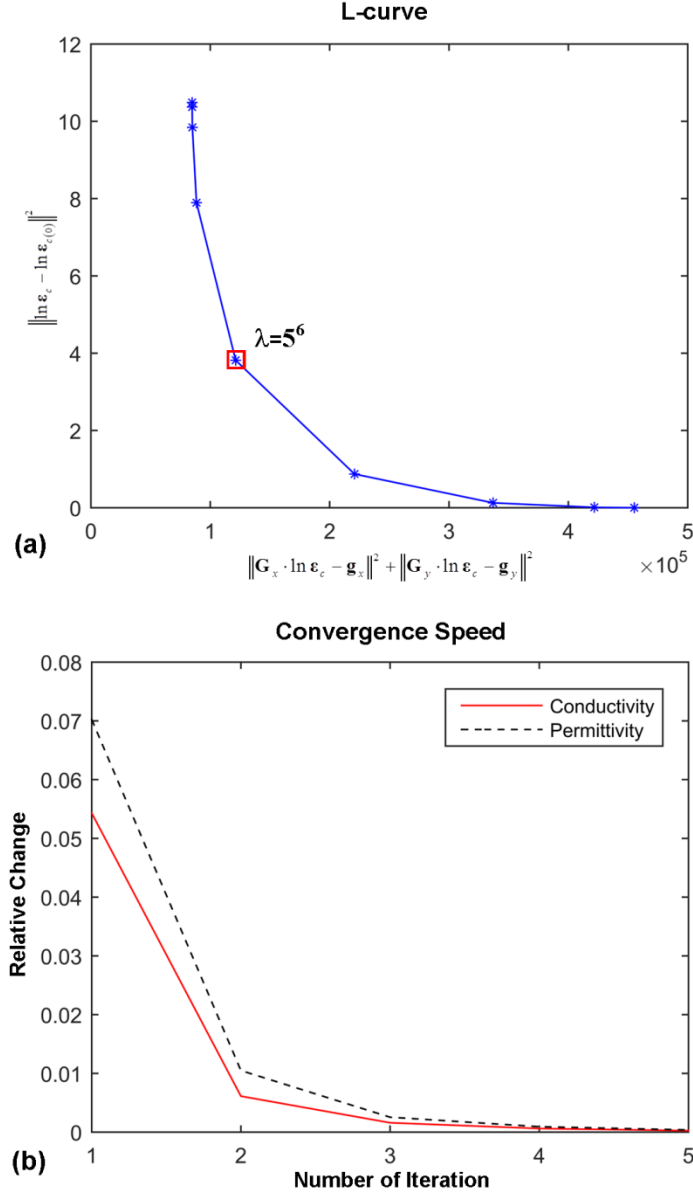


Figure 5.4 (a) L-curve of the proposed algorithm using initial EP value assignment. (b) Convergence speed over iterations.

The reconstructed EP maps are shown in Figure 5.5 in comparison with the target maps based on the probe-measured values. In general, the structure of the phantom is accurately indicated in the reconstructed EP maps in comparison with the magnitude image of the phantom. A sharp boundary can be clearly observed between the balloon

and the cylinder. This result suggests the feasibility and accuracy of realigning the derived EP gradient field of the sample from two acquisitions. Using initial  $\varepsilon_{c(0)}$  of  $\sigma=1$  S/m and  $\varepsilon=75 \varepsilon_0$ , the reconstructed mean EP value and standard deviation in the two compartments are  $\sigma=0.97\pm0.03$  S/m /  $\varepsilon=77.8\pm3.6 \varepsilon_0$  for compartment #1 (background) and  $\sigma=1.08\pm0.04$  S/m /  $\varepsilon=66.5\pm4.2 \varepsilon_0$  for compartment #2 (balloon), in comparison with the probe measured EP of  $\sigma=0.915$  S/m /  $\varepsilon=79 \varepsilon_0$  for compartment #1 (background) and  $\sigma=1.19$  S/m /  $\varepsilon=68.2 \varepsilon_0$  for compartment #2 (balloon).

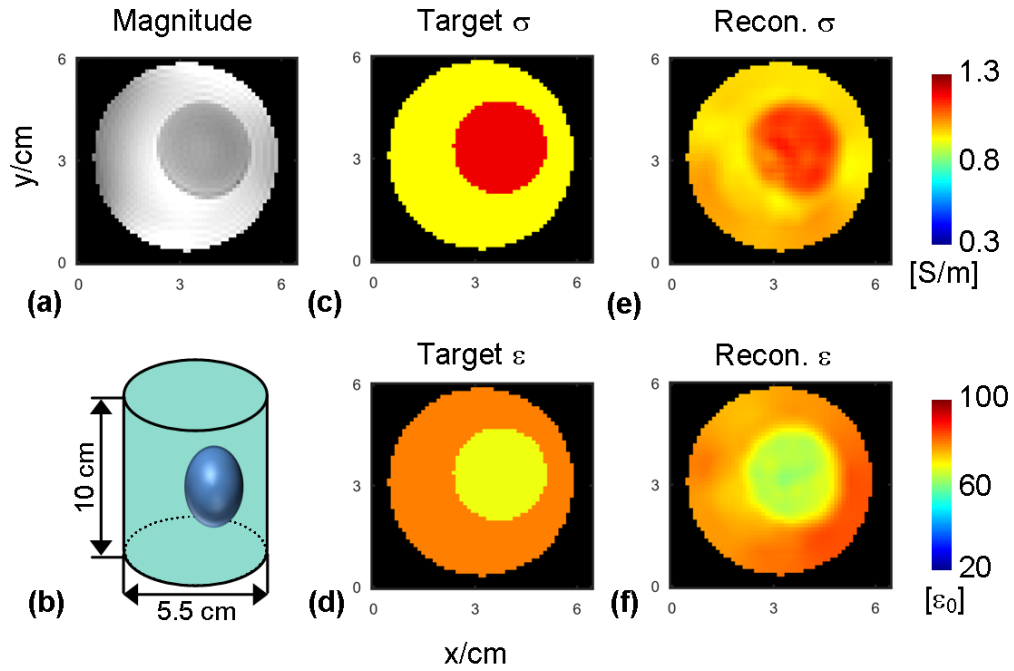


Figure 5.5 Reconstructed electrical properties of a phantom. (a) Magnitude of MRI image illustrating the structure of the phantom. (b) Schematic of the phantom structure and size. (c)-(d) Target electrical properties of the phantom based on probe measurement. (e)-(f) Reconstructed electrical properties distribution.

It is anticipated that the choice of initial  $\varepsilon_{c(0)}$  in the first iteration step will have an impact on the range of final absolute EP value. Figure 5.6 exhibits the impact of using various initial conductivity  $\sigma_{(0)}$  or permittivity  $\varepsilon_{(0)}$  on the reconstructed absolute EP in the

phantom. In Figure 5.6, it can be observed that even though the absolute value of the final reconstruction can be biased by the initial EP input, the differences between the phantom compartments are largely independent of  $\sigma_{(0)}$  or  $\varepsilon_{(0)}$  in a reasonable range. It also appears that the final conductivity and permittivity are minimally affected by the other's initial value. Therefore, it suggests that for practical applications, an approximate initial EP value can be assigned based on the averaged EP value in the ROI, and the final EP maps will preserve the EP difference of various compartments or tissues.

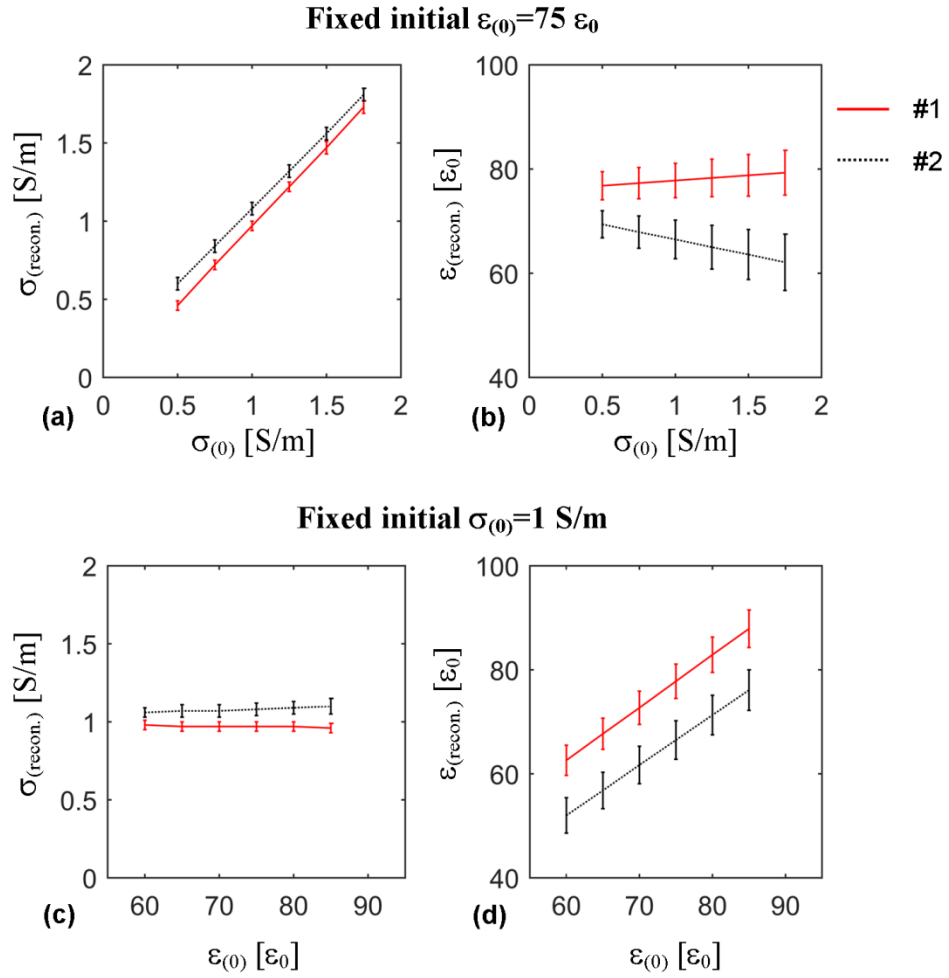


Figure 5.6 Effect of initial EP value on reconstruction result. (a) and (b): Reconstructed conductivity and permittivity using various  $\sigma_{(0)}$  and fixed  $\varepsilon_{(0)}$ , respectively. (c) and (d): Reconstructed conductivity and permittivity using various  $\varepsilon_{(0)}$  and fixed  $\sigma_{(0)}$ , respectively.



### 5.3.3 In Vivo Imaging Result

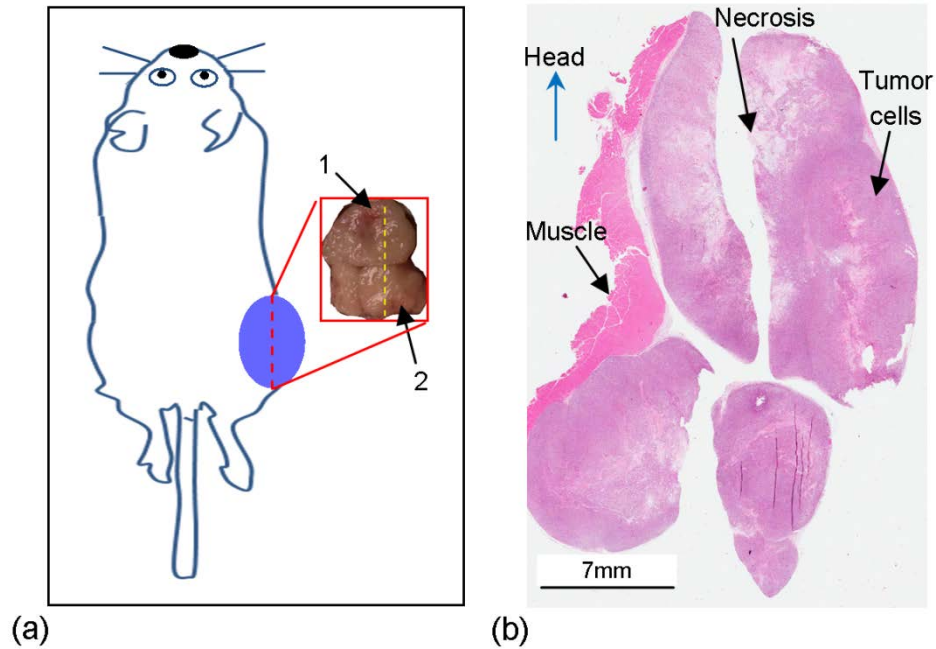


Figure 5.7 (a) Diagram of tumor location. Inlet: a cross-section view of the excised tumor in a slice that was cut following on the red dash line. On this slice, electrical properties were measured on nodules indicated by number 1 and 2 using a probe. (b) Histologic image in a slice following a cut indicated by the yellow dash line in the inlet in (a).

Figure 5.7 presents the histologic image of tumor and its relative location in the first animal. It can be observed that three different nodules had developed in the excised tumor, with the largest one close to the head. In Figure 5.7 (b), besides muscle, there are four separate pieces of tumor tissue, among which the two close to head correspond to nodule #1 in Figure 5.7 (a) and the other two nodule #2. The middle vertical gap in Figure 5.7 (b) resulted from a cut in the middle of the tumor to allow for dielectric measurement. Related to its size, in the histologic image, nodule #1 exhibits a larger fraction of necrosis characterized by a lighter stain in comparison to the darker viable tumor tissue and pink normal muscle tissue. The measured probe-EP value of muscle,

tumor #2 and #1 are  $\sigma_m=0.95$  S/m /  $\epsilon_m=62.0 \epsilon_0$ ,  $\sigma_{t2}=0.98$  S/m /  $\epsilon_{t2}=66.6 \epsilon_0$  and  $\sigma_{t1}=1.09$  S/m /  $\epsilon_{t1}=68.4 \epsilon_0$ , respectively, showing highest value in the most necrotic region of #1.

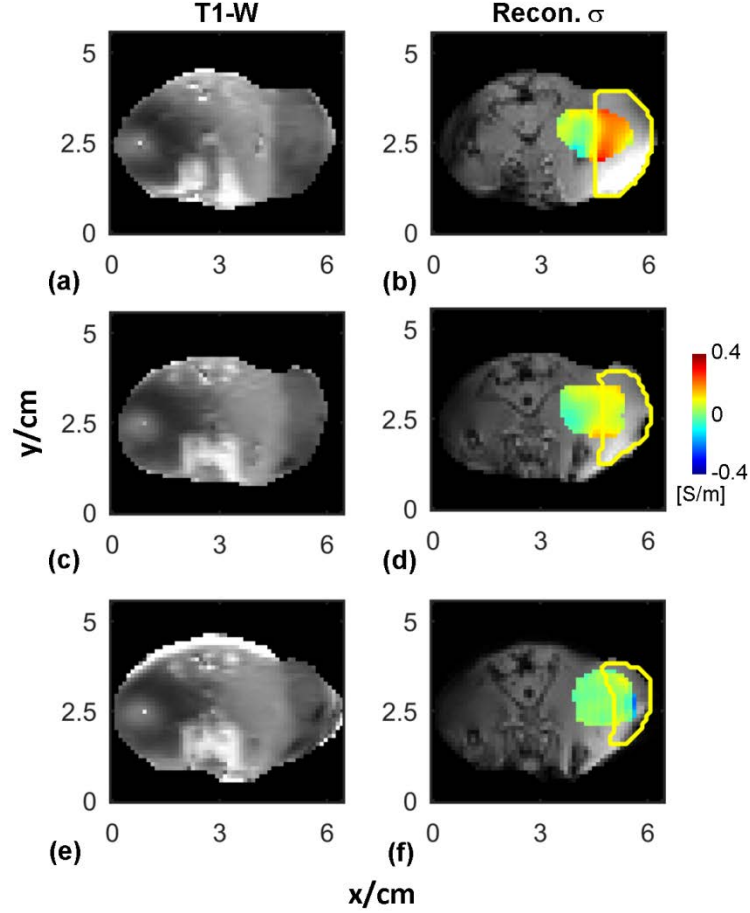


Figure 5.8 Reconstructed conductivity subtracted by the measured conductivity of muscle in comparison with T1-weighted anatomical images in three transverse slices from top (head) to bottom (tail). Yellow boundaries outline the dark region images on the right side in the corresponding T1-weighted.

Figure 5.8 presents reconstructed relative conductivity with reference to that of muscle in three slices in the first animal, with the top slice being closest to the head. In each slice, an ROI was selected for EP reconstruction, covering both tumor and normal tissue. The tumor regions on the right side of the animal are characterized by hypointensity in the T1-weighted MRI. The ring-like hypointensive regions on the left side are related to a weak coverage of the shimmed transmit  $B_1$  field, with a similar

pattern to the AFI map (data not shown here). In the top two slices in Figure 5.8, the reconstructed conductivity shows higher values in tumor than in muscle tissue. The boundary indicated by the conductivity value aligns with the one outlined based on the T1-weighted images. In the bottom slice, the reconstructed conductivity distribution is mostly uniform in both tumor and muscle. The reconstructed conductivity in tumor and muscle after being subtracted by the probe measured conductivity of muscle for the three slices from top to bottom are summarized as  $\sigma_{t1}=0.12\pm0.05$  S/m &  $\sigma_{m1}=-0.02\pm0.05$  S/m,  $\sigma_{t2}=0.08\pm0.02$  S/m &  $\sigma_{m2}=0.03\pm0.05$  S/m and  $\sigma_{t3}=0\pm0.07$  S/m &  $\sigma_{m3}=0\pm0.01$  S/m, respectively. An unpaired two-sample t-test shows statistically significantly different conductivity value between tumor and muscle regions in slices #1 and #2 except for slice #3. It can also be observed that the difference of reconstructed conductivity between tumor and muscle regions in slice #1 agrees well with the aforementioned probe measurement on tumor nodule #1 whereas the difference in slice #2 is close to the measurement on tumor #2 and almost diminishes in slice #3. Based on a combination of various information including conductivity, location and size, it can be inferred from the conductivity reconstruction that slice #1 is located in tumor nodule #1 while the other two are from nodule #2.

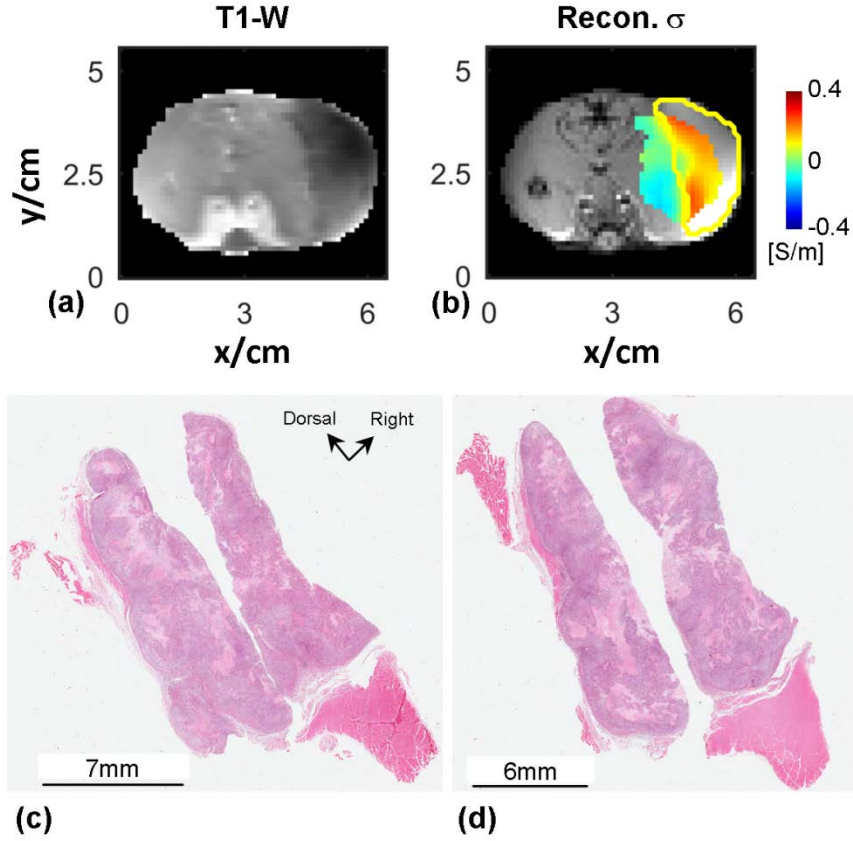


Figure 5.9 (a) T1-weighted anatomical image. (b) Reconstructed conductivity subtracted by the measured conductivity of muscle. Yellow boundary outlined the tumor region. (c) and (d) Histologic images of two transverse slices with orientation marked by arrows.

The reconstruction result of conductivity and histology result of another rat are shown in Figure 5.9. Unlike the first animal, only one tumor nodule was identified by visual inspection during the dielectric measurement. Separated away by at least 5 mm, two slices of histologic images in the transverse plane are shown in Figure 5.9 (c) and (d). Widely spread necrosis can be found in both histologic images. Different from the first animal, the measured EP of tumor is dominantly higher than that of muscle tissue, with EP of tumor being  $\sigma_t=1.08$  S/m &  $\epsilon_t=68.8 \epsilon_0$  and EP of muscle  $\sigma_m=0.9$  S/m &  $\epsilon_m=64.7 \epsilon_0$ . The reconstructed relative conductivity is shown in Figure 5.9 (b). The transition zone from muscle to tumor indicated by conductivity value is in consistent with the yellow

boundary derived from the T1-weighted image in Figure 5.9 (a). The reconstructed average conductivity in tumor region subtracted by the average conductivity in muscle region is 0.17 S/m, close to the measured difference of 0.18 S/m.

## 5.4 Discussion

In this study, a noninvasive in vivo system has been developed for imaging the electrical properties of small animals using MRI on 7 T. Utilizing the gradient-based EPT algorithm, the proposed method was built upon mapped multi-channel transmit  $B_1$  field using an eight-channel transmission line array coil. The system was validated using a physical phantom with known electrical properties. Small animals, Copenhagen rats with implanted subcutaneous tumors, were imaged, and the results showed elevated conductivity in tumor tissue in consistent with dielectric measurement. This is the first preclinical study for imaging tumor tissue's electrical properties using EPT.

The results of both phantom and in vivo experiments show high sensitivity to differentiate objects with small EP difference. In this study, the measured conductivity contrast between phantom compartments is 30% and around 20% between tumor and muscle in the animal models. The latter is consistent with previous studies which measured EP of tissue in the Larmor frequency range (Hancu et al., 2015; Joines, 1994). In comparison with the electrical properties in the audio frequency range, it is believed that electrical properties of a tissue in the high radiofrequency range are mainly determined by its net water and electrolyte content (Schwan, 1957). An EPT method with high sensitivity and specificity is desirable for characterizing tumor unless an intrinsically high EP contrast is present in the organ, e.g. breast carcinoma v.s. adipose tissue. The utilized method here shows less than 5% standard deviation of the actual absolute

conductivity within a uniform region in both phantom and in vivo studies. This demonstrates a strong power of differentiation for a 20% contrast. The reason for the benefit is believed to root from the intrinsic high robustness to noise and improved reconstruction performance near tissue boundaries using the gEPT algorithm. Second order derivative on the B1 field is a noise-amplifying operation based on Fourier analysis. The traditional Helmholtz-based EPT methods calculate voxel after another and treat each voxel independent from its neighbors. On the other hand, using the gradient-based EPT approach, the relative spatial relationship of voxels is used as constraints to solidify the reconstruction and improve the noise robustness. Recently, there are new EPT algorithms that reconstruct the electrical properties by solving a partial differential equation (Hafalir et al., 2014; Liu et al., 2015a; Wang et al., 2015). These approaches achieve similar enhancement against noise effect because the spatial relationship is utilized implicitly in the partial differential equation.

In the outcome of the in vivo study, both dielectric measurement and the in vivo imaging results in combination with histology suggest that necrosis in tumor is one of the driving forces for differentiated conductivity in tumor tissue at Larmor frequency. In the audio frequency range, electrical current mainly flows in the extracellular space because bilipid cell membrane serves as an insulating capsule for the intracellular space; shrunk cell volume and increased extracellular space in tumor lead to increased conductivity (D. C. Walker, 2000). In the higher radiofrequency range, the current barrier of cell membrane becomes more transparent electrically. Therefore, the relative volume of intracellular space and extracellular space contributes less to the conductivity change.

Necrosis can further induce vasogenic edema and elevation of Sodium inside tumor tissue (Babsky et al., 2005), leading to increased conductivity in necrotic tumor.

In current clinical practice, successful differentiation of therapeutic necrosis and tumor recurrence is a challenging but important topic. The two processes demonstrate similar syndrome and imaging outcome but are prescribed with distinctive treatment plans. Apparent diffusion coefficient was found to predict well the fraction of necrotic tissue in certain types of tumors but not in others (Lyng et al., 2000). T1 value has been shown to be shorter in necrotic regions than in the nearby viable tumor tissue, but the performance is not specific enough to accurately outline the necrotic region with reference to histology (Jakobsen et al., 1995). Although contrast-enhanced MRI improves the sensitivity and specificity (Lorenzo Mannelli, 2009; Osama et al., 2013), severe side effect may occur in some cases. The conductivity contrast as shown in this study could potentially be developed as a new mechanism to understand necrosis and viable tumor tissue by exploring their relative contribution to the increased conductivity.

In Chapter 4, it has been shown that the full gradient field of electrical properties can be obtained with enough channels of transmit and receive  $B_1$  fields. However, the proton density carried in MRI signal cannot be parsed out from the receive  $B_1$  field when measurement only includes magnitude and relative phase of transmit and receive  $B_1$  field. It should be noted that relative  $B_1$  phase can be mapped robustly because channel-independent phase component from non- $B_1$  sources will be cancelled out in deriving the relative phase. In this study, the proton density-bias issue was avoided by taking two sets of transmit  $B_1$  field measurements with the setup oriented in two opposite directions, one in the positive direction of the  $B_0$  field and one in the negative direction. Based on the

principle of reciprocity, this is equivalent to acquiring the receive B1 field of the positive direction when the setup is oriented negatively. The reconstructions of EP and its gradient in the two orientations are straightforward to be realigned as long as the rotation happens in a horizontal plane and a 180-degree rotation is guaranteed. This is a feasible approach for imaging small objects without spatial constraint and inconvenience as happens in human imaging situation.

To reconstruct the final absolute EP value, an initial constant EP was aligned to all the pixels in the reconstructed ROI. The initial value was chosen in a reasonable range considering the probe measured EP of tumor and muscle. For an arbitrary organ, this value can be determined from literature or measurement of specimen. As can be seen in Figure 5.6, the reconstructed difference of conductivity or permittivity is mostly independent of the initial value within a physiologically reasonable range. In many cases of medical diagnosis, the relative contrast difference is already useful for making a diagnostic decision. On the other hand, as suggested in previous chapters, a local pixelwise EP solution can be used to provide the global offset of absolute EP. However, it is challenging to be utilized in the current study to provide a stable offset due to the limited number of pixels in the small anatomy of rats.

In summary, an EPT platform suitable for imaging small animal tumor models has been developed. The reconstructed result of conductivity shows detectable increase inside tumor tissue. With high spatial resolution and sensitivity, the proposed method can be further applied to study the electrical properties of tumor in the early stage in an animal tumor model. It can provide important evidence for investigating the clinical value of EPT for tumor diagnosis.



## **Chapter 6**

# **Simultaneous Proton Density and Electrical Properties Imaging**

### **6.1 Introduction**

The generation of MRI (magnetic resonance imaging) signal involves a series of tissue properties. Among them, one class relates to the MRI-visible nuclear spins, such as proton density and relaxation times (e.g.  $T_1$ ,  $T_2$ , and  $T_2^*$ ), and another defines the distribution of the radiofrequency (RF) magnetic field inside the object, such as the electrical conductivity, permittivity and magnetic permeability. Using MRI, quantitative parametric mapping of various types of tissue properties can provide insight into the fundamental aspects of tissue for both research and medical purposes.

Recently, there has been an increasing interest toward quantitatively imaging, in vivo, the electrical properties (EP) of biological tissues, including conductivity ( $\sigma$ ) and permittivity ( $\epsilon$ ), using so-called electrical properties tomography (EPT) technique, based on the RF field (or  $B_1$  field) measured during an MRI scan (Haacke et al., 1991; Ulrich Katscher et al., 2009; Wen, 2003; Zhang et al., 2010). The electrical properties of tissue depend on multiple factors, such as water content, ion concentration, protein and fat composition, that can be significantly altered under pathological conditions. For example, substantial variations of EP at Larmor frequencies of water proton have been reported in various types of tumors, when compared with normal tissues (Balidemaj et al., 2015b; Joines, 1994; Yoo, 2004), suggesting that EPT may have the potential to be a noninvasive diagnostic tool in oncology.

Quantitative mapping of MRI-visible proton density ( $\rho$ ) is also a topic of great interest for several reasons. First of all, the coupling between  $\rho$  and receive  $B_1$  field need to be disentangled in order to implement EPT algorithms involving receive  $B_1$  field. Based on certain assumptions to reduce  $\rho$  bias on receive  $B_1$  field, utilizing both transmit ( $B_1^+$ ) and receive  $B_1$  ( $B_1^-$ ) fields, several EPT techniques (Liu et al., 2014, 2013; Sodickson et al., 2012; Zhang et al., 2013b) have been proposed to quantitatively calculate the unknown absolute  $B_1$  phase to overcome the limitation of half-transceiver-phase estimation at higher field strength (Voigt et al., 2011; Wen, 2003); more recently, a gradient-based EPT algorithm demonstrated high quality in vivo images of human brain with high spatial resolution and reduced sensitivity to noise (Liu et al., 2014). However, those EPT methods are sensitive to the experimental scenario where the utilized assumptions to remove  $\rho$  bias are not valid. Secondly, quantitative calculation of the specific absorption rate (SAR) requires  $B_1^-$  without  $\rho$  bias (Katscher et al., 2012; Zhang et al., 2013a). Calculation of SAR involves derivative on both  $B_1^+$  and  $B_1^-$ . Careful calibration of  $B_1^-$  magnitude and mapping of  $\rho$  are needed to assure SAR calculation accuracy. Thirdly, quantitative mapping of  $\rho$  can provide clinically relevant information in pathological conditions that are associated with changes in tissue water homeostasis, such as multiple sclerosis (Laule et al., 2004), brain ischemia (Ayata and Ropper, 2002), brain tumor (Neeb et al., 2006) or interferon treatment of liver metastases (Andersson et al., 1989).

In order to derive quantitative  $\rho$ -map, other contributing sources of MRI signal modulation have to be minimized or removed. These include the relaxation times ( $T_1$ ,  $T_2$  and  $T_2^*$ ),  $B_0$  field distortion, and inhomogeneity of  $B_1^+$  and  $B_1^-$ . Whereas  $B_0$  and  $|B_1^+|$  can

readily be measured, spatial variation of  $B_1^-$  is particularly challenging to be disassociated from  $\rho$ . One solution, using transceiver RF coils, is based on the reciprocity theorem (Hoult, 2000), assuming identical or symmetric profiles between  $B_1^+$  and  $B_1^-$  (Katscher et al., 2012; Liu et al., 2014; Zhang et al., 2013b), with the former being readily measured using various  $B_1$ -mapping techniques (Nehrke and Börnert, 2012; Sacolick et al., 2010; Yarnykh, 2007). However, as the field strength increases, this assumption generally does not hold because of the reduced wave length at higher frequencies. Meanwhile, the distribution of  $B_1$  field strongly correlates with the imaged objects so that it becomes increasingly inaccurate to predict the receive  $B_1$  profiles for a specific coil based on measurements obtained in a homogeneous phantom (Neeb et al., 2006). Another way for extracting  $\rho$  is based on the unified segmentation approach (Ashburner and Friston, 2005) to remove the residual inhomogeneity of  $B_1^-$  identified as the bias field map (Volz et al., 2012a; Weiskopf et al., 2011). Although this approach improves the reconstruction accuracy compared to the reciprocity-based method, it may fail in presence of abnormal morphologies such as brain tumors (Volz et al., 2012a, 2012b). The third strategy to quantify  $\rho$  exploits the observation of linear relationship between  $1/T_1$  and  $1/\rho$  (Volz et al., 2012b; Fatouros and Marmarou, 1999; Gelman et al., 2001). However, reconstruction errors again manifest themselves when brain diseases or injuries involving hemorrhagic, protein, fatty or calcification components are present with  $T_1$ -hyperintense images (Cakirer et al., 2003).

In this chapter, a novel method is proposed to quantitatively calculate the electrical properties ( $\sigma$  and  $\varepsilon$ ) and  $\rho$  at the same time. The measured  $B_1^+$  and  $\rho$ -weighted  $B_1^-$  ( $\rho B_1^-$ ) were taken as inputs into Maxwell's equations, which describe the RF wave

propagation in a sample carrying specific distribution of electromagnetic properties. Proton density was calculated as a scaling factor of  $B_1^-$ . The method was evaluated using simulated  $B_1$  field in a digital phantom and in a realistic human head model. Experiments were performed to validate the proposed approach in a phantom including pork tissue on a 7T MRI scanner.

## 6.2 Theory

Using MRI, the measured  $B_1$  components include the magnitude  $|B_1^+|$ ,  $\rho$ -weighted magnitude  $|\rho B_1^-|$ , and *image* phase  $\Theta$ . The image phase  $\Theta$  is a summation of *transceiver* phase  $\theta$  between a transmit and a receive channel and the background phase, which can be induced by  $B_0$  inhomogeneity, magnetic susceptibility, chemical shift, RF signal pathway delay, etc. Spatially variable background phase components can be imaged using  $B_0$ -mapping techniques with multiple echo times (TE) while the RF signal pathway delay only contributes a spatially constant zero-order phase, which is eliminated in the differential operation in EPT.

The *relative* phase between arbitrary transmit or receive channels can be calculated as the difference of  $\Theta$  related to corresponding transmit or receive channels. Taking transmit channel  $n$  as the reference channel, denoting its unknown *absolute* transmit  $B_1$  phase as  $\phi_n$ , the transmit and receive  $B_1$  fields can be written as

$$\begin{cases} B_{1j}^+ = B_{rj}^+ e^{i\phi_n} \\ B_{1k}^- = \gamma B_{sk}^- e^{-i\phi_n} \end{cases} \quad (6.1)$$

where  $B_{rj}^+ \equiv |B_{1j}^+| e^{i\phi_{rj}}$  includes the measured  $|B_1^+|$  and *relative* phase  $\phi_{rj}$  of transmit channel  $\#j$ ,  $B_{sk}^- \equiv |\rho B_{1k}^-| e^{i\theta_{sk}}$  is a complex field with a  $\rho$ -weighted magnitude  $|\rho B_{1k}^-|$  of

receive channel  $\#k$  and transceiver phase  $\theta_{nk}$ , and  $\gamma \equiv 1/\rho$  denotes a correcting factor to account for the unknown  $\rho$ .

Taking Eq. (6.1) into the central equations of EPT (2.15) and (2.16), they can be transformed into the forms of unknowns and measured components as

$$\begin{aligned} -\nabla^2 B_{rj}^+ &\approx \nabla B_{rj}^+ \cdot [2i\nabla\phi_n - (g_+, -ig_+, g_z)] \\ &+ B_{rj}^+ \cdot [\omega^2 \mu_0 \varepsilon_c + i\nabla^2 \phi_n - \nabla\phi_n \cdot \nabla\phi_n - i\nabla\phi_n \cdot (g_+, -ig_+, g_z)] \end{aligned} \quad (6.2)$$

and

$$\begin{aligned} -\nabla^2 B_{sk}^- &\approx \nabla B_{sk}^- \cdot [-2i\nabla\phi_n + 2\nabla\ln\gamma - (g_-, ig_-, g_z)] \\ &+ B_{sk}^- \cdot \{ \omega^2 \mu_0 \varepsilon_c - i\nabla^2 \phi_n - \nabla\phi_n \cdot \nabla\phi_n \\ &+ \nabla^2 \ln\gamma + \nabla\ln\gamma \cdot \nabla\ln\gamma - \nabla\ln\gamma \cdot (g_-, ig_-, g_z) \\ &- i\nabla\phi_n \cdot [2\nabla\ln\gamma - (g_-, ig_-, g_z)] \} \end{aligned} \quad (6.3)$$

where the unknowns are  $\nabla\phi_n$ ,  $\nabla\ln\gamma$ ,  $\mathbf{g}$ , and  $\varepsilon_c$ . As we can see in Eqs. (6.2) and (6.3), besides the first order components of the unknowns, there are second order polynomial or derivatives of the unknowns, and the complex permittivity  $\varepsilon_c$  is combined with the higher order terms. To derive a solution of  $\nabla\phi_n$ ,  $\nabla\ln\gamma$  and  $\mathbf{g}$ , we combined their high order polynomial and derivative and  $\varepsilon_c$  in Eqs. (6.2) and (6.3) and treated it as a new independent variable. With measured  $B_{rj}^+$  and  $B_{sk}^-$  of multiple RF channels,  $\nabla\phi_n$ ,  $\nabla\ln\gamma$  and  $\mathbf{g}$  can be derived by solving a set of linear equations. Final maps of  $\varepsilon_c$  and  $\rho$  can be calculated from the gradient  $\mathbf{g}$  and  $\nabla\ln\gamma$  using the finite difference method, with at least one seed point providing *a priori*  $\rho$  and absolute value of  $\varepsilon_c$  as introduced in Chapter 4 (Liu et al., 2014).

The reconstructed EP or  $\rho$  were evaluated using relative error (RE) and correlation coefficient (CC) as defined in Eq. (4.3) according to the corresponding ground true maps.

## **6.3 Materials and Methods**

### **6.3.1 Simulation**

Electromagnetic fields, including  $B_1$ , were simulated to evaluate the proposed method based on the finite-difference time-domain (FDTD) technique using SEMCAD X (Schmid & Partner Engineering, Zurich, Switzerland). In the simulation, a model of the 16-channel microstrip RF array coil (Adriany et al., 2008) used in the following experiment was loaded with either a digital phantom (Figure 6.1a) or the realistic Duke head model (Figure 6.1b) from Virtual Family (IT'IS Foundation, Zurich, Switzerland). The models were discretized into voxels of  $1.5 \times 1.5 \times 2 \text{ mm}^3$  in size. The z-axis is defined parallel to the head-foot direction. The tuning/matching/decoupling capacitors of the coil model were replaced with  $50\Omega$  port in the FDTD simulation, and the resultant S-parameters were transferred into Advanced Design System (ADS) (Agilent Technologies, Santa Clara, CA, USA) where the coil was tuned, matched and decoupled at 298 MHz by optimizing the S-parameters. The final  $B_1^+$  and  $B_1^-$  fields of the sixteen channels at 298 MHz were calculated based on the  $50\Omega$  port signal in the circuit simulation in ADS and the port signal and field maps in the 3D simulation in SEMCAD X (Kozlov and Turner, 2009; Lemdiasov et al., 2011). Values of  $\rho$  in cerebrospinal fluid (CSF), gray matter (GM) and white matter (WM) in the Duke head model were set to 1, 0.8 and 0.65, respectively [27], and 1 for other tissues.

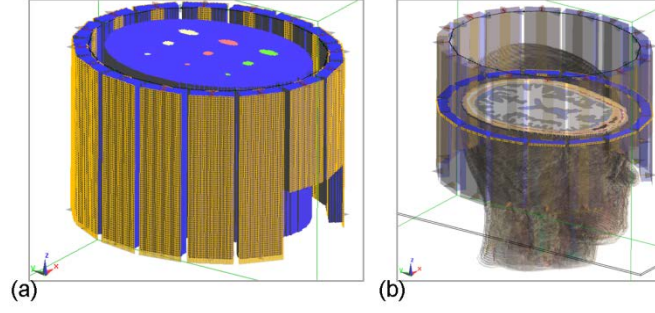


Figure 6.1 Simulation setup of a sixteen-channel microstrip RF coil loaded with a digital phantom (a) or the Duke head model (b) in which a cross-section of the brain is shown.

In the phantom simulation study, the effective spatial resolution and sensitivity for reconstructing EP and  $\rho$  were evaluated. An elliptic cylinder was used as the outer compartment with dimensions set approximately about the overall size of a human head, with a length of 16 cm, a major axis of 20 cm and a minor axis of 15 cm. The electrical properties of the cylinder were chosen as the average of human brain tissue at 298 MHz (S. Gabriel et al., 1996a), with  $\sigma=0.55$  S/m and  $\epsilon=52 \epsilon_0$ . Inside the cylinder, as shown in Figure 6.1, circular cylinders with diameters of 5 mm and 10 mm, and elliptic cylinders with a major axis of 20 mm and minor axis of 10 mm were included, organized on a  $3 \times 3$  Cartesian grid with their longitudinal axis parallel to the z axis and their lengths to be 16 cm. The three rows, carrying 3 different shapes each, were given the following pairs of (conductivity, relative permittivity): (0.61 S/m, 57), (0.83 S/m, 65) and (1.1 S/m, 72), and the corresponding  $\rho$  values were 1.1, 1.25 and 1.5, respectively, normalized to the value of  $\rho$  in the background (outer compartment).

The impact of noise was evaluated by adding independent and identically distributed random Gaussian noise, separately to the real and imaginary parts of the simulated complex  $B_1^+$  and  $\rho B_1^-$  fields. The standard deviation of the Gaussian noise was determined to be 2% of the magnitude of the corresponding  $B_1$  field, resulting in an

equivalent signal-to-noise (SNR) ratio of 50. When noise addition was applied, the data was smoothed, before further calculation, using a 3D Gaussian filter with a standard deviation of 1.2 voxels and a kernel size of 5 voxels in all three dimensions.

### 6.3.2 Experiment

#### *Phantom Preparation*

A phantom containing two compartments of different saline gel solutions and one inclusion of pork muscle tissue was built. The outer diameter of the phantom was 12 cm. The main body (compartment #1) of the phantom was filled with a gel solution including Agar, NaCl,  $\text{CuSO}_4 \cdot 5\text{H}_2\text{O}$  and deionized water with a mass ratio of 1.2:0.27:0.1:100. The electrical properties, measured with an Agilent 85070E dielectric probe and E5061B network analyzer (Agilent Technologies, Santa Clara, CA, USA) at 300MHz, were  $\sigma=0.639\pm0.003$  S/m and  $\varepsilon=79.1\pm0.1\varepsilon_0$ , where  $\varepsilon_0$  is the vacuum permittivity. A small balloon (compartment #2) positioned inside the main body was filled with a gel solution including Agar, NaCl,  $\text{CuSO}_4 \cdot 5\text{H}_2\text{O}$  and deionized water with a mass ratio of 1.2:0.45:0.1:100, and the measured electrical properties were  $\sigma=0.939\pm0.004$  S/m and  $\varepsilon=78.1\pm0.5\varepsilon_0$ . A block of fresh pork muscle (compartment #3), with measured electrical properties of  $\sigma=1.38\pm0.04$  S/m and  $\varepsilon=71.3\pm0.8\varepsilon_0$ , was also immersed in the gel. MR experiments began less than 30 minutes after building the phantom to minimize diffusion of ion from meat into gel, which may change the conductivity distribution.

#### *B<sub>1</sub>-mapping procedures*

The measured B<sub>1</sub>-related components included  $|B_1^+|$ ,  $|\rho B_1^-|$ , the image phase  $\Theta_k$  using transmit channel #*j* and receive channel #*k*, and the background  $\Delta B_0$  map. A sixteen-channel transceiver microstrip RF coil (Adriany et al., 2008) was used in the



experiment. First of all, a  $B_1$ -shimming configuration was applied in the CP2+ mode (Orzada et al., 2013), providing strong  $|B_1^+|$  around the periphery of the phantom, and the resultant flip angle (FA) map was imaged using the Actual Flip-angle (AFI) technique (maximum FA $\approx$ 90°) (Yarnykh, 2007). With one channel transmitting at a time, a series of small-flip-angle (FA $<$ 10°) GRE (gradient-recalled echo, 10 averages) sequence was employed to calculate the magnitude  $|B_1^+|$  after the GRE images were normalized by the sine of the measured AFI map (Van de Moortele et al., 2007). The image phase  $\Theta_{jk}$  was acquired from another scan, in the same single-channel-transmit mode, with a larger flip angle (maximum FA $\approx$ 30°, 3 averages). In the same  $B_1$ -shimming mode as the AFI scan, the  $\rho$ -weighted magnitude  $|\rho B_1^-|$  was acquired using a GRE scan (maximum FA $\approx$ 90°, TE=3.1 ms and TR=8 s, 2 averages) and removing the sine of FA from the measured images. The  $\Delta B_0$  map was calculated by taking the phase difference of a GRE scan at two TEs which were separated by 5.08 ms. All imaging sequences employed a voxel size of  $1.5 \times 1.5 \times 3 \text{ mm}^3$ , and 12 contiguous slices (thickness = 3 mm) were acquired in total.

### ***Data Processing***

The *relative* transmit  $B_1$  phase  $\phi_{mj}$  between channel #j and a reference channel #n was derived from all receive channels, calculated as  $\phi_{mj} = \arg \left\{ \sum_k w_k \exp \left[ i \left( \Theta_{jk} - \Theta_{nk} \right) \right] \right\}$  where  $w_k$  is a weighting factor proportional the squared magnitude of receive channel #k for maximum SNR of mean relative phase. The transceiver phase  $\theta_{nk}$  was derived from the image phase  $\Theta_{nk}$  after  $\Delta B_0$ -induced phase  $\phi_{\Delta B_0} = \gamma_g \cdot \Delta B_0 \cdot \text{TE}$  (with  $\gamma_g$  the gyromagnetic ratio and TE the echo time) was removed. The resultant complex *relative* transmit  $B_1$

field  $B_{ij}^+$  and  $\rho$ -weight receive  $B_1$  field  $B_{sk}^-$  were smoothed using a Gaussian filter with a standard deviation of 1.2 voxels and kernel of 5 voxels in all three directions.

## 6.4 Results

### 6.4.1 Simulation

Results of reconstructed EP and  $\rho$  of the phantom model are compared with the corresponding target maps as shown in Figure 6.2. The target distributions of EP are calculated based on Ampere's Law from simulated electromagnetic field data instead of taken as the input value to the simulation model because the proposed theory is derived from Maxwell's equations. A seed point at the center of the phantom was utilized. As can be seen, under the noise-free condition in Figure 6.2(b), (g) and (l), both EP and  $\rho$  were accurately reconstructed in comparison with the target distribution. The REs and CCs of the reconstructed maps under the noise-free condition were  $RE_\sigma=0.9\%$  /  $CC_\sigma=99.7\%$ ,  $RE_\epsilon=0.7\%$  /  $CC_\epsilon=99.0\%$  and  $RE_\rho=2.1\%$  /  $CC_\rho=94.3\%$ . The line profiles extracted from the reconstructed results, shown in Figure 6.2(d), (i) and (n), reveal a high consistency between reconstruction and ground true values, and indicate that objects with a diameter as small as 5 mm and contrast ratio as low as 10% relative to the surrounding region could still be clearly detected.

The results of reconstructed EP and  $\rho$ , when noise (SNR=50) was included, are shown in Figure 6.2 (c), (e), (h), (j), (m) and (o). It can be seen that, overall, there is a good agreement between reconstructed maps and target distribution, and shaped compartments that are larger than 5mm or with a contrast higher than 10% are clearly identified, even though fluctuation resulting from the noise addition is observed,

especially between the inserted compartments. We notice that the peak values of reconstructed EP and  $\rho$  inside the cylindrical objects under the noise condition are mostly lower than the target peak values. This phenomenon is partially due to the effect of applied Gaussian filter and can be confirmed in reconstructed EP and  $\rho$  using filtered noise-free field data (results not shown). The REs and CCs for the reconstruction with added noise are  $RE_{\sigma}=4.5\%$  /  $CC_{\sigma}=93.6\%$  and  $RE_{\varepsilon}=2.6\%$  /  $CC_{\varepsilon}=88.4\%$ , and  $RE_{\rho}=3.9\%$  /  $CC_{\rho}=81.5\%$ , respectively. It can also be seen in Figure 6.2 (c), (h) and (m), that the shaped compartments with only 10% contrast and 5-mm in diameter become difficult to be distinguished from the background due to the combined effect of added noise and applied Gaussian filter. Similar observations can be made for the corresponding line profiles as a function of compartment size and contrast in Figure 6.2(e), (j) and (o).

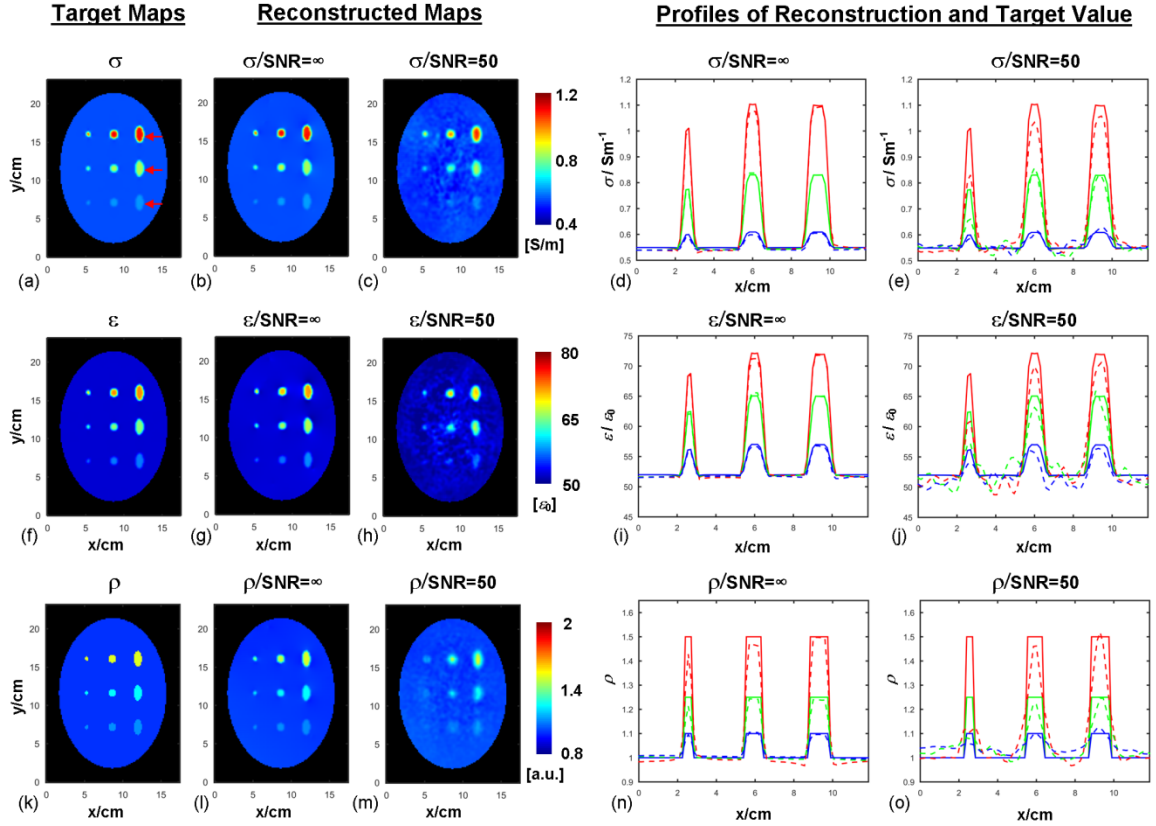


Figure 6.2 From left to right: (a), (f) and (k): Target maps of conductivity ( $\sigma$ ), permittivity ( $\epsilon$ ) and proton density ( $\rho$ ). Red arrows in (a) indicate the positions of the line profiles shown in the reconstruction plots. (b), (g) and (l): Reconstructed  $\sigma$ ,  $\epsilon$  and  $\rho$  distribution in the absence of noise, respectively. (c), (h) and (m): Reconstructed  $\sigma$ ,  $\epsilon$  and  $\rho$  distribution when random noise was added into simulated  $B_1$  field, respectively. (d), (i) and (n): Line profiles of reconstructed  $\sigma$ ,  $\epsilon$  and  $\rho$  in the absence of noise, respectively. (e), (j) and (o): Line profiles of reconstructed  $\sigma$ ,  $\epsilon$  and  $\rho$  in the noise condition, respectively. Red, green and blue lines represent the top, middle and bottom arrows shown in (a), respectively, with solid lines for target value and dashed lines for reconstructed results.

Using the realistic Duke head model, the reconstructed maps of EP and  $\rho$  are shown in Figure 6.3. The REs and CCs for the reconstructed EP and  $\rho$  in different brain regions are presented in Table 6.1. It can be observed that under the noise-free condition, the reconstructed EP and  $\rho$  values were highly consistent with the target distribution. When noise was added, the reconstructed maps were still fairly consistent with the target

maps, however they appear blurred due to the applied Gaussian filter, which is needed to mitigate the magnification of noise by Laplatian operator.

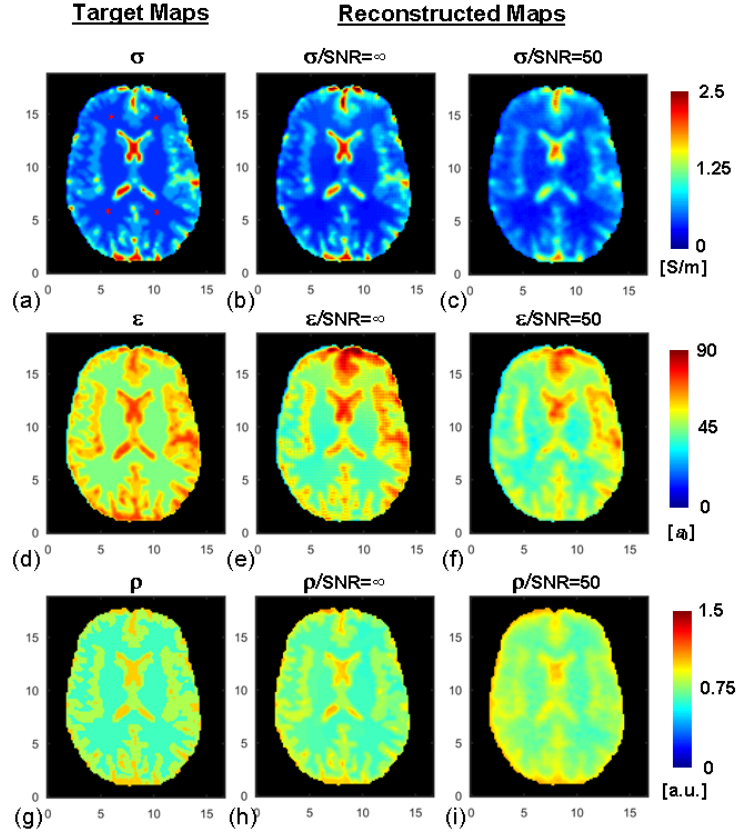


Figure 6.3 Duke head model and reconstruction results. From left to right: target distribution of conductivity (a), permittivity (d) and proton density (g) of the model; reconstructed conductivity (b), permittivity (e) and proton density (h) in the absence of noise; reconstructed conductivity (c), permittivity (f) and proton density (i) when noise was added. Red “\*” in (a) represent the location of four seed points. The axis unit is cm.

Table 6.1 Evaluation of reconstructed EP and proton density using duke head model.

REs		SNR= $\infty$	SNR=50
GM	$\sigma$	14.8%	20.1%
	$\varepsilon$	11.0%	14.5%
	$\rho$	5.4%	9.1%
WM	$\sigma$	14.5%	15.1%
	$\varepsilon$	10.6%	11.1%
	$\rho$	5.2%	15.2%
CSF	$\sigma$	14.7%	28.8%
	$\varepsilon$	14.3%	17.9%
	$\rho$	6.8%	10.0%
Total (REs/CCs)	$\sigma$	14.7%/0.96	23.0%/0.91
	$\varepsilon$	11.4%/0.95	13.9%/0.93
	$\rho$	5.5%/0.95	9.9%/0.88

## 6.4.2 Experiment

Figure 6.4 (b)-(f) show the experimental phantom with several measured parametric maps. In the CP2+ B<sub>1</sub>-shimming mode, the transmit B<sub>1</sub> field (Figure 6.4b) is boosted around the circumference of the phantom (constructive interferences) whereas destructive interferences result in a region devoid of transmit B<sub>1</sub> field at the center of the phantom, which was excluded in the reconstruction algorithm. Over a fraction of its circular path, the boundary between the inserted balloon and the surrounding gel phantom can easily be followed as shown by the red arrow in the B<sub>0</sub> map (Figure 6.4c). Figure 6.4(f) clearly demonstrates the impact of proton density in the  $\rho$ -weighted magnitude of receive B<sub>1</sub>, with sharp discontinuity in the corresponding map at the boundary between pork and gel.

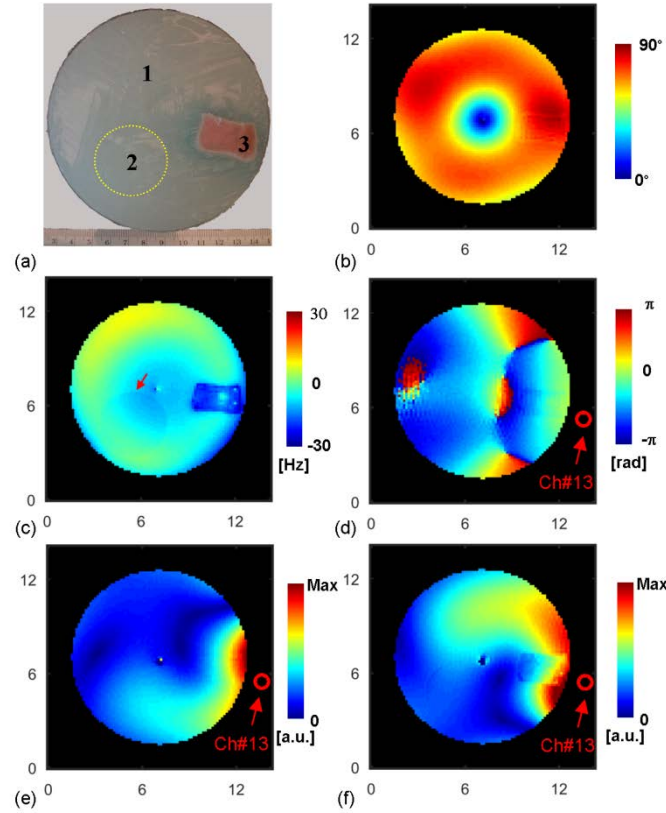


Figure 6.4 Experimental condition. (a): Photograph of a cross section of the phantom showing pork muscle and a small spherical compartment of gel as indicated by the yellow dash circle. (b): Measured flip angle distribution in CP2+  $B_1$  shimming configuration. (c): Measured  $\Delta B_0$  field map in Hz. Red arrow indicates the boundary of the small gel compartment. (d): Measured image phase distribution using channel #13 for both transmission and reception. (e): Measured magnitude of transmit  $B_1$  field of channel #13. (f): Measured proton density-weighted magnitude of receive  $B_1$  field of channel #13. The axis unit is cm.

The reconstructed EP maps are shown in Figure 6.5 in comparison with the target maps based on the probe-measured values. Note that in the reconstructed maps in Figure 6.5(b), (c), (e) and (f), the black circle in the center represents the region devoid of  $B_1^+$  field that was excluded from the reconstruction. The reconstruction results of EP using either one or two seed points in compartment #1 are shown in Figure 6.5 (b) and (e), and Figure 6.5(c) and (f), respectively. The results are consistent to each other regarding the selection of seed points. The reconstructed EP values using different seed points,

summarized in Table 6.2, are in good agreement with the probe measurement. The three phantom compartments are clearly identified in the reconstructed maps, with a sharp delineation of the boundary between the balloon and the cylinder. On the other hand, the boundary between pork and gel in the conductivity map is blurred, possibly because of diffusion of conducting ions into the gel in which the pork is exposed. The latter explanation is consistent with the sharper edge preserved in the permittivity map, since permittivity is less sensitive to the ion diffusion process.

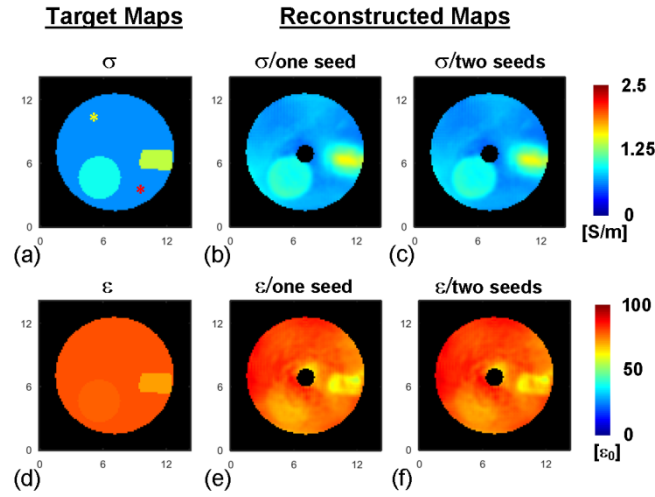


Figure 6.5 Left: drawings of the three phantom compartments with conductivity (a) and permittivity (d) values as measured with a probe. Yellow and red asterisks in (a) indicate the seed points. Middle: reconstructed conductivity (b) and permittivity (e) maps using one seed point located at the yellow asterisk in (a). Right: reconstructed conductivity (c) and permittivity (f) maps using two seed points in (a). The axis unit is cm.



Table 6.2 Reconstructed EP in the phantom. Units of  $\sigma$  and  $\varepsilon$  are S/m<sup>-1</sup> and  $\varepsilon_0$ , respectively.

EP <sup>a</sup>		Reconstruction (one seed)	Reconstruction (two seeds)	Probe measurement
#1	$\sigma$	0.77±0.17	0.74±0.17	0.64
	$\varepsilon$	77.2±5.4	78.3±5.3	79.1
#2	$\sigma$	0.98±0.04	0.95±0.04	0.94
	$\varepsilon$	74.2±4.5	75.6±4.5	78.1
#3	$\sigma$	1.28±0.16	1.26±0.16	1.38
	$\varepsilon$	64.7±3.5	66.6±3.5	71.3

The reconstructed  $\rho$  in the phantom using the proposed method is shown in Figure 6.6(a), with calculated values that are comparable for the gel compartments #1 ( $0.98 \pm 0.08$ ) and #2 ( $1.07 \pm 0.04$ ), which is expected since only the NaCl concentration was slightly changed between the two gels. The value of reconstructed  $\rho$  is  $0.85 \pm 0.05$  within the pork. We were not able to independently measure the actual  $\rho$  distribution in the pork tissue for assessing the accuracy of the reconstructed  $\rho$  results. However, an indirect evaluation consists in applying the calculated  $\rho$  value to EPT reconstruction methods, that implicitly rely on unbiased  $B_1^-$  maps, and evaluating the corresponding calculated EP. In the present case we followed this approach using the gradient-based EPT (gEPT) algorithm (Liu et al., 2014). We also compared two additional methods for estimating  $\rho$  that are based on some  $B_1$ -pattern assumptions: one assumes an approximate *mirroring symmetry* between the sum of transmit  $B_1$  magnitude and that of receive  $B_1$  magnitude through all channels in a transceiver coil symmetrical about the y-axis:  $\sum_i |B_{1,i}^+(x, y)| \approx \sum_i |B_{1,i}^-(-x, y)|$  (Liu et al., 2014; Zhang et al., 2013b), while the other assumes an approximate *identity* between the two sums  $\sum_i |B_{1,i}^+(x, y)| \approx \sum_i |B_{1,i}^-(x, y)|$  under the same coil geometry assumptions (Katscher et al., 2012; Van de Moortele and Ugurbil,

2009). As can be seen in Figure 6.6(b) and (c), the estimated  $\rho$  distributions based on  $B_1$ -pattern assumptions result in larger spatial deviations of  $\rho$  inside each phantom compartment ( $\rho$  should be homogeneous in compartment #1 as well as in compartment #2). Similarly, the reconstructed EP maps as shown in Figure 6.6 (e) and (h) and Figure 6.6 (f) and (i), which were obtained using the gEPT algorithm and estimated  $\rho$  from  $B_1$ -pattern assumptions, clearly depict larger EP erroneous deviations than the reconstructed EP maps using gEPT and calculated  $\rho$  with the proposed method in Figure 6.6(d) and (g). This is especially noticeable in the permittivity maps. These findings are supported by the quantitative evaluation of the reconstructed EP using REs and CCs as shown in Table 6.3. The larger impact of  $\rho$  on permittivity results is consistent with the theoretical analysis that indicates that permittivity is more closely related than the conductivity to the magnitude of  $B_1$  field (Voigt et al., 2011).

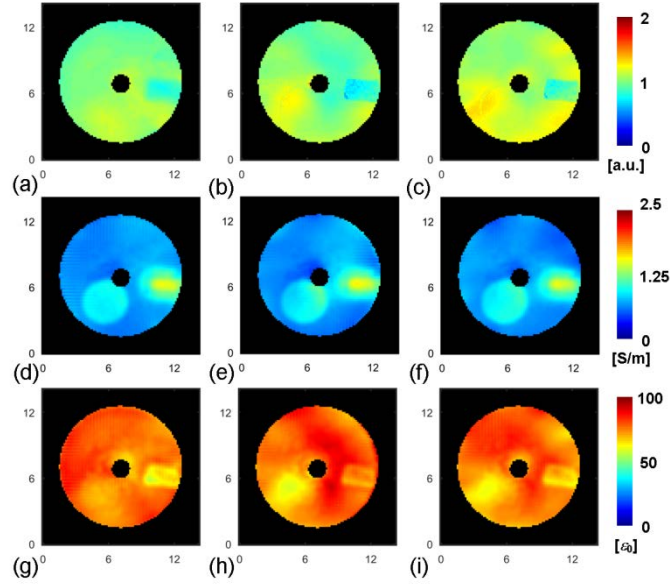


Figure 6.6 Reconstructed proton density and its effect on the accuracy of EP reconstruction using the gradient-based EPT (gEPT) algorithm. Top: reconstructed proton density using the proposed method (a), assuming symmetric  $B_1$  pattern (b) or assuming identical  $B_1$  pattern (c). Middle: reconstructed conductivity (d)-(f) using gEPT algorithm and estimated proton density corresponding to (a)-(c), respectively. Bottom: reconstructed permittivity (g)-(i) using gEPT algorithm and estimated proton density corresponding to (a)-(c), respectively. The axis unit is cm.

Table 6.3 Evaluation of reconstructed EP using gradient-based EPT and differently derived proton density.

		Calculated $\rho$	S.B.- $\rho$	I.B.- $\rho$
RE	$\sigma$	15%	18%	15%
	$\varepsilon$	6%	9%	8%
CC	$\sigma$	0.82	0.77	0.82
	$\varepsilon$	0.6	0.17	0.35

S.B.- $\rho$ : Estimated  $\rho$  assuming symmetric  $B_1$  pattern  
I.B.- $\rho$ : Estimated  $\rho$  assuming identical  $B_1$  pattern

## 6.5 Discussion

In this study, for the first time, quantitative  $\rho$  distribution was rigorously calculated based on measurable  $B_1$  information in MRI, along with the electrical properties. Different from other approaches exploiting various assumptions such as the  $B_1$  reciprocity (Zhang et al., 2013b; Katscher et al., 2012) or the  $1/\rho$ - $1/T_1$  relationship

(Fatouros and Marmarou, 1999; Volz et al., 2012b), the proposed method calculates  $\rho$  by solving the Maxwell's equations involving transmit and receive  $B_1$  field, exploiting the multiple channels available in a transceiver array. The method was first evaluated using simulated  $B_1$  field, and the results showed strong similarity between, on the one hand, the reconstructed  $\rho$  and electrical properties and, on the other hand, their target values. The method was further validated using a physical multi-compartment phantom on a 7T MRI scanner. The experimental results demonstrated accurate EP reconstruction, based on  $B_1$  measurements, when compared with direct dielectric probe measurement. Significant improvement in  $\rho$  estimation was found with the proposed method compared with  $B_1$  pattern-based approaches.

Compared to a previously proposed gradient-based EPT (gEPT) technique (Liu et al., 2014), which has been shown to provide improved robustness against noise and increased performance near tissue boundaries, the major advantage of the proposed method is that it aims at rigorously calculating  $\rho$  from the measured  $B_1$  information. It expands the generality of the gEPT method, and it is independent of particular geometric assumptions about the object or the coil that typically tempt to fail at higher field. At the same time, quantitative  $\rho$  map is estimated and can be useful for understanding lesions causing tissue's water content change. The resultant unbiased magnitude of receive  $B_1$  field is also desirable for accurate estimation of SAR (Katscher et al., 2012; Zhang et al., 2013a), which is an important safety concern at high field. As can be seen in (4) and (5), in order to calculate  $\rho$ , the transceiver phase for each pair of transmit and receive channels is utilized together with the magnitude  $|B_1^+|$  and  $|\rho B_1^-|$  as input. As a common approach in EPT studies (Hafalir et al., 2014; Katscher et al., 2012; Sodickson et al.,

2012; Voigt et al., 2011), utilizing the transceiver phase requires removal of background phase resulting from inhomogeneous  $B_0$  field distribution, susceptibility-induced  $B_0$  distortion, chemical shift and eddy current induced phase accumulation. On the other hand, EPT methods, such as gEPT, using only relative  $B_1$  phase between individual channels (Liu et al., 2014, 2013; Zhang et al., 2013b), are insensitive to possible residual background phase. As suggested by our results in Figure 6.6, an optimized strategy could consist of applying the calculated  $\rho$  distribution to the gEPT algorithm, thereby taking advantage of the robustness of the relative phase measurement offered by the latter.

The sensitivity and spatial resolution for detecting contrast in both EP and  $\rho$  were evaluated in the simulation study as shown in Figure 6.2. It can be seen that down to the relative contrast ratio of 10%, the proposed method is able to detect small regions (<5 mm) of different EP, at a much smaller spatial scale than that of the wavelength ( $\approx 14$  cm) of the probing RF field. We attributed these performances to the high spatial resolution obtained in MRI acquisitions and to the enhanced near-boundary performance and noise robustness of the proposed algorithm in which spatial gradient of EP is integrated to derive the final EP maps. Due to the noise-reduction spatial filter, the effective resolution of the reconstructed EP and  $\rho$  maps is less than that of actual MRI images, with an evident smoother appearance for the results obtained with experimental data as well as for those obtained in simulation studies when noise addition is performed. This points towards the need for exploring, in future studies, fast and unbiased  $B_1$  mapping techniques to achieve high SNR in the measured  $B_1$  data in order to reduce or alleviate the use of spatial filters.

In this study, the EP and  $\rho$  values of the seed points were assumed to be known in order to calculate the final maps using the corresponding gradient. A frequent approach in semi-quantitative MRI or spectroscopy consists in normalizing metabolites or  $\rho$  in various tissues by comparison to the value of a reference tissue such as ventricular CSF for intra-cerebral studies. Similarly, in the current study an arbitrary value of  $\rho$  can be assigned to a seed point. However, there is a growing interest in the absolute values of EP, and it may be impractical under some in vivo conditions to find seed points where absolute EP values are assumed to be known. Incorrect assignment of these seed point values can shift the global reconstructed maps. As can be seen in Eqs. (6.2) and (6.3), although the local absolute EP value in  $\varepsilon_c$  can be calculated pixel-by-pixel once gradient of absolute phase, EP and  $\rho$  are determined, this local pixel-wise EP solution is subjective to error propagation during reconstruction. Recently, we have proposed an algorithm to sample useful absolute EP value in the reconstructed local EP solution (Liu et al., 2015b). The method utilized the local EP solution to provide absolute EP value reference, and at the same time, improved EP reconstruction performance using gradient  $g_+$  from measured  $B_1^+$  as a global constraint. It is straightforward and expected to be more accurate to incorporate the full gradient vector  $\mathbf{g}$  as provided in the proposed method here.

As we can see in Eqs. (6.2) and (6.3), assuming negligible  $B_z$ , the object for solving the equations is essentially deriving a system of nonlinear partial differential equations (PDE) involving the unknown absolute  $B_1$  phase, EP and  $\rho$ . In previous studies, various assumptions have been exploited to gauge the absolute  $B_1$  phase (Voigt et al., 2011; Wen, 2003) or  $\rho$  distribution (Liu et al., 2014; Zhang et al., 2013b). Assuming known absolute  $B_1$  phase, Hafalir *et al.* developed a linear PDE-based EPT approach (cr-

MREPT) (Hafalir et al., 2014), and explicitly utilized the spatial relationship between the EP of different voxels, which is carried in the derivatives, to improve the results near boundaries and the robustness to overcome disruption induced by measurement noise. However, reconstruction error increased when cr-MREPT was evaluated using the estimated phase based on the half-transceiver-phase assumption. In this study, the final EP and  $\rho$  maps were derived in two steps: 1) the gradient of EP,  $\rho$  and  $B_1$  phase were calculated using multiple channels of  $B_1$  data and 2) spatial integration was carried out on the gradients to obtain the final maps. Unique solution was obtained when multiple channels of  $B_1$  data were available. Future work will explore algorithms to solve the distribution of phase, EP and  $\rho$  in the nonlinear PDEs as shown in Eqs. (6.2) and (6.3) in one step. They are expected to give more robust reconstruction results by taking advantage of the spatial relationship between voxels and avoiding error propagation across steps.

In summary, in this study, for the first time, a new method was developed to quantitatively map proton density distribution, together with electrical properties distribution, using the  $B_1$  field information measured with an MRI scanner. The method was evaluated and validated both theoretically in simulation studies and experimentally in a physical phantom on a 7T scanner. The results demonstrated high spatial resolution and high sensitivity to contrast in reconstructed EP and  $\rho$ . The method improves the generality of EPT algorithms utilizing both transmit and receive  $B_1$  fields, devoid of specific assumptions to obtain  $\rho$  distribution which is coupled with receive  $B_1$  field in MRI measurement. Accuracy of reconstructed  $\rho$  maps was improved compared to previous estimation based on  $B_1$ -pattern assumptions. This method is expected to help

improve EP-based noninvasive in vivo tissue characterization and provide a new way for estimating quantitative  $\rho$  map for diagnostic and research purpose.



## Chapter 7 Summary and Future Work

### 7.1 Summary

The electrical conductivity and permittivity are intrinsic properties of tissue and are associated with fundamental biophysics down to molecular and cellular levels. Measuring electrical properties in vivo and understanding the underlying mechanism have significant value in understanding the response of tissue to electromagnetic stimulation and clinical applications of disease diagnosis and therapy. The history of studying tissue's electrical properties started more than 100 years ago, with theoretical framework established by 1980s (Foster and Schwan, 1989).

As introduced in Section 2.2.2, over the past decades, a large amount of efforts have been dedicated to noninvasively image the electrical properties in vivo. Among these methods, electrical properties tomography (EPT) is a recently introduced imaging modality. It reconstructs distribution of the electrical properties based on the measured  $B_1$  field map using magnetic resonance imaging (MRI) (Wen, 2003; U Katscher et al., 2009; Zhang et al., 2010). During an MRI scan,  $B_1$  field is commonly used to induce nuclear spin precession inside tissue for the purpose of MRI imaging (Lauterbur, 1973) and can be quantitatively measured using various  $B_1$ -mapping techniques (Yarnykh, 2007; Van de Moortele and Ugurbil, 2009; Sacolick et al., 2010). Compared to other noninvasive electrical-property imaging techniques aiming at high spatial resolution, such as magnetic resonance electrical impedance tomography (MREIT) (Zhang, 1992) and magnetoacoustic tomography with magnetic induction (MAT-MI) (Hu et al., 2011; Li and He, 2010; Mariappan and He, 2013; Xu and He, 2005), EPT takes advantage of well-

established instrumentation of MRI for the measurement. Using MRI, high spatial resolution maps of  $B_1$  field can be obtained, and electrical properties can be computed from the measured  $B_1$  maps with high spatial resolution based on the principle of electromagnetism and Maxwell's Equations. Therefore, it can potentially be a successful candidate for both research and clinical applications.

At low magnetic field strength, when the wavelength of  $B_1$  field is reasonably longer than the size of human body, the transmit  $B_1$  phase and receive  $B_1$  phase can be assumed to be equal using birdcage transceiver RF coil. This assumption was first exploited by Wen et al. on a 1.5 T MRI scanner (Wen, 2003). With mapped magnitude distribution of transmit  $B_1$  and estimated  $B_1$  phase, one channel is sufficient to solve the Helmholtz equation (2.17) for the electrical properties voxel by voxel. The advantage of this Helmholtz-equal-phase approach is it is readily applicable on clinical scanners (1.5 or 3T) equipped with a birdcage transceiver coil. For a specific region in the sample, e.g., near the center of the birdcage coil, the assumption holds reasonably well (Balidemaj et al., 2015b; van Lier et al., 2013). However, more significant error can occur near the peripheral region or at high static magnetic field. Also, with only one channel of  $B_1$  data, the central equations (2.15) and (2.16) of EPT cannot be solved whereas the Helmholtz equation results in considerable error near boundaries between regions with different electrical properties. In addition, the Laplacian operation on the  $B_1$  field in the Helmholtz equation can significantly amplify noise in the measured  $B_1$  data. Because of these drawbacks, current imaging performance of EPT using the Helmholtz equation and phase assumption is often limited in in vivo applications (van Lier et al., 2012; Voigt et al., 2011), making it difficult to acquire high resolution images.

In this thesis, several advanced EPT techniques have been proposed to address the current limitations. First of all, a general frame work utilizing multi-channel transmit or receive  $B_1$  fields was developed suitable for reconstructing electrical properties in a homogeneous region. The method overcomes the limitation of previous EPT relying on half-transceiver-phase assumption which is mainly valid under low field strength. Secondly, a gradient-based EPT concept was introduced to emphasize the importance of gradient information as carried in the central equations. It has been shown that using the calculated gradient of EP, the performance of EPT can be greatly improved with higher resistance to noise impact and better reconstruction near tissue boundaries. Using the gradient information is also advantageous with high sensitivity to detect low contrast of electrical properties, such as shown in Figure 6.2 in a simulation study or in Figure 5.5 in a phantom study. Thirdly, based on the Maxwell's equations, proton density ( $\rho$ ), which is carried in the measured magnitude of receive  $B_1$  field, is quantitatively reconstructed independent on certain empirical assumptions such as  $B_1$ -pattern symmetry or  $T_1$ - $\rho$  relationship. The extracted proton density could be useful for clinical applications which are associated with changes in tissue water homeostasis, such as multiple sclerosis (Laule et al., 2004), brain ischemia (Ayata and Ropper, 2002), brain tumor (Neeb et al., 2006) or interferon treatment of liver metastases (Andersson et al., 1989).

Based on the proposed gradient-based EPT method, in vivo images of electrical properties inside human brains were able to be obtained for the first time with high accuracy and refined details of brain structure. In addition, the electrical properties of rat tumor model were studied in vivo. In the imaging results, the difference of conductivity between tumor tissue and healthy muscle was found to be statistically significant.

Another interesting finding is that necrosis which happens inside tumor due to blood supply deficit further drives the increasing trend of tumor conductivity. In vivo monitoring of tumor's electrical properties change can potentially provide deep insight into the evolution of tumor tissue and serve as a tool for characterizing necrosis.

## **7.2 Future Work**

Although the results in this thesis hold promises, as a novel methodology, the proposed method for EPT have several limitations that are worthy of investigation in the future. Two promising future applications of EPT will also be discussed later in 7.2.2 Prospective Applications.

### **7.2.1 Technical Development**

One particular challenge for EPT is its intrinsic sensitivity to noise in measured  $B_1$  field. Currently, multiple measurements are repeated to achieve enough SNR. This will lengthen the scan time, reduce subject comfort and make the result subjective to motion artifact. Fast  $B_1$ -mapping can provide more averages in limited amount of time. This can be achieved in two directions: one by optimizing the current imaging sequence such as shortened TR and another by developing novel  $B_1$ -mapping mechanisms. However, caution should be taken because the SNR of mapped  $B_1$  field is related to the parameters or methods employed. The complete transfer function of error from measurement noise to final complex  $B_1$  field should be carefully studied. Design of EPT algorithms can also play a significant role in reducing scan time. In general, transmit  $B_1$ -based EPT algorithm requires more scan time because individual channels transmit one after another while all receive channels can detect the signal at the same time. Besides the proposed multi-channel receive  $B_1$ -based EPT algorithms in Chapter 3, a recent relative

$B_1$  sensitivity-based EPT algorithm (Marques et al., 2015) can further speed up data acquisition because it avoids T1-bias which occurs with a short TR. However, pure receive  $B_1$ -based EPT algorithms cannot pass around the proton density bias and boundary artifacts related to inhomogeneous EP distribution.

Advanced numerical strategy will be another area of beneficial investigation. Three kinds of unknowns, including EP, absolute  $B_1$  phase and proton density, exist in the EPT problem. In this thesis, these unknowns are derived step by step with EP in the last. The reason is that all of these unknowns are nonlinearly related to each other in a set of partial differential equations as can be seen in Eqs. (6.2) and (6.3). Future EPT algorithms which are capable of deriving all the unknowns in a single step will be beneficial to avoid error generated in previous steps from accumulation in the final EP result.

Including the proposed methods, EPT algorithms concerning inhomogeneous EP distribution involve the z-component of  $B_1$  field in their equations (Hafalir et al., 2014; Liu et al., 2014; Zhang et al., 2013b, 2010). However, currently there are no methods to directly access the  $B_z$  component using MRI. In this thesis, using the longitudinal microstrip coil elements, satisfactory results were obtained by neglecting  $B_z$  near the middle section of the coil along the z-axis, following the similar strategy adopted in previous EPT studies (Hafalir et al., 2014; Liu et al., 2014; Zhang et al., 2013b). This can be seen as a restrictive condition limited to certain types of coil geometry, potentially incompatible with other coil elements involving a larger  $B_z$  contribution, such as loop coils with conductors perpendicular to the z-axis. Using Gauss's Law for magnetism,  $B_z$  can be incorporated in EPT framework (Katscher et al., 2015b; Katscher and Djamshidi,

2013; Sodickson et al., 2013) with much more complexity. The practical feasibility remains to be demonstrated.

### **7.2.2 Prospective Applications**

#### ***Breast Cancer***

Breast cancer is the most deadly cancer found among women with more than 230 thousand new cases in the US each year. Early diagnosis and detection is critical to improve survival rate of breast cancer patients. Mammography has been the main tool for breast cancer screening. But its employed X-ray is radioactive, and its sensitivity is only 48% in patients with dense breasts (Kolb et al., 2002). Ultrasound can be used to overcome some limitations of mammography but not all. Ultrasound is useful to determine whether a mass shown in mammography is cystic and can be ignored or solid and needs further examination. But ultrasound is not helpful to estimate the extent of tumor or find additional foci. The sensitivity of ultrasound combined with mammography is low in women with high risk of breast cancer (Kuhl et al., 2005). Although Gadolinium-based contrast MRI shows high sensitivity in population with high risk of breast cancer, its specificity to differentiate malignant and benign tissue is around 70% (Hlawatsch et al., 2002).

The electrical properties could be explored as a new imaging contrast for diagnosing breast cancer. Because adipose tissue is dominant in breast, breast tumor has a large contrast of electrical properties compared to normal breast tissue. Studies also suggest the difference of electrical properties between malignant and benign breast tissue (Katscher et al., 2015a). The current gradient-based EPT approach is very promising for imaging breast because the breast tissue is highly inhomogeneous and differences of

electrical properties between breast tissues are larger compared to those in other organs. To develop a valuable EPT method for clinical application of breast tumor diagnosis, suitable  $B_1$  mapping protocol for fatty breast tissue, RF coil fitting breast anatomy with high sensitivity and reconstruction algorithms should be further developed. Both healthy subjects and breast cancer patients at different stages will be recruited to investigate the clinical value of EPT.

### ***Quantification of Tissue Heating and Application at High Field***

Elevated thermal effects due to tissue heating accompany with increased main magnetic field strength, posing a safety concern in high field MRI applications (Lattanzi et al., 2009). MRI benefits from increase field strength with improved intrinsic signal to noise ratio, enhanced fMRI contrast, enlarged spectral difference and susceptibility contrast (Uğurbil et al., 2003; Duyn, 2012). However, one challenge encountered at high field strength is inhomogeneous  $B_1$  field coverage when the RF wavelength comes close to the size of human body. Parallel transmission technique that uses independent multiple RF transmit channels has been exploited to overcome the inhomogeneous  $B_1$  coverage, but can further induce concerns about RF safety due to increased complexity and freedom of RF power deposition in the body (Katscher et al., 2003; Zhu, 2004; Boulant et al., 2014). Specific Absorption Rate (SAR) is a quantity that measures the power of RF-induced heating (Collins et al., 2004). Using parallel transmission scheme for pulse design, it is possible to explicitly utilize predicted SAR or temperature change to design RF pulse that satisfies safety constraints.

SAR can be predicted based on forward simulation of RF coil and generic models of human electrical properties at Larmor frequency (Collins, 2009). However, this

approach can miss a subject-specific SAR pattern and is time consuming, with millions of grids to be calculated in simulation. On the other hand, the estimated absolute  $B_1$  phase and electrical properties as shown in this thesis can be used to quantify SAR of a specific subject undergoing a scan (Zhang et al., 2013a) and predict temperature change given a reasonable heat transferring model of the imaged object (Zhang et al., 2014). It will be potentially very useful to use the predicted SAR based on EPT outcome to optimize RF pulse design in the parallel transmission scheme. The ultimate goal is to obtain improved MRI performance at high field with subject-specifically optimized parallel transmission design.



## Reference

- Aberg, P., Nicander, I., Hansson, J., Geladi, P., Holmgren, U., Ollmar, S., 2004. Skin cancer identification using multifrequency electrical impedance-a potential screening tool. *IEEE Trans. Biomed. Eng.* 51, 2097–2102. doi:10.1109/TBME.2004.836523
- Adriany, G., Van de Moortele, P.-F., Ritter, J., Moeller, S., Auerbach, E.J., Akgün, C., Snyder, C.J., Vaughan, T., Uğurbil, K., 2008. A geometrically adjustable 16-channel transmit/receive transmission line array for improved RF efficiency and parallel imaging performance at 7 Tesla. *Magn. Reson. Med.* 59, 590–597. doi:10.1002/mrm.21488
- Adriany, G., Van de Moortele, P.-F., Wiesinger, F., Moeller, S., Strupp, J.P., Andersen, P., Snyder, C., Zhang, X., Chen, W., Pruessmann, K.P., Boesiger, P., Vaughan, T., Uğurbil, K., 2005. Transmit and receive transmission line arrays for 7 Tesla parallel imaging. *Magn. Reson. Med.* 53, 434–445. doi:10.1002/mrm.20321
- Akoka, S., Franconi, F., Seguin, F., Le Pape, A., 1993. Radiofrequency map of an NMR coil by imaging. *Magn. Reson. Imaging* 11, 437–441. doi:10.1016/0730-725X(93)90078-R
- Andersson, T., Ericsson, A., Eriksson, B., Hemmingsson, A., Lindh, E., Nyman, R., Oberg, K., 1989. Relative proton density and relaxation times in liver metastases during interferon treatment. *Br. J. Radiol.* 62, 433–437. doi:10.1259/0007-1285-62-737-433
- Ashburner, J., Friston, K.J., 2005. Unified segmentation. *NeuroImage* 26, 839–851. doi:10.1016/j.neuroimage.2005.02.018
- Assaf, B.A., Ebersole, J.S., 1997. Continuous Source Imaging of Scalp Ictal Rhythms in Temporal Lobe Epilepsy. *Epilepsia* 38, 1114–1123. doi:10.1111/j.1528-1157.1997.tb01201.x
- Ayata, C., Ropper, A.H., 2002. Ischaemic brain oedema. *J. Clin. Neurosci.* 9, 113–124. doi:10.1054/jocn.2001.1031
- Babsky, A.M., Hekmatyar, S.K., Zhang, H., Solomon, J.L., Bansal, N., 2005. Application of <sup>23</sup>Na MRI to Monitor Chemotherapeutic Response in RIF-1 Tumors. *Neoplasia N. Y.* 7, 658–666.
- Balidemaj, E., de Boer, P., Crezee, H., Remis, R., Lukas, S., Nederveen, A., van den Berg, C.A.T., 2015a. In vivo reconstructed conductivity values of cervical cancer patients based on EPT at 3T MRI, in: *Proc. Intl. Soc. Mag. Reson. Med.* 23.
- Balidemaj, E., van Lier, A.L.H.M.W., Crezee, H., Nederveen, A.J., Stalpers, L.J.A., van den Berg, C.A.T., 2015b. Feasibility of Electric Property Tomography of pelvic tumors at 3T. *Magn. Reson. Med.* 73, 1505–1513. doi:10.1002/mrm.25276
- Barber, C.C., Brown, B.H., 1983. Imaging spatial distributions of resistivity using applied potential tomography. *Electron. Lett.* 19, 933–935. doi:10.1049/el:19830637
- Benabid, A.L., Pollak, P., Gervason, C., Hoffmann, D., Gao, D.M., Hommel, M., Perret, J.E., de Rougemont, J., 1991. Long-term suppression of tremor by chronic stimulation of the ventral intermediate thalamic nucleus. *Lancet Lond. Engl.* 337, 403–406.

- Blankman, P., Hasan, D., van Mourik, M.S., Gommers, D., 2013. Ventilation distribution measured with EIT at varying levels of pressure support and Neurally Adjusted Ventilatory Assist in patients with ALI. *Intensive Care Med.* 39, 1057–1062. doi:10.1007/s00134-013-2898-8
- Bloch, F., 1946. Nuclear Induction. *Phys. Rev.* 70, 460–474. doi:10.1103/PhysRev.70.460
- Boulant, N., Massire, A., Amadon, A., Vignaud, A., 2014. Radiofrequency pulse design in parallel transmission under strict temperature constraints. *Magn. Reson. Med.* 72, 679–688. doi:10.1002/mrm.24974
- Brace, C.L., 2008. Temperature-dependent dielectric properties of liver tissue measured during thermal ablation: toward an improved numerical model. *Conf. Proc. Annu. Int. Conf. IEEE Eng. Med. Biol. Soc. IEEE Eng. Med. Biol. Soc. Annu. Conf.* 2008, 230–233. doi:10.1109/IEMBS.2008.4649132
- Brown, B., 2003. Electrical impedance tomography (EIT): a review. *J. Med. Eng. Technol.* 27, 97–108.
- Burnes, J.E., Taccardi, B., MacLeod, R.S., Rudy, Y., 2000. Noninvasive ECG Imaging of Electrophysiologically Abnormal Substrates in Infarcted Hearts A Model Study. *Circulation* 101, 533–540. doi:10.1161/01.CIR.101.5.533
- Cakirer, S., Karaarslan, E., Arslan, A., 2003. Spontaneously T1-hyperintense lesions of the brain on MRI: a pictorial review. *Curr. Probl. Diagn. Radiol.* 32, 194–217. doi:10.1016/S0363-0188(03)00026-4
- Cheney, M., Isaacson, D., Newell, J.C., 1999. Electrical Impedance Tomography. *SIAM Rev.* 41, 85–101.
- Christ, A., Kainz, W., Hahn, E.G., Honegger, K., Zefferer, M., Neufeld, E., Rascher, W., Janka, R., Bautz, W., Chen, J., Kiefer, B., Schmitt, P., Hollenbach, H.-P., Shen, J., Oberle, M., Szczerba, D., Kam, A., Guag, J.W., Kuster, N., 2010. The Virtual Family—development of surface-based anatomical models of two adults and two children for dosimetric simulations. *Phys. Med. Biol.* 55, N23. doi:10.1088/0031-9155/55/2/N01
- Cole, K.S., Cole, R.H., 1941. Dispersion and Absorption in Dielectrics I. Alternating Current Characteristics. *J. Chem. Phys.* 9, 341–351. doi:10.1063/1.1750906
- Collins, C.M., 2009. Numerical field calculations considering the human subject for engineering and safety assurance in MRI. *NMR Biomed.* 22, 919–926. doi:10.1002/nbm.1251
- Collins, C.M., Liu, W., Wang, J., Gruetter, R., Vaughan, J.T., Ugurbil, K., Smith, M.B., 2004. Temperature and SAR calculations for a human head within volume and surface coils at 64 and 300 MHz. *J. Magn. Reson. Imaging JMRI* 19, 650–656. doi:10.1002/jmri.20041
- D. C. Walker, B.H.B., 2000. Modelling the electrical impedivity of normal and premalignant cervical tissue. *Electron. Lett.* 36, 1603 – 1604. doi:10.1049/el:20001118
- Duan, Q., van Gelderen, P., Duyn, J., 2013. Improved Bloch-Siegert based B1 mapping by reducing off-resonance shift. *NMR Biomed.* 26, 1070–1078. doi:10.1002/nbm.2920

- Duyn, J.H., 2012. The future of ultra-high field MRI and fMRI for study of the human brain. *NeuroImage*, 20 YEARS OF fMRI 20 YEARS OF fMRI 62, 1241–1248. doi:10.1016/j.neuroimage.2011.10.065
- Epstein, B.R., Foster, K.R., 1983. Anisotropy in the dielectric properties of skeletal muscle. *Med. Biol. Eng. Comput.* 21, 51–55. doi:10.1007/BF02446406
- European Stroke Initiative Executive Committee, EUSI Writing Committee, Olsen, T.S., Langhorne, P., Diener, H.C., Hennerici, M., Ferro, J., Sivenius, J., Wahlgren, N.G., Bath, P., 2003. European Stroke Initiative Recommendations for Stroke Management-update 2003. *Cerebrovasc. Dis. Basel Switz.* 16, 311–337.
- Fatouros, P.P., Marmarou, A., 1999. Use of magnetic resonance imaging for in vivo measurements of water content in human brain: method and normal values. *J. Neurosurg.* 90, 109–115. doi:10.3171/jns.1999.90.1.0109
- Foster, K.R., Schepps, J.L., 1981. Dielectric properties of tumor and normal tissues at radio through microwave frequencies. *J. Microw. Power* 16, 107–119.
- Foster, K.R., Schwan, H.P., 1989. Dielectric properties of tissues and biological materials: a critical review. *Crit. Rev. Biomed. Eng.* 17, 25–104.
- Fricke, H., 1953. The Maxwell-Wagner Dispersion in a Suspension of Ellipsoids. *J. Phys. Chem.* 57, 934–937. doi:10.1021/j150510a018
- Gabriel, C., Gabriel, S., Corthout, E., 1996. The dielectric properties of biological tissues: I. Literature survey. *Phys. Med. Biol.* 41, 2231–2249. doi:10.1088/0031-9155/41/11/001
- Gabriel, C., Peyman, A., Grant, E.H., 2009. Electrical conductivity of tissue at frequencies below 1 MHz. *Phys. Med. Biol.* 54, 4863–4878. doi:10.1088/0031-9155/54/16/002
- Gabriel, S., Lau, R.W., Gabriel, C., 1996a. The dielectric properties of biological tissues: III. Parametric models for the dielectric spectrum of tissues. *Phys. Med. Biol.* 41, 2271–2293. doi:10.1088/0031-9155/41/11/003
- Gabriel, S., Lau, R.W., Gabriel, C., 1996b. The dielectric properties of biological tissues: II. Measurements in the frequency range 10 Hz to 20 GHz. *Phys. Med. Biol.* 41, 2251–2269. doi:10.1088/0031-9155/41/11/002
- Gandhi, O.P., Chen, X.B., 1999. Specific absorption rates and induced current densities for an anatomy-based model of the human for exposure to time-varying magnetic fields of MRI. *Magn. Reson. Med.* 41, 816–823. doi:10.1002/(SICI)1522-2594(199904)41:4<816::AID-MRM22>3.0.CO;2-5
- Gao, N., He, B., 2008. Noninvasive Imaging of Bioimpedance Distribution by Means of Current Reconstruction Magnetic Resonance Electrical Impedance Tomography. *IEEE Trans. Biomed. Eng.* 55, 1530–1538. doi:10.1109/TBME.2008.918565
- Gelman, N., Ewing, J.R., Gorell, J.M., Spickler, E.M., Solomon, E.G., 2001. Interregional variation of longitudinal relaxation rates in human brain at 3.0 T: relation to estimated iron and water contents. *Magn. Reson. Med.* 45, 71–79.
- George, M., Lisanby, S., Sackeim, H., 1999. Transcranial magnetic stimulation: Applications in neuropsychiatry. *Arch. Gen. Psychiatry* 56, 300–311. doi:10.1001/archpsyc.56.4.300
- Grant, P.F., Lowery, M.M., 2010. Effect of dispersive conductivity and permittivity in volume conductor models of deep brain stimulation. *IEEE Trans. Biomed. Eng.* 57, 2386–2393. doi:10.1109/TBME.2010.2055054

- Griffiths, H., 2001. Magnetic induction tomography. *Meas. Sci. Technol.* 12, 1126–1131. doi:10.1088/0957-0233/12/8/319
- Griffiths, H., Stewart, W.R., Gough, W., 1999. Magnetic Induction Tomography: A Measuring System for Biological Tissues. *Ann. N. Y. Acad. Sci.* 873, 335–345. doi:10.1111/j.1749-6632.1999.tb09481.x
- Güllmar, D., Haueisen, J., Reichenbach, J.R., 2010. Influence of anisotropic electrical conductivity in white matter tissue on the EEG/MEG forward and inverse solution. A high-resolution whole head simulation study. *NeuroImage* 51, 145–163. doi:10.1016/j.neuroimage.2010.02.014
- Haacke, E.M., Petropoulos, L.S., Nilges, E.W., Wu, D.H., 1991. Extraction of conductivity and permittivity using magnetic resonance imaging. *Phys. Med. Biol.* 36, 723–734. doi:10.1088/0031-9155/36/6/002
- Haemmerich, D., Staelin, S.T., Tsai, J.Z., Tungjitkusolmun, S., Mahvi, D.M., Webster, J.G., 2003. In vivo electrical conductivity of hepatic tumours. *Physiol. Meas.* 24, 251–260.
- Hafalir, F.S., Oran, O.F., Gurler, N., Ider, Y.Z., 2014. Convection-reaction equation based magnetic resonance electrical properties tomography (cr-MREPT). *IEEE Trans. Med. Imaging* 33, 777–793. doi:10.1109/TMI.2013.2296715
- Halter, R.J., Schned, A., Heaney, J., Hartov, A., Paulsen, K.D., 2009. Electrical Properties of Prostatic Tissues: I. Single Frequency Admittivity Properties. *J. Urol.* 182, 1600–1607. doi:10.1016/j.juro.2009.06.007
- Hancu, I., Roberts, J.C., Bulumulla, S., Lee, S.-K., 2015. On conductivity, permittivity, apparent diffusion coefficient, and their usefulness as cancer markers at MRI frequencies. *Magn. Reson. Med.* 73, 2025–2029. doi:10.1002/mrm.25309
- He, B., 1999. Brain electric source imaging: scalp Laplacian mapping and cortical imaging. *Crit. Rev. Biomed. Eng.* 27, 149–188.
- He, B., Cohen, R.J., 1992. Body surface Laplacian mapping of cardiac electrical activity. *Am. J. Cardiol.* 70, 1617–1620. doi:10.1016/0002-9149(92)90471-A
- Hiraoka, M., Jo, S., Dodo, Y., Ono, K., Takahashi, M., Nishida, H., Abe, M., 1984. Clinical results of radiofrequency hyperthermia combined with radiation in the treatment of radioresistant cancers. *Cancer* 54, 2898–2904. doi:10.1002/1097-0142(19841215)54:12<2898::AID-CNCR2820541214>3.0.CO;2-B
- Hlawatsch, A., Teifke, A., Schmidt, M., Thelen, M., 2002. Preoperative assessment of breast cancer: sonography versus MR imaging. *AJR Am. J. Roentgenol.* 179, 1493–1501. doi:10.2214/ajr.179.6.1791493
- Holder, D.S., 1992. Detection of cerebral ischaemia in the anaesthetised rat by impedance measurement with scalp electrodes: implications for non-invasive imaging of stroke by electrical impedance tomography. *Clin. Phys. Physiol. Meas. Off. J. Hosp. Phys. Assoc. Dtsch. Ges. Für Med. Phys. Eur. Fed. Organ. Med. Phys.* 13, 63–75.
- Hoult, D.I., 2000. The principle of reciprocity in signal strength calculations—A mathematical guide. *Concepts Magn. Reson.* 12, 173–187. doi:10.1002/1099-0534(2000)12:4<173::AID-CMR1>3.0.CO;2-Q
- Hu, G., Cressman, E., He, B., 2011. Magnetoacoustic imaging of human liver tumor with magnetic induction. *Appl. Phys. Lett.* 98, 23703. doi:10.1063/1.3543630

- Huhndorf, M., Stehning, C., Rohr, A., Helle, M., Katscher, U., Jansen, O., 2013. Systematic Brain Tumor Conductivity Study with Optimized EPT Sequence and Reconstruction Algorithm. Presented at the ISMRM, Salt Lake City, USA, p. 3626.
- Hurt, W.D., 1985. Multiterm Debye Dispersion Relations for Permittivity of Muscle. *IEEE Trans. Biomed. Eng. BME-32*, 60–64. doi:10.1109/TBME.1985.325629
- Isaacs, J.T., Isaacs, W.B., Feitz, W.F., Scheres, J., 1986. Establishment and characterization of seven Dunning rat prostatic cancer cell lines and their use in developing methods for predicting metastatic abilities of prostatic cancers. *The Prostate* 9, 261–281.
- Iserles, A., 2009. A first course in the numerical analysis of differential equations, 2nd ed. ed. Cambridge University Press, Cambridge, UK ; New York.
- Jakobsen, I., Kaalhus, O., Lyng, H., Rofstad, E.K., 1995. Detection of necrosis in human tumour xenografts by proton magnetic resonance imaging. *Br. J. Cancer* 71, 456–461.
- Joines, W.T., 1994. The measured electrical properties of normal and malignant human tissues from 50 to 900 MHz. *Med. Phys.* 21, 547–550. doi:10.1118/1.597312
- Jossinet, J., 1998. The impedivity of freshly excised human breast tissue. *Physiol. Meas.* 19, 61–75.
- Joy, M., Scott, G., Henkelman, M., 1989. In vivo detection of applied electric currents by magnetic resonance imaging. *Magn. Reson. Imaging* 7, 89–94. doi:16/0730-725X(89)90328-7
- Just, M., Thelen, M., 1988. Tissue characterization with T1, T2, and proton density values: results in 160 patients with brain tumors. *Radiology* 169, 779–785.
- Katscher, U., Abe, H., Ivancevic, M., Keupp, J., 2015a. Investigating breast tumor malignancy with electric conductivity measurement, in: *Proceedings of the 23th Annual Meeting of ISMRM*. Toronto, Canada, p. 3306.
- Katscher, U., Börnert, P., Leussler, C., van den Brink, J.S., 2003. Transmit SENSE. *Magn. Reson. Med.* 49, 144–150. doi:10.1002/mrm.10353
- Katscher, U., Braun, M., Findelee, C., Leussler, C., Graesslin, I., Vernickel, P., Morlock, M., 2015b. B1-based SAR determination for local RF transmit coils, in: *Proceedings of the 23rd Annual Meeting of ISMRM*. Toronto, ON, Canada, p. 383.
- Katscher, U., Djamshidi, K., 2013. Improving B1-based SAR determination via iterative determination of missing field components, in: *Proceedings of the 21st Annual Meeting of ISMRM*. Salt Lake City, USA, p. 4410.
- Katscher, U., Findelee, C., Voigt, T., 2012. B1-based specific energy absorption rate determination for nonquadrature radiofrequency excitation. *Magn. Reson. Med.* 68, 1911–1918. doi:10.1002/mrm.24215
- Katscher, U., Voigt, T., Findelee, C., Vernickel, P., Nehrke, K., Dossel, O., 2009. Determination of Electric Conductivity and Local SAR Via B1 Mapping. *Med. Imaging IEEE Trans. On* 28, 1365–1374. doi:10.1109/TMI.2009.2015757
- Katscher, U., Voigt, T., Findelee, C., Vernickel, P., Nehrke, K., Dossel, O., 2009. Determination of Electric Conductivity and Local SAR Via B1 Mapping. *IEEE Trans. Med. Imag.* 28, 1365–1374. doi:10.1109/TMI.2009.2015757

- Kim, H.J., Kim, Y.T., Minhas, A.S., Jeong, W.C., Woo, E.J., Seo, J.K., Kwon, O.J., 2009. In Vivo High-Resolution Conductivity Imaging of the Human Leg Using MREIT: The First Human Experiment. *Med. Imaging IEEE Trans. On* 28, 1681–1687. doi:10.1109/TMI.2009.2018112
- Kim, H.J., Lee, B.I., Cho, Y., Kim, Y.T., Kang, B.T., Park, H.M., Lee, S.Y., Seo, J.K., Woo, E.J., 2007. Conductivity imaging of canine brain using a 3 T MREIT system: postmortem experiments. *Physiol. Meas.* 28, 1341–1353. doi:10.1088/0967-3334/28/11/002
- Kolb, T.M., Lichy, J., Newhouse, J.H., 2002. Comparison of the performance of screening mammography, physical examination, and breast US and evaluation of factors that influence them: an analysis of 27,825 patient evaluations. *Radiology* 225, 165–175. doi:10.1148/radiol.2251011667
- Kozlov, M., Turner, R., 2009. Fast MRI coil analysis based on 3-D electromagnetic and RF circuit co-simulation. *J. Magn. Reson.* 200, 147–152. doi:10.1016/j.jmr.2009.06.005
- Kuhl, C.K., Schrading, S., Leutner, C.C., Morakkabati-Spitz, N., Wardelmann, E., Fimmers, R., Kuhn, W., Schild, H.H., 2005. Mammography, Breast Ultrasound, and Magnetic Resonance Imaging for Surveillance of Women at High Familial Risk for Breast Cancer. *J. Clin. Oncol.* 23, 8469–8476. doi:10.1200/JCO.2004.00.4960
- Lattanzi, R., Sodickson, D.K., Grant, A.K., Zhu, Y., 2009. Electrodynamics constraints on homogeneity and radiofrequency power deposition in multiple coil excitations. *Magn. Reson. Med.* 61, 315–334. doi:10.1002/mrm.21782
- Laule, C., Vavasour, I.M., Moore, G.R.W., Oger, J., Li, D.K.B., Paty, D.W., MacKay, A.L., 2004. Water content and myelin water fraction in multiple sclerosis. A T2 relaxation study. *J. Neurol.* 251, 284–293. doi:10.1007/s00415-004-0306-6
- Lauterbur, P.C., 1973. Image Formation by Induced Local Interactions: Examples Employing Nuclear Magnetic Resonance. *Nature* 242, 190–191. doi:10.1038/242190a0
- Lemdiasov, R.A., Obi, A.A., Ludwig, R., 2011. A numerical postprocessing procedure for analyzing radio frequency MRI coils. *Concepts Magn. Reson. Part A* 38A, 133–147. doi:10.1002/cmr.a.20217
- Limousin, P., Krack, P., Pollak, P., Benazzouz, A., Ardouin, C., Hoffmann, D., Benabid, A.-L., 1998. Electrical Stimulation of the Subthalamic Nucleus in Advanced Parkinson's Disease. *N. Engl. J. Med.* 339, 1105–1111. doi:10.1056/NEJM199810153391603
- Liu, J., Wang, Y., Zhang, X., Van De Moortele, P.-F., He, B., 2015a. PDE Solution of Electrical Properties Tomography With Multi-channel B1 Transmission, in: *Proceedings of the 23th Annual Meeting of ISMRM*. Toronto, ON, Canada, p. 3300.
- Liu, J., Zhang, X., Schmitter, S., Van de Moortele, P.-F., He, B., 2014. Gradient-based electrical properties tomography (gEPT): A robust method for mapping electrical properties of biological tissues in vivo using magnetic resonance imaging. *Magn. Reson. Med.* doi:10.1002/mrm.25434
- Liu, J., Zhang, X., Van de Moortele, P.-F., Schmitter, S., He, B., 2013. Determining electrical properties based on B(1) fields measured in an MR scanner using a

- multi-channel transmit/receive coil: a general approach. *Phys. Med. Biol.* 58, 4395–4408. doi:10.1088/0031-9155/58/13/4395
- Liu, J., Zhang, X., Wang, Y., Van de Moortele, P.-F., He, B., 2015b. Local Electrical Properties Tomography With Global Regularization By Gradient, in: *Proceedings of the 23th Annual Meeting of ISMRM*. Toronto, ON, Canada, p. 3297.
- Liu, Z., Liu, C., He, B., 2006. Noninvasive reconstruction of three-dimensional ventricular activation sequence from the inverse solution of distributed equivalent current density. *IEEE Trans. Med. Imaging* 25, 1307–1318.
- Li, X., He, B., 2010. Multi-excitation magnetoacoustic tomography with magnetic induction for bioimpedance imaging. *IEEE Trans. Med. Imaging* 29, 1759–1767. doi:10.1109/TMI.2010.2052063
- Li, X., Xu, Y., He, B., 2007. Imaging Electrical Impedance From Acoustic Measurements by Means of Magnetoacoustic Tomography With Magnetic Induction (MAT-MI). *IEEE Trans. Biomed. Eng.* 54, 323–330. doi:10.1109/TBME.2006.883827
- Lorenzo Mannelli, S.K., 2009. Assessment of Tumor Necrosis of Hepatocellular Carcinoma After Chemoembolization: Diffusion-Weighted and Contrast-Enhanced MRI With Histopathologic Correlation of the Explanted Liver. *AJR Am. J. Roentgenol.* 193, 1044–52. doi:10.2214/AJR.08.1461
- Lukaski, H.C., Johnson, P.E., Bolonchuk, W.W., Lykken, G.I., 1985. Assessment of fat-free mass using bioelectrical impedance measurements of the human body. *Am. J. Clin. Nutr.* 41, 810–817.
- Lux, H.D., Heinemann, U., Dietzel, I., 1986. Ionic changes and alterations in the size of the extracellular space during epileptic activity. *Adv. Neurol.* 44, 619–639.
- Lyng, H., Haraldseth, O., Rofstad, E.K., 2000. Measurement of cell density and necrotic fraction in human melanoma xenografts by diffusion weighted magnetic resonance imaging. *Magn. Reson. Med.* 43, 828–836.
- Malmivuo, J., Plonsey, R., 1995. *Bioelectromagnetism*. Oxford University Press, New York.
- Mansfield, P., 1977. Multi-planar image formation using NMR spin echoes. *J. Phys. C Solid State Phys.* 10, L55–L58. doi:10.1088/0022-3719/10/3/004
- Mariappan, L., He, B., 2013. Magnetoacoustic Tomography with Magnetic Induction: Bioimpedance reconstruction through vector source imaging. *IEEE Trans. Med. Imaging* 32, 619–627. doi:10.1109/TMI.2013.2239656
- Marques, J.P., Sodickson, D.K., Ipek, O., Collins, C.M., Gruetter, R., 2015. Single acquisition electrical property mapping based on relative coil sensitivities: A proof-of-concept demonstration. *Magn. Reson. Med.* 74, 185–195. doi:10.1002/mrm.25399
- Maxwell, J.C., 1865. A Dynamical Theory of the Electromagnetic Field. *Philos. Trans. R. Soc. Lond.* 155, 459–512. doi:10.1098/rstl.1865.0008
- Metherall, P., Barber, D.C., Smallwood, R.H., Brown, B.H., 1996. Three-dimensional electrical impedance tomography. *Nature* 380, 509–512. doi:10.1038/380509a0
- Metzger, G.J., van de Moortele, P.-F., Akgun, C., Snyder, C.J., Moeller, S., Strupp, J., Andersen, P., Shrivastava, D., Vaughan, T., Ugurbil, K., Adriany, G., 2010. Performance of external and internal coil configurations for prostate investigations at 7 T. *Magn. Reson. Med. Off. J. Soc. Magn. Reson. Med. Soc. Magn. Reson. Med.* 64, 1625–1639. doi:10.1002/mrm.22552

- Michel, C.M., Murray, M.M., Lantz, G., Gonzalez, S., Spinelli, L., Grave de Peralta, R., 2004. EEG source imaging. *Clin. Neurophysiol.* 115, 2195–2222. doi:10.1016/j.clinph.2004.06.001
- Mueller, J.L., Isaacson, D., Newell, J.C., 1999. A reconstruction algorithm for electrical impedance tomography data collected on rectangular electrode arrays. *IEEE Trans. Biomed. Eng.* 46, 1379–1386. doi:10.1109/10.797998
- Neeb, H., Zilles, K., Shah, N.J., 2006. A new method for fast quantitative mapping of absolute water content in vivo. *NeuroImage* 31, 1156–1168. doi:10.1016/j.neuroimage.2005.12.063
- Nehrke, K., Börner, P., 2012. DREAM—a novel approach for robust, ultrafast, multislice B1 mapping. *Magn. Reson. Med.* 68, 1517–1526. doi:10.1002/mrm.24158
- Oh, S.H., Han, J.Y., Lee, S.Y., Cho, M.H., Lee, B.I., Woo, E.J., 2003a. Electrical conductivity imaging by magnetic resonance electrical impedance tomography (MREIT). *Magn. Reson. Med.* 50, 875–878. doi:10.1002/mrm.10588
- Oh, S.H., Lee, B.I., Woo, E.J., Lee, S.Y., Cho, M.H., Kwon, O., Seo, J.K., 2003b. Conductivity and current density image reconstruction using harmonic Bz algorithm in magnetic resonance electrical impedance tomography. *Phys. Med. Biol.* 48, 3101–3116.
- O'Rourke, A.P., Lazebnik, M., Bertram, J.M., Converse, M.C., Hagness, S.C., Webster, J.G., Mahvi, D.M., 2007. Dielectric properties of human normal, malignant and cirrhotic liver tissue: in vivo and ex vivo measurements from 0.5 to 20 GHz using a precision open-ended coaxial probe. *Phys. Med. Biol.* 52, 4707–4719. doi:10.1088/0031-9155/52/15/022
- Orzada, S., Johst, S., Maderwald, S., Bitz, A.K., Solbach, K., Ladd, M.E., 2013. Mitigation of B1(+) inhomogeneity on single-channel transmit systems with TIAMO. *Magn. Reson. Med.* 70, 290–294. doi:10.1002/mrm.24453
- Osama, R.M., Abdelmaksoud, A.H.K., El Tatawy, S.A.M., Nabeel, M.M., Metwally, L.I.A., 2013. Role of dynamic contrast-enhanced and diffusion weighted MRI in evaluation of necrosis of hepatocellular carcinoma after chemoembolization. *Egypt. J. Radiol. Nucl. Med.* 44, 737–746. doi:10.1016/j.ejnm.2013.09.012
- Pappone, C., Rosanio, S., Oreto, G., Tocchi, M., Gugliotta, F., Vicedomini, G., Salvati, A., Dicandia, C., Mazzone, P., Santinelli, V., Gulletta, S., Chierchia, S., 2000. Circumferential Radiofrequency Ablation of Pulmonary Vein Ostia A New Anatomic Approach for Curing Atrial Fibrillation. *Circulation* 102, 2619–2628. doi:10.1161/01.CIR.102.21.2619
- Park, C., Park, E.-J., Woo, E.J., Kwon, O., Seo, J.K., 2004. Static conductivity imaging using variational gradient Bz algorithm in magnetic resonance electrical impedance tomography. *Physiol. Meas.* 25, 257–269.
- Paulson, K., Lionheart, W., Pidcock, M., 1993. Optimal experiments in electrical impedance tomography. *IEEE Trans. Med. Imaging* 12, 681–686. doi:10.1109/42.251118
- Pethig, R., 1984. Dielectric Properties of Biological Materials: Biophysical and Medical Applications. *IEEE Trans. Electr. Insul.* EI-19, 453–474. doi:10.1109/TEI.1984.298769



- Purcell, E.M., Torrey, H.C., Pound, R.V., 1946. Resonance Absorption by Nuclear Magnetic Moments in a Solid. *Phys. Rev.* 69, 37–38. doi:10.1103/PhysRev.69.37
- Rabi, I.I., Zacharias, J.R., Millman, S., Kusch, P., 1938. A New Method of Measuring Nuclear Magnetic Moment. *Phys. Rev.* 53, 318–318. doi:10.1103/PhysRev.53.318
- Rush, S., Abildskov, J.A., Mcfee, R., 1963. Resistivity of Body Tissues at Low Frequencies. *Circ. Res.* 12, 40–50. doi:10.1161/01.RES.12.1.40
- Sacolick, L.I., Wiesinger, F., Hancu, I., Vogel, M.W., 2010. B1 mapping by Bloch-Siegert shift. *Magn. Reson. Med.* 63, 1315–1322. doi:10.1002/mrm.22357
- Schmid, G., Neubauer, G., Illievich, U.M., Alesch, F., 2003. Dielectric properties of porcine brain tissue in the transition from life to death at frequencies from 800 to 1900 MHz. *Bioelectromagnetics* 24, 413–422. doi:10.1002/bem.10122
- Schroeder, M., Sadasiva, A., Nelson, R., 2008. An Analysis on the Role of Water Content and State on Effective Permittivity Using Mixing Formulas. *J. Biomech. Biomed. Biophys. Eng.* 2.
- Schwan, H.P., 1994. Electrical properties of tissues and cell suspensions: mechanisms and models, in: *Proceedings of the 16th Annual International Conference of the IEEE Engineering in Medicine and Biology Society, 1994. Engineering Advances: New Opportunities for Biomedical Engineers. Presented at the Proceedings of the 16th Annual International Conference of the IEEE Engineering in Medicine and Biology Society, 1994. Engineering Advances: New Opportunities for Biomedical Engineers*, pp. A70–A71 vol.1. doi:10.1109/IEMBS.1994.412155
- Schwan, H.P., 1957. Electrical properties of tissue and cell suspensions. *Adv. Biol. Med. Phys.* 5, 147–209.
- Scott, G.C., Joy, M.L., Armstrong, R.L., Henkelman, R.M., 1995. Rotating frame RF current density imaging. *Magn. Reson. Med.* 33, 355–369.
- Scott, G.C., Joy, M.L., Armstrong, R.L., Henkelman, R.M., 1991. Measurement of nonuniform current density by magnetic resonance. *IEEE Trans. Med. Imaging* 10, 362–374. doi:10.1109/42.97586
- Scott, G.C., Joy, M.L.G., Armstrong, R.L., Henkelman, R.M., 1992. RF Current Density Imaging in Homogeneous Media. *Magn. Reson. Med.* 28, 186–201. doi:10.1002/mrm.1910280203
- Seo, J.K., Kim, M.-O., Lee, J., Choi, N., Woo, E.J., Kim, H.J., Kwon, O.I., Kim, D.-H., 2012. Error analysis of nonconstant admittivity for MR-based electric property imaging. *IEEE Trans. Med. Imaging* 31, 430–437. doi:10.1109/TMI.2011.2171000
- Seo, J.K., Kim, S.W., Kim, S., Liu, J.J., Woo, E.J., Jeon, K., Lee, C.-O., 2008. Local Harmonic Algorithm With Domain Decomposition in MREIT: Computer Simulation Study. *IEEE Trans. Med. Imaging* 27, 1754–1761. doi:10.1109/TMI.2008.926055
- Seo, J.K., Yoon, J.-R., Woo, E.J., Kwon, O., 2003. Reconstruction of conductivity and current density images using only one component of magnetic field measurements. *IEEE Trans. Biomed. Eng.* 50, 1121–1124. doi:10.1109/TBME.2003.816080
- Sha, L., Ward, E.R., Stroy, B., 2002. A review of dielectric properties of normal and malignant breast tissue, in: *Proceedings IEEE SoutheastCon, 2002. Presented at*

- the Proceedings IEEE SoutheastCon, 2002, pp. 457–462.  
doi:10.1109/.2002.995639
- Shin, J., Kim, M.J., Lee, J., Nam, Y., Kim, M.-O., Choi, N., Kim, S., Kim, D.-H., 2014. Initial study on in vivo conductivity mapping of breast cancer using MRI. *J. Magn. Reson. Imaging JMRI*. doi:10.1002/jmri.24803
- Sodickson, D., Alon, L., Deniz, C., Ben-Eliezer, N., Cloos, M., Sodickson, L., Collins, C.M., Wiggins, G., Novikov, D., 2013. Generalized Local Maxwell Tomography for Mapping of Electrical Property Gradients and Tensors. Presented at the ISMRM, Salt Lake City, USA, p. 4175.
- Sodickson, D., Alon, L., Deniz, C., Brown, B., Zhang, B., Wiggins, G., Cho, G., Eliezer, N., Novikov, D., Lattanzi, R., Duan, Q., Sodickson, L., Zhu, Y., 2012. Local Maxwell Tomography Using Transmit-Receive Coil Arrays for Contact-Free Mapping of Tissue Electrical Properties and Determination of Absolute RF Phase. Presented at the ISMRM, Melbourne, Australia, p. 387.
- Stehning, C., Voigt, T., Katscher, U., 2011. Real-Time Conductivity Mapping using Balanced SSFP and Phase-Based Reconstruction, in: *Proc. Intl. Soc. Mag. Reson. Med.* 19. Montreal, Canada, p. 128.
- Stuchly, M.A., Athey, T.W., Stuchly, S.S., Samaras, G.M., Taylor, G., 1981. Dielectric properties of animal tissues in vivo at frequencies 10 MHz – 1 GHz. *Bioelectromagnetics* 2, 93–103. doi:10.1002/bem.2250020202
- Stuchly, M.A., Stuchly, S.S., 1980. Coaxial Line Reflection Methods for Measuring Dielectric Properties of Biological Substances at Radio and Microwave Frequencies-A Review. *IEEE Trans. Instrum. Meas.* 29, 176–183. doi:10.1109/TIM.1980.4314902
- Surowiec, A.J., Stuchly, S.S., Barr, J.R., Swarup, A., 1988. Dielectric properties of breast carcinoma and the surrounding tissues. *IEEE Trans. Biomed. Eng.* 35, 257–263. doi:10.1109/10.1374
- Uğurbil, K., Adriany, G., Andersen, P., Chen, W., Garwood, M., Gruetter, R., Henry, P.-G., Kim, S.-G., Lieu, H., Tkac, I., Vaughan, T., Van De Moortele, P.-F., Yacoub, E., Zhu, X.-H., 2003. Ultrahigh field magnetic resonance imaging and spectroscopy. *Magn. Reson. Imaging* 21, 1263–1281.
- Van de Moortele, P.-F., Akgun, C., Adriany, G., Moeller, S., Ritter, J., Collins, C.M., Smith, M.B., Vaughan, J.T., Uğurbil, K., 2005. B1 destructive interferences and spatial phase patterns at 7 T with a head transceiver array coil. *Magn. Reson. Med.* 54, 1503–1518. doi:10.1002/mrm.20708
- Van de Moortele, P.-F., Auerbach, E.J., Olman, C., Yacoub, E., Uğurbil, K., Moeller, S., 2009. T1 weighted brain images at 7 Tesla unbiased for Proton Density, T2\* contrast and RF coil receive B1 sensitivity with simultaneous vessel visualization. *NeuroImage* 46, 432–446. doi:10.1016/j.neuroimage.2009.02.009
- Van de Moortele, P.-F., Snyder, C., DelaBarre, L., Adriany, G., Vaughan, T., Uğurbil, K., 2007. Calibration Tools for RF Shim at Very High Field with Multiple Element RF Coils: from Ultra Fast Local Relative Phase to Absolute Magnitude B1+ Mapping, in: *Proc. Intl. Soc. Mag. Reson. Med.* 15. Berlin, Germany, p. 1676.
- Van de Moortele, P.-F., Uğurbil, K., 2009. Very Fast Multi Channel B1 Calibration at High Field in the Small Flip Angle Regime, in: *Proc. Intl. Soc. Mag. Reson. Med.* 17. Hawaii, USA, p. 367.

- van Lier, A.L., Brunner, D.O., Pruessmann, K.P., Klomp, D.W.J., Luijten, P.R., Lagendijk, J.J.W., van den Berg, C.A.T., 2012. B 1+ Phase mapping at 7 T and its application for in vivo electrical conductivity mapping. *Magn. Reson. Med.* 67, 552–561. doi:10.1002/mrm.22995
- van Lier, A.L.H.M.W., Raaijmakers, A., Voigt, T., Lagendijk, J.J.W., Luijten, P.R., Katscher, U., van den Berg, C.A.T., 2013. Electrical Properties Tomography in the Human Brain at 1.5, 3, and 7T: A Comparison Study. *Magn. Reson. Med. Off. J. Soc. Magn. Reson. Med. Soc. Magn. Reson. Med.* doi:10.1002/mrm.24637
- Voigt, T., Katscher, U., Doessel, O., 2011. Quantitative conductivity and permittivity imaging of the human brain using electric properties tomography. *Magn. Reson. Med.* 66, 456–466. doi:10.1002/mrm.22832
- Volz, S., Nöth, U., Deichmann, R., 2012a. Correction of systematic errors in quantitative proton density mapping. *Magn. Reson. Med.* 68, 74–85. doi:10.1002/mrm.23206
- Volz, S., Nöth, U., Jurcoane, A., Ziemann, U., Hattingen, E., Deichmann, R., 2012b. Quantitative proton density mapping: correcting the receiver sensitivity bias via pseudo proton densities. *NeuroImage* 63, 540–552. doi:10.1016/j.neuroimage.2012.06.076
- Wang, Y., Zhang, X., Liu, J., Van De Moortele, P.-F., He, B., 2015. Total Variance Constrained Electrical Properties Tomography Using a 16-Channel Transceiver Array Coil at 7T, in: *Proceedings of the 23th Annual Meeting of ISMRM*. Toronto, ON, Canada, p. 3303.
- Wang, Z., Lin, J.C., Mao, W., Liu, W., Smith, M.B., Collins, C.M., 2007. SAR and temperature: Simulations and comparison to regulatory limits for MRI. *J. Magn. Reson. Imaging* 26, 437–441. doi:10.1002/jmri.20977
- Weiskopf, N., Lutti, A., Helms, G., Novak, M., Ashburner, J., Hutton, C., 2011. Unified segmentation based correction of R1 brain maps for RF transmit field inhomogeneities (UNICORT). *NeuroImage* 54, 2116–2124. doi:10.1016/j.neuroimage.2010.10.023
- Wen, H., 2003. Noninvasive quantitative mapping of conductivity and dielectric distributions using RF wave propagation effects in high-field MRI, in: *Proc. SPIE*. San Diego, CA, USA, pp. 471–477. doi:10.1117/12.480000
- Woo, E.J., Hua, P., Webster, J.G., Tompkins, W.J., 1992. Measuring lung resistivity using electrical impedance tomography. *IEEE Trans. Biomed. Eng.* 39, 756–760. doi:10.1109/10.142651
- Woo, E.J., Seo, J.K., 2008. Magnetic resonance electrical impedance tomography (MREIT) for high-resolution conductivity imaging. *Physiol. Meas.* 29, R1–26. doi:10.1088/0967-3334/29/10/R01
- Xu, Y., He, B., 2005. Magnetoacoustic tomography with magnetic induction (MAT-MI). *Phys. Med. Biol.* 50, 5175–5187. doi:10.1088/0031-9155/50/21/015
- Yang, L., Worrell, G.A., Nelson, C., Brinkmann, B., He, B., 2012. Spectral and spatial shifts of post-ictal slow waves in temporal lobe seizures. *Brain J. Neurol.* 135, 3134–3143. doi:10.1093/brain/aws221
- Yarnykh, V.L., 2007. Actual flip-angle imaging in the pulsed steady state: A method for rapid three-dimensional mapping of the transmitted radiofrequency field. *Magn. Reson. Med.* 57, 192–200. doi:10.1002/mrm.21120

- Yoo, D., 2004. The dielectric properties of cancerous tissues in a nude mouse xenograft model. *Bioelectromagnetics* 25, 492–497. doi:10.1002/bem.20021
- Zhang, B., Sodickson, D.K., Lattanzi, R., Duan, Q., Stoeckel, B., Wiggins, G.C., 2012. Whole body traveling wave magnetic resonance imaging at high field strength: homogeneity, efficiency, and energy deposition as compared with traditional excitation mechanisms. *Magn. Reson. Med. Off. J. Soc. Magn. Reson. Med. Soc. Magn. Reson. Med.* 67, 1183–1193. doi:10.1002/mrm.23107
- Zhang, N., 1992. Electrical Impedance Tomography Based on Current Density Imaging (M.S. thesis). Univ. Toronto, Toronto, ON, Canada.
- Zhang, X., Moortele, P.-F.V. de, Liu, J., Schmitter, S., He, B., 2014. Quantitative prediction of radio frequency induced local heating derived from measured magnetic field maps in magnetic resonance imaging: A phantom validation at 7 T. *Appl. Phys. Lett.* 105, 244101. doi:10.1063/1.4903774
- Zhang, X., Schmitter, S., Van de Moortele, P.-F., Liu, J., He, B., 2013a. From Complex B1 Mapping to Local SAR Estimation for Human Brain MR Imaging Using Multi-channel Transceiver Coil at 7T. *IEEE Trans. Med. Imaging* 32, 1058–1067. doi:10.1109/TMI.2013.2251653
- Zhang, X., Van de Moortele, P.-F., Schmitter, S., He, B., 2013b. Complex B1 mapping and electrical properties imaging of the human brain using a 16-channel transceiver coil at 7T. *Magn. Reson. Med.* 69, 1285–1296. doi:10.1002/mrm.24358
- Zhang, X., Zhu, S., He, B., 2010. Imaging Electric Properties of Biological Tissues by RF Field Mapping in MRI. *IEEE Trans. Med. Imaging* 29, 474–481. doi:10.1109/TMI.2009.2036843
- Zhang, Y., van Drongelen, W., He, B., 2006. Estimation of in vivo brain-to-skull conductivity ratio in humans. *Appl. Phys. Lett.* 89, 223903–223903. doi:10.1063/1.2398883
- Zhu, Y., 2004. Parallel excitation with an array of transmit coils. *Magn. Reson. Med.* 51, 775–784. doi:10.1002/mrm.20011